Study on CMOS LSI Systems for Solar-Cell-Powered Continuous Glucose Monitoring Contact Lenses

CHEN Guowei

TABLE OF CONTENTS

LIST OF FIGURES

iii

v

vi

LIST OF TABLES

CHAPTER I

Introduction

1.1 Background of Diabetes

The number of people with diabetes is increasing year by year. According to WHO, it reached 422 million in 2014 and tends to increase continuously [1]. What's worse, data on deaths from diabetes is increasing due to long-term damage to the body, threatening people's health and burdening our society [2].

There are three types of diabetes, which are normally named type 1 diabetes, type 2 diabetes, and gestational diabetes, respectively. People with type 1 diabetes can't produce enough insulin in the body. People with type 2 diabetes have a deficient ability to utilize insulin in the body effectively. Gestational diabetes occurs in a portion of women during pregnancy, because of the antagonism between the placenta and insulin. The symptoms of increasing blood glucose above the normal level are medically known as hyperglycemia, which may occur in all three types of diabetes. The symptoms of decreasing blood glucose below normal level are medically known as hypoglycemia, which usually occurs in type 1 diabetes, but is also possible among people who take an overdose of insulin.

All three types with serious symptoms should receive insulin administration which requires an insulin pump or manual insulin injection, especially for people with type 1 diabetes whose glucose level may drop suddenly. However, blood glucose levels vary differently among different people. Even for a single person, there are many random fluctuations in blood glucose level, some of which may just result from an emotional change. This gives a challenge to insulin administration. As for the people with mild symptoms or before being diagnosed with diabetes, they don't need insulin administration, but also require a healthy diet or physical activity to delay or prevent the onset of diabetes. No matter how

1

serious their symptoms are, they should know their blood glucose level more accurately and frequently than normal people.

In conventional methods to observe blood glucose levels, pricking and taking a blood sample from fingers are inevitable. However, most people dislike this invasive method because of mental or physical resistance. In addition, the pricking method limits the times of blood collection, which is unwelcome among people who must know their glucose level frequently. Especially for type 1 diabetes, continuous glucose monitoring (CGM) is preferred and required to confront random glucose fluctuations. Sometimes CGM can even save their life from hypoglycemia symptoms. Although finger pricking is a relatively cheap way to monitor the glucose level accurately, this method becomes less and less popular, and it can be predicted that the market of pricking-based glucose monitoring will shrink as other emerging glucose monitors develop.

1.2 Emerging Healthcare Devices for Glucose Monitoring

In order to relieve the pain of blood collection and chase an accurate method to continuously monitor the glucose level with high time resolution, many approaches have been proposed and developed in the last decades. Table 1.1 summarizes some approaches and products which are available or in development.

Interstitial fluid-type glucose monitors have been developed and commercialized by some companies [3]–[5]. The glucose sensors which are attached to upper arms or stomachs can detect the glucose in interstitial fluid, requiring the injection of a tiny needle into subcutaneous tissues. Therefore, accuracy is the best among these emerging methods. The data readout is on demand, which needs action from people to scan the sensor by a dedicated reader. Then, the sensor can send the data wirelessly to the reader. This scanning is sometimes forgettable. Therefore, the next-generation sensor eliminates the necessity of the reader, and sends the data directly to people's phones, thanks to the evolutions of low-power wireless communication techniques. However, this emerging product has a lifespan of only 14 days

2

and is much more expensive than conventional pricking-type monitors which only cost ¥100 for one test.

A Finger optical-type glucose monitor is in research and development. It adapts a near-infrared (NIR) LED to record photoplethysmography (PPG) spectroscopy from fingers [6], [7]. This method measures the light transmission or reflection to infer the glucose concentrations. This new approach is non-invasive, but with low accuracy, because extracting the useful PPG signal is difficult. There are much other interference and noise from the finger's vessel, skin color, or ambient environment. Therefore, the selectivity of glucose sensing is poor. This issue should be tackled by heavy compute load through field-programmable gate arrays (FPGA) or other computers, which results in a large overall size. Therefore, this approach can be only on-demand and intermittent. The same situations apply to the earlobe-type glucose monitor [8], [9]. The difference from finger-optical types is that it adopts a microwave to detect the signal transmission or reflection.

Table 1.1: Emerging healthcare devices for glucose monitoring.

	Interstitial Fluid-Type	Next-Gen Interstitial Fluid-Type	Finger Optical-Type	Earlobe Microwave-Type	Intermittent Tear Glucose-Type	Continuous Tear Glucose-Type
Product Image						
Invasiveness	Yes (upper arm/stomach)	Yes (upper arm/stomach)	No	No	No	No
Accuracy	Good	Good	Bad	Bad	Moderate	Moderate
Time Resolution	On demand	Every 5 minutes	On demand	Several minutes	On demand	Seconds–minutes
Data Readout	Dedicated RFID reader	Wireless connection to phones	Dedicated device	Wire(less) connection to phones	Dedicated device	Wireless connection
Maker	Abbott dexcom	Abbott SIBIONICS 硅基仿生	LTT Light Touch Technology	GlucoTrack	PROVIGATE sustainnovation for healthy living	健而 NII
Price	Reader:¥7000 Sensor(14 days): ¥7000	Sensor(14 days): ¥9000	Undecided	Undecided	Undecided	Undecided
Completion Degree	Product	Product	In development	In development	In development	In development

Tear glucose-type monitors have attracted much attention in recent years because of their non-invasiveness [10]–[17]. The researchers found that the glucose in tear fluid has a relationship with blood glucose [18], [19]. Although glucose concentration in tear fluid is only 0.1–0.6 millimoles per liter (mM/L) which is nearly ten times lower than blood glucose, it can be detectable as the bio-materials and front-end electronics evolve with higher sensitivity and selectivity. The glucose sensor can be mounted on contact lenses with wireless communication integrated circuits (IC) for data readout. Since there is always tear fluid in the eyes, sensing can be anywhere and anytime. The time resolution highly depends on the available power, which is usually from dedicated wireless power-transferring devices.

From the above introductions about emerging glucose sensors, we can summarize the main trade-offs when we select emerging glucose monitors as in Figure 1.1, which are non-invasiveness, accuracy, overall size, and sensor lifespan. We have to sacrifice a certain level of non-invasiveness to improve the sensing accuracy. The implanted sensors require a miniaturized size for bio-compatibility and wearability but make themselves more fragile and short-lifetime. This dissertation focuses on tear glucose monitoring contact lenses. Not only because it's the most promising solution to achieve the balanced point of these trade-offs, but eyes also contain other important bio-informations, such as cholesterol, sodium, and intraocular pressure, which can be detected by smart contact lenses in the future.

14 days	14–30 days	Long as electronic device
Sensor Lifespan		
Wearable for 24/7	Wearable for 12 hours a day	Not suitable for long time carry
Overall Size		
Accurate	Moderate	Inaccurate
Glucose Sensing Accuracy		
Implanted	Contact with eyes	On the skin
Non-invasiveness		
Interstitial Fluid-Type	**Tear Glucose Contact Lens**	**Earlobe Clip/Finger Clip**
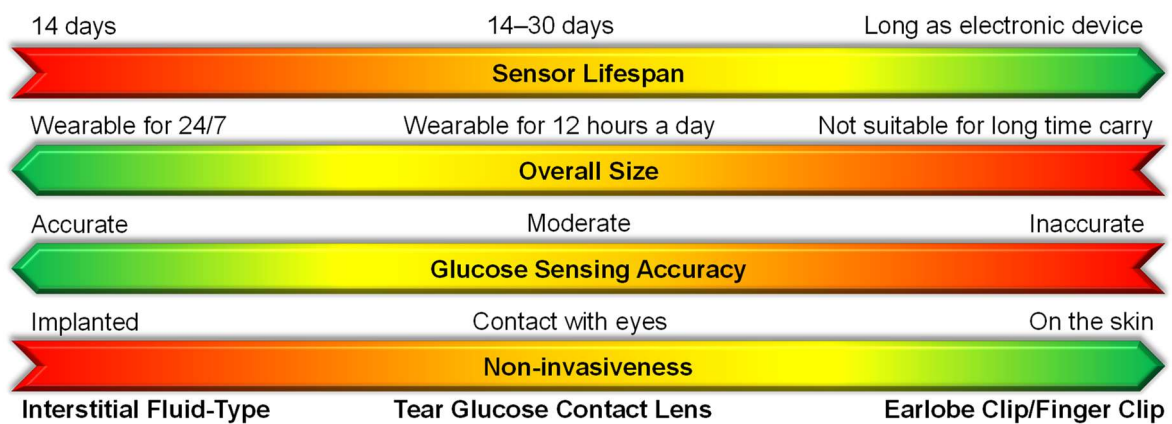
Figure 1.1: Trade-offs of emerging glucose monitor features.

1.3 Smart Contact Lenses for CGM

From the start of the 2010s, many smart contact lens prototypes have been proposed mainly by researchers and universities [10]–[17], [20]–[25]. From the mid of the 2010s, some smart contact lenses have been released by industrial companies [26], [27], and were approved by the U.S. Food and Drug Administration (FDA) [26]. The applications of these smart contact lenses cover intraocular pressure measurement, glucose monitoring, eye tracking, electroretinography (ERG) recording, low-vision augmented reality, and so on. As fabrication techniques develop, these smart contact lenses have been coming from science fiction to reality.

Among them, CGM smart contact lenses always attract researchers' interests, whose state-of-the-art is advancing further and further. From the birth of the first CGM smart contact lenses, there are basically two generations of evolution as shown in Figure 1.2. The first generation of CGM contact lenses are powered by wireless power transfer, and backscattering the glucose information to a dedicated reader like radio frequency identification (RFID) [11]. This system consumes 3 μW, requiring pairing smart glasses for data readout. Compared to the first generation using passive communications, the second generation adopts active data transmission without the help of smart glasses [14], [16]. By employing a glucose biofuel cell (BFC) [14] or a battery as power sources [16], data readout becomes fully autonomous. This strategy and evolution trend keep the same with interstitial fluid-type monitors that commit to removing the necessity of a dedicated reader to establish a simpler system. Benefiting from evolving circuit design and fabrication techniques, the power consumption of the second generation is reduced to 0.27–143 nW.
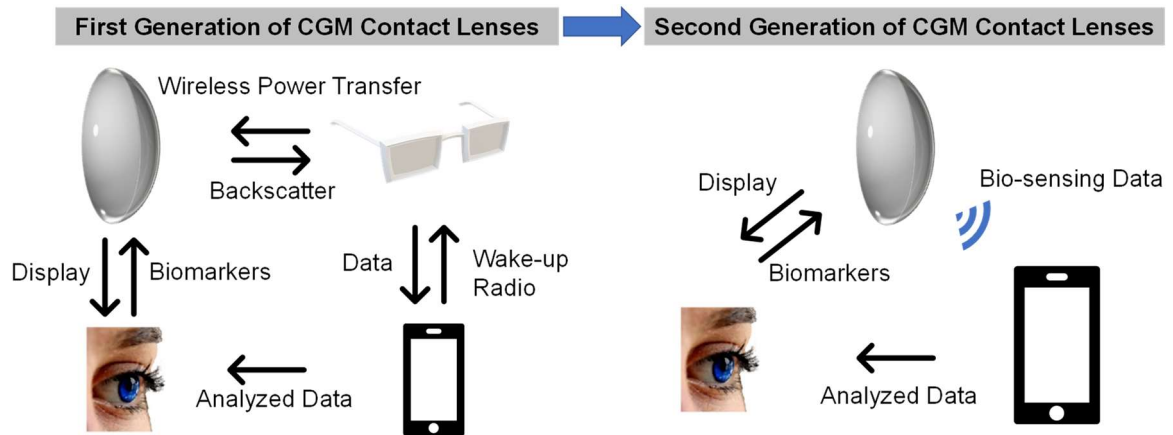
Figure 1.2: The evolution of smart contact lenses shows a trend of simpler systems.
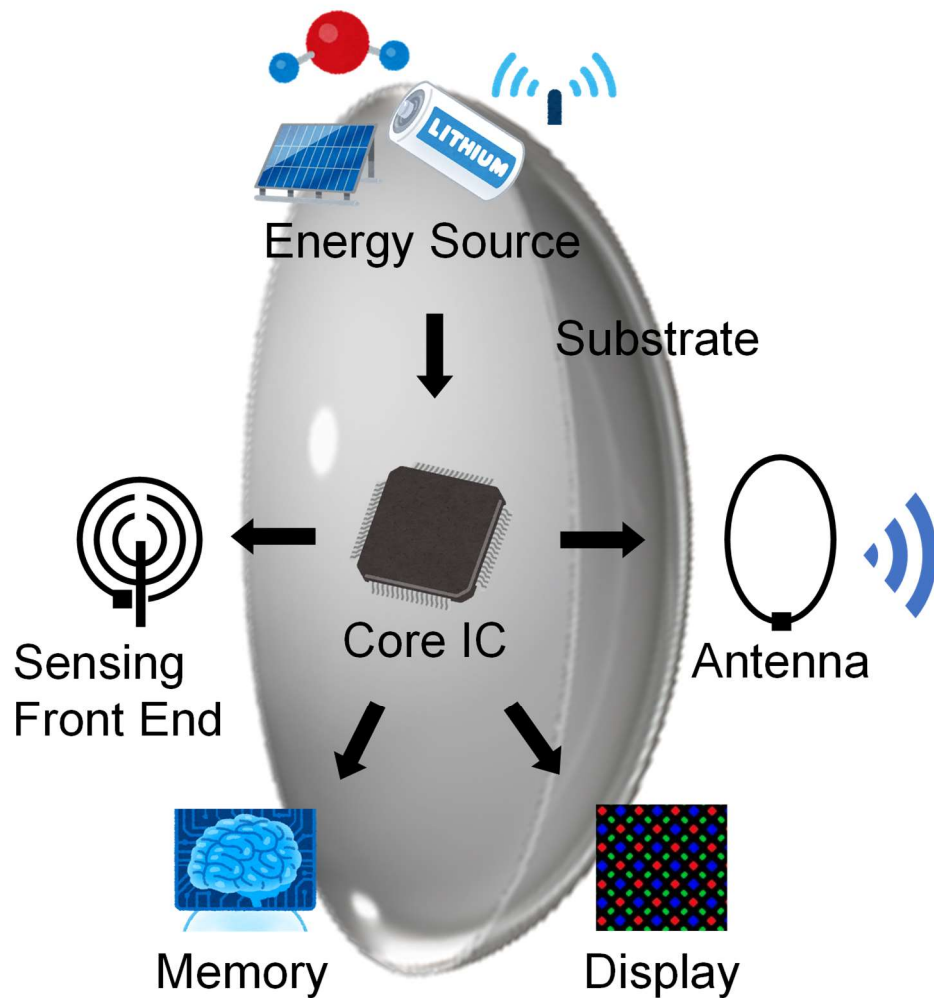
Figure 1.3: Compositions of CGM contact lenses, including energy source, substrate, core IC, sensing front end, antenna, display, and memory.

As shown in Figure 1.3, most CGM contact lenses contain at least one component from the following compositions: energy source, substrate, core IC, sensing front end, antenna, display, and memory. Compared with battery-powered electronic devices like smartphones, available area and space on contact lenses are limited. Therefore, the options for energy sources are area-saving-oriented. To the best of the author's knowledge, the world's smallest solid-state battery is a bare die of 1.75 mm × 2.15 mm (Cymbet) [28]. The capacity of 5 µAh can only satisfy a power load of mA level by several seconds, let alone the leakage power during standby mode. This is not enough for a long-lifespan CGM application. Considering the typical diameter of the contact lens is 13–16 mm, it can't afford a battery with a larger size.

Most previous smart contact lenses adopt wireless power transferring for power supply. The power transferring coil is assembled on glasses. This method passes the energy source to another device which is a dedicated reader glass to obtain a larger battery. However, it is not a highly energy-efficient way, because the coil is transferring power everywhere and some energy is wasted. According to the previous state-of-the-art prototype [20], the efficiency of the power harvesting system is below 10%. Therefore, a deeply duty-cycled operation is necessary to achieve monitoring throughout the day. On the other hand, batteries incur the issues of disposal when the lifecycle runs out. Choosing an environmentally friendly way is also a key point in the future design of smart electronics.

Therefore, some previous works adopt energy harvesting from the ambient environment. For example, using tear glucose as biofuels to power the core IC [14]. This method employs glucose fuel cells as both the sensing front end and energy source, saving area but sacrificing sensing accuracy. To obtain a more accurate glucose level, some previous designs adopted potentiostat as a sensing front end combined with a high-accuracy analog-to-digital converter (ADC), to transduce the glucose concentrations to a digital code [16]. As the analog circuit design develops, ADC with more than 10 bits is possible to integrate on a biosensor chip.

Core IC should manage the input/output power, process signals, control the operation

timing, modulate the transmitter circuits for wireless communications, and so on. As fabrication techniques develop, advanced large-scale integration (LSI) systems are becoming more versatile and more powerful, but still facing challenges when applied to smart contact lenses which require extremely small areas, low standby power, and high performance of analog sensing and communication.

Antenna, display, and memory functions are optional to CGM contact lenses. All three functions target information transmission to the users, but the transmission speed and data freshness are different among them. For display on contact lenses, the information transmission is fastest and the data is fresh because the information is directly shown to human eyes. However, display drivers are power-hungry, requiring power at mW level. Wireless transmitters using an antenna should coordinate with a receiver, which can be a smartphone or smart glasses. Although the communication speed of wireless methods is fast and low-power wireless communication protocols are available nowadays, we have to consider the connectivity between CGM contact lenses and the receivers. If the available power is limited, the connection can be lost. Since there is always a delay existing, the speed and data freshness is not the best. The memory stores the sensing data on contact lenses when enough power is unavailable and the aggregated data can be sent out when power is sufficient. This method sacrifices data freshness but can obtain flexibility and ease the power demands. From the above discussions, we can find that a trade-off to design CGM contact lenses is between power and data freshness. It depends on the users' symptoms and their needs. From the interests of people with type 1 diabetes, the fresher the data is, the quicker reactions they can respond to prevent hyperglycemia/hypoglycemia conditions. If the users have only mild symptoms, low data freshness can be acceptable, and memory-type CGM contact lenses are applicable to most scenarios. The main properties of these three information transmission methods are shown in Figure 1.4. A key technique to leverage these three methods is power adaptation so that the function can be switched smoothly in various scenarios. That means the core IC should be able to function under a wide power range without fatal errors.
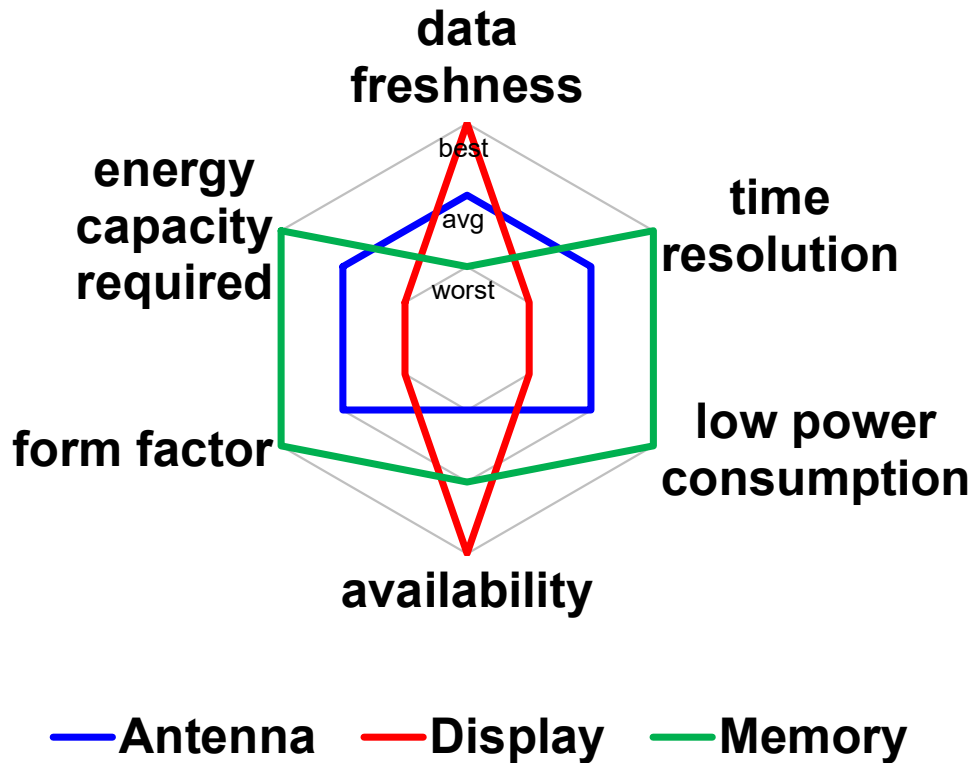
Figure 1.4: Main properties of the different information transmission methods of CGM contact lenses.

1.4 Design Considerations of Smart Contact Lenses for CGM

This dissertation focuses on designing next-generation smart contact lenses for CGM that are adaptable to more application scenarios, user-and-environmentally friendly, and closer to actual daily usage. As introduced in the evolution from Generation 1 to Generation 2 CGM contact lenses, a key point of making them easy to use is to reduce the burden on users. The less they carry, the more willing they are to wear. A stand-alone system with fewer devices and fewer motions is preferred since it makes people live in a general routine. This poses challenges to energy sources, communication schemes, core IC power minimization, size miniaturization, and so on.

1.4.1 Energy Source of CGM Contact Lenses

Starting from Generation 2 CGM contact lenses, pairing smart glasses which play the

role of power transmitters and data interrogators, is not necessary anymore. Because CGM contact lenses are trending toward stand-alone, energy-autonomous, and active data transmission. Since the conventional way of wireless power transfer becomes impossible without pairing glasses, we have to search for another energy harvesting option before we compromise on a battery.

Based on the previous investigations [29]–[37], the energy sources available on CGM smart contact lenses are light using photovoltaic (PV), body heat using a thermoelectric generator (TEG), biofuel using biofuel cell (BFC), human vibration using a piezoelectric generator (PZT), ambient wireless RF from GSM or WiFi base station without dedicated power transmitters. The typical harvesting power density is shown in Figure 1.5 left. Energy harvesters through light achieve the highest power density and a wide power range. The unstable solar power could be an issue for reliable IC operation, whereas it's not a problem on TEG using body heat. However, since eye temperature is a little bit lower than body temperature [38] and there is a further degradation of contact lens [39], a large area of TEG is required which is not suitable for contact lens applications. The same condition also applies to vibration and ambient wireless RF energy harvesting.
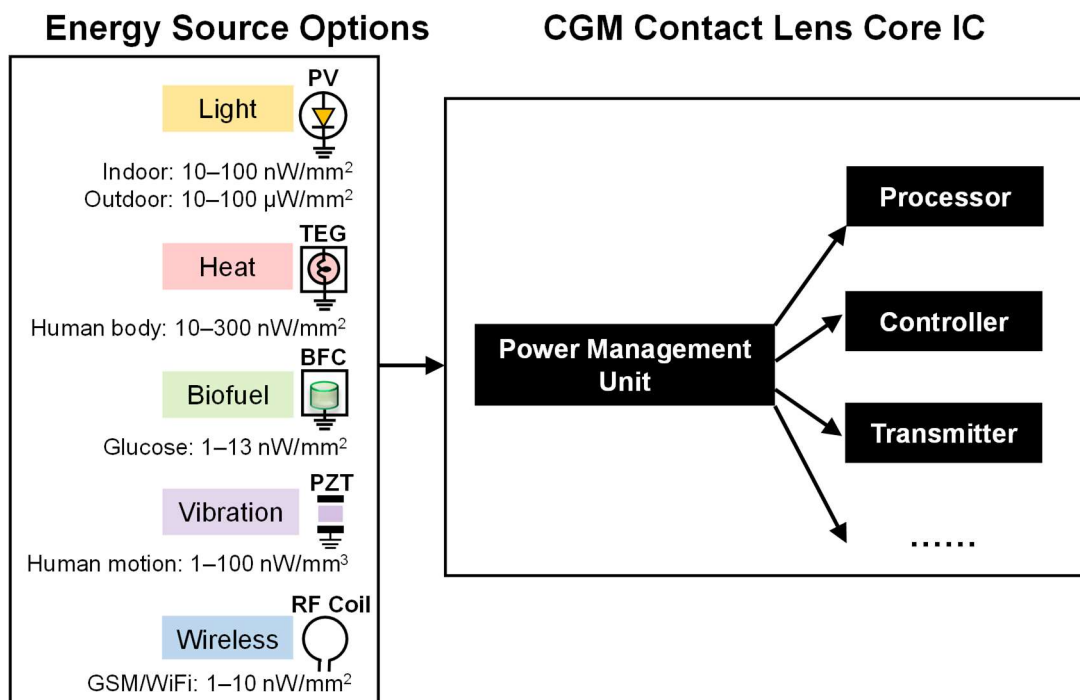
Figure 1.5: Available energy source options on CGM contact lens for core IC.

It should be noted that recently published glucose-based BFC [33] features an output performance of 43 µW/cm^2 (430 nW/mm^2), which is the highest BFC power density to date. However, the required glucose concentration should be 500 mM/L, which is 1000x larger than tear glucose. It can be estimated that the degraded power density by tear glucose is tens of nW/mm^2 at most, which is impossible as the energy source.

In order to leverage solar power with the highest power density among these options, power fluctuation should be tackled. As mentioned in Section 1.3 about the power-data freshness trade-off, various function options are adaptive to a wide power range by playing a trick on data aggregation and freshness. Therefore, the effect of solar power fluctuation can be solved by circuit power adaptation. In addition, silicon-based solar cells can be fabricated by a CMOS process easily, because PN junctions as photodiodes inherently exist in CMOS devices. This characteristic makes solar cells compatible with CMOS IC chips, and everything-fully-on-chip design can be possible, which reduces the post-fabrication costs.

Based on the above considerations, solar cells harvesting energy from ambient light can be a good energy source for next-generation CGM contact lenses.

1.4.2 Communication Schemes of CGM Contact Lenses

Since the interrogator, which is smart glasses, is no longer used, an RFID-like readout scheme is impossible due to the physical distance between the contact lenses and other electronic devices. Although smartphones can approach eyes manually, it requests people's motion intentionally, which can not be conducted very often. Figure 1.6 shows a recorded blood glucose concentration plot with different time intervals. If glucose data is monitored every 5 minutes, it can look into the glucose change in detail. However, no one can afford to put their phones close to their eyes every 5 minutes. In usual cases, a 40-minute interval can be acceptable, but it can miss the glucose peak, which is the event of interest, as shown in Figure 1.6. Observed from plotted glucose concentrations, the glucose level must be detected every 15 minutes or more frequently, so that the event of interest will not be missed.
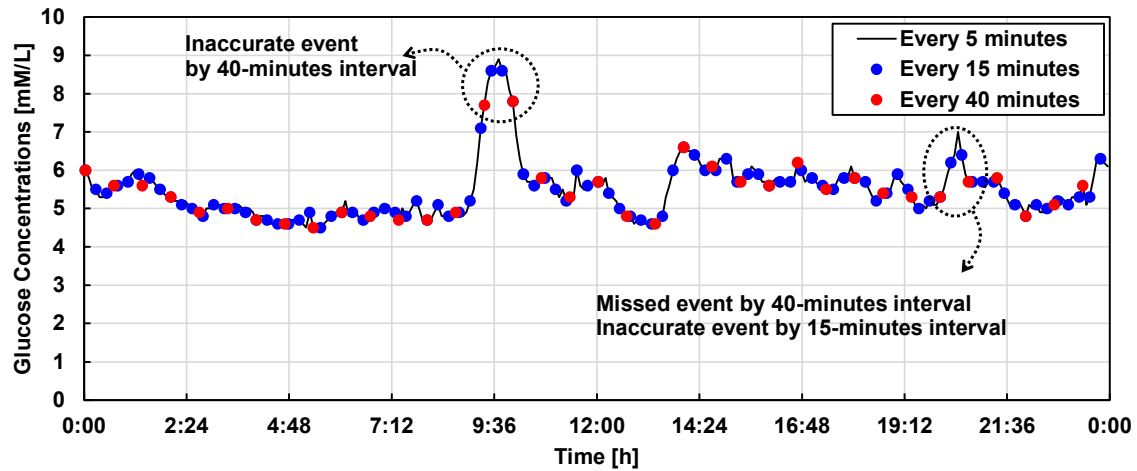
Figure 1.6: Recorded blood glucose concentrations by an implanted sensor with 5, 15, and 40 minutes time intervals.

To free people from intentional data interrogation, active data transmitters, like wireless RF transmitters (TX) or a display, are preferred in the next-generation CGM contact lenses. In some previous research [14], BFCs are used to power the TX with an on-chip antenna but suffer from a communication distance of only 10 cm, which is constrained by available power from tear glucose. To extend the communication distance above 1 m, a thin-film battery is adopted to power a TX with a large off-chip antenna [16]. Since an off-chip capacitor can provide a large current of relatively the same level as rechargeable batteries [40], it can be believed that an energy harvesting system with solar cells and an off-chip capacitor can also achieve a long communication distance as a battery-powered system.

Another communication scheme is to utilize an on-lens display to inform the glucose level directly to human eyes. Different from a light-emitting diode (LED) or liquid crystal display (LCD) array on smartphones that draw a high current, a single-element LED display that consumes sub-mA current is possible to light up by an energy harvesting system on contact lenses. Previous research employed wireless power transfer to deliver 12 μW to the chip driving a custom micro-LED at 362 kHz [20]. 12 μW is difficult to realize by on-lens solar cells since it requires 120 mm^2 at least for indoor operation. Therefore, it should be solved by leveraging the trade-off between energy and power density. Solar cells have a

relatively low power density and a high energy density (μWh/mm^2), but capacitors have a high power density and a low energy density. As a high lighting frequency at kHz is not necessary for CGM applications, we can deeply duty-cycle the LED lighting time. The duty cycling can store harvested energy in a capacitor to deliver a high current for LED lighting. The same method is also applicable to TX for a high RF radiative power.

We can find that an accurate CGM requires frequent detection for a high resolution, but the trade-off between energy and power density requires a deep-duty cycle to store enough energy for power-hungry circuits. It is a conflict of interest. Then, it introduces a new trade-off between power and miss rate. To leverage the power-miss rate trade-off, not only do we have to choose CGM time intervals carefully, but we should also elevate the core IC performance which includes highly-efficient power converting and low-power low-leakage circuit design. Considering that the appropriate CGM time interval is 15 minutes or below, this time is enough to store sufficient energy for μs-level LED lighting and TX transmission.

1.4.3 Core IC Power Minimization

As a key enabler of stand-alone biosensing systems and leveraging the power-miss rate trade-off, reducing the power consumption of core IC can make the CGM system available even under a low power supply. Figure 1.7 shows the power breakdown of a CGM contact lens system. As mentioned in Section 1.4.2, duty-cycling reduced total power consumption because the operating time of the most power-hungry building block, TX, is shortened. Then, it is transformed from a continuously active system to a time-driven system. However, it still faces some challenges to minimizing power consumption further.
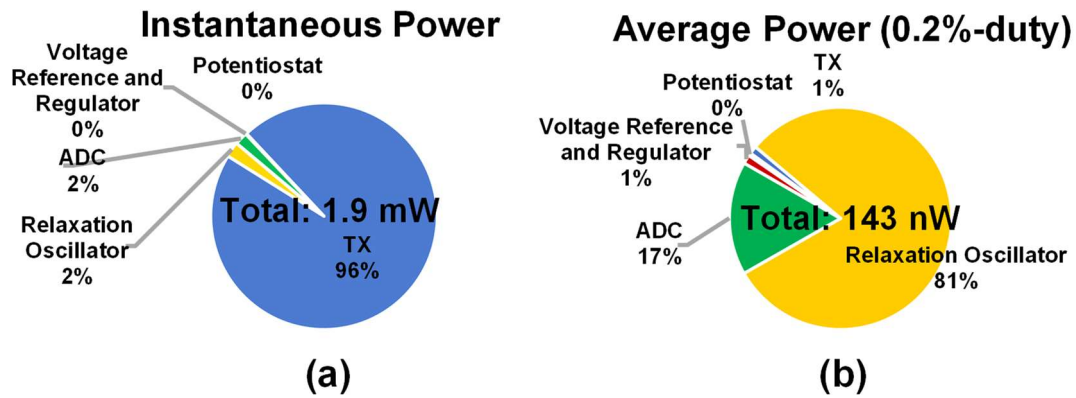
Figure 1.7: Instantaneous/average power breakdown of a CGM contact lens system with a wireless TX [16].

First, the relaxation oscillator, which generated the system clock, consumed a 100 nW average which should be reduced. As CGM contact lenses can start up several minutes at a time, a high-frequency clock is not necessary. The wireless communication system does not need a dedicated high-frequency oscillation generator because an LC power oscillator can work for both oscillation and RF radiation. It should be noted that a relaxation oscillator is not a must-required building block in a biosensing system, because there are cloud-driven and event-driven systems besides time-driven systems. In cloud-driven systems, the sensor is woken up by a request from the cloud periodically. However, a data interrogator is needed, and an event of interest could be missed because the cloud doesn't know the situation inside the sensor. Event-driven systems capture the data by an on-chip event detector. For example, if the detected voltage of BFC exceeds a threshold, the data will be transmitted [41]. But this strategy could miss hypoglycemia or other useful data between the upper limit and lower limit. Taking into account the features of CGM, continuous monitoring at the minutes level is necessary. Even the glucose level in the normal range should be recorded because users need to know their body reactions to different stimuli, such as foods with high glucose concentrations. Therefore, a time-driven system is the most suitable activation pattern for CGM applications, and a low-power relaxation oscillator should be designed to provide a system clock.

Second, the sensor readout block (potentiostat + ADC) consumes 21-nW average power which can be reduced further. The potentiostat provides voltage biases for the glucose sensor consisting of a working electrode, a counter electrode, and a reference electrode. During the redox reaction, the electric current in the glucose sensor is mirrored by the potentiostat and transduced to a digital code by an ADC. This strategy was adopted by some previous research [12], [16]. All these sensor readout blocks are power-hungry at 0.4–0.5 μW and hard to scale down further. Recently, a new design philosophy is proposed to reduce power consumption, utilizing a supply voltage monitor (SVM) to transduce the voltage of BFC to a digital code [42]. The combination of SVM + BFC consumes nW-level power because the BFCs can leverage the power from glucose and generate a voltage/current by themselves. Then, a part of the power load is transferred from the core IC to the BFCs. In addition, BFCs can be physically scaled down to sub-mm^2 due to the evolution of new materials but potentiostats can not. Therefore, SVM + BFC can be a new solution to a miniaturized next-generation CGM system.

1.5 Dissertation Outline

This dissertation will overview three designed very large-scale integration (VLSI) biosensing systems for next-generation CGM contact lenses, as shown in Figure 1.8. Based on Generation 2 CGM contact lenses utilizing BFC as a supply-sensing source, these designs reform it to a solar cell-BFC combined system to maximize the available power density and reduce power consumption. These efforts achieved a stand-alone biosensing system on contact lenses, minimizing human burden and motions.

A New Paradigm for CGM Contact Lens: A Solar Cell and Biofuel
Cell Jointly-Powered Biosensing System
✓ Fully-on-chip solar cells, antenna, and energy harvesting circuits

Application Scenario I
Normal Case

Application Scenario II
Emergency Case

A Solar Cell-Powered Biofuel Cell-Input Biosensing
System with an Off-Chip Antenna for Long-Distance
Wireless Communication
✓ Large size antenna for long communication distance
  (>40 cm)
✓ An FSK-PIM-Combined near-2.4 GHz Transmitter for
  2-D modulation

A Solar Cell-Powered Biofuel Cell-Input Biosensing
System with an LED for Direct
Hyperglycemia/Hypoglycemia Warning
✓ Fully stand-alone RF-less system
✓ LED driving capability for emergency alert (glucose
  too high/too low)

Figure 1.8: Organization of this dissertation and main contributions of each project.

In Chapter II, a new paradigm for CGM contact lenses is presented as a solar cell and BFC jointly-powered biosensing system capable of wireless communications. To facilitate BFC area reduction for the applications in area-constrained CGM contact lenses, an energy harvester combined with an on-chip solar cell is introduced as a dedicated power source for the power-hungry transmitter. A dual-oscillator-based SVM which is powered by BFC is employed to convert the output voltage of BFC into digital codes. The 8-bit digital code is given to a digital-to-analog converter (DAC) to modulate the TX frequency by Frequency-Shift Keying (FSK). The VLSI system integrated an on-chip antenna for data transmission to bring down the cost. From measurements of the test chip fabricated in 65-nm CMOS technology, the energy harvester achieved an output voltage above 1 V by up-converting the solar cell's voltage, which satisfies the minimum operating voltage of the TX. The solar cell-based energy harvester achieved 89% BFC area reduction compared to BFC-powered previous work [14]. These results pave the way to the more powerful solar cell-powered BFC-input biosensing systems for two application scenarios that bring CGM contact lenses closer to practical applications.

Chapter III focuses on Application Scenario I which targets normal cases of all types of diabetes. To tackle the issues of varying solar power and extend the wireless communication distance. This work presents a battery-less biosensing system for solar cell-powered BFC-input CGM contact lenses featuring a near 2.4 GHz transmitter. The modulation method

combines FSK and pulse interval modulation (PIM) to send RF signals with two-dimensional information including the solar cell's voltage, which aims to overcome the impact of unstable solar power. The charge-pump-based energy harvester converts the solar-cell voltage above 1.8 V to achieve a transmission distance longer than 40 cm, which allows communications between contact lenses and handsets. The SVM is improved by replacing the BFC power with solar cell power. By employing the BFC-input SVM-interfaced approach instead of using a power-hungry potentiostat + ADC, powering and sensing components are separated, which reduces the power budget from solar cells and BFCs. The TX receives 5 bits from SVM and achieves a wide tuning range of 2.1–2.3 GHz which targets 2.4-GHz communication with handsets. The fabricated chip in a 65 nm CMOS process consumes 126 nW at 0.37-V supply, which is manageable by on-lens solar cells in an ambient-light environment.

Chapter IV focuses on Application Scenario II which targets emergency cases for people with type 1 diabetes and serious symptoms. It presents the first solar cell-powered BFC-input biosensing system with PIM and pulse density modulation (PDM) LED driving capability for CGM contact lenses featuring stand-alone RF-less operation. Power supply from on-lens solar cells can eliminate the necessity of wireless power delivery, and LED implementation can eliminate the necessity of wireless communications. The BFC-input SVM-interfaced approach is improved and simplified to a BFC-input current-to-frequency transducer. By this method, the power consumption of glucose readout blocks can be further reduced, sparing LED driving more power. The charge-pump-based energy harvester converts the solar-cell voltage above 4 V to achieve a high energy density in the storage capacitor and efficient LED lighting, which allows direct communication between LED and eyes. The measured power of 28 nW/144 nW at PIM/PDM mode with a 0.31 V/0.39 V supply voltage can be managed by the on-lens solar cells, enabling a fully stand-alone on-lens operation under office-room ambient light whose typical illumination intensity is 800–1600 lx.

Chapter V summarizes and concludes the contributions of these VLSI systems, and also

17

discusses related works and future directions of next-generation CGM contact lenses. First, the glucose readout analog blocks still face challenges on how to optimize the trade-off between power, area, and accuracy, which is always a classic subject in the world of analog circuit design. Second, a powerful BFC is desired in CGM contact lenses to leverage the glucose in tears. Third, a new customized memory circuit for low-power low-voltage sensors is necessary to advance the intelligence of CGM contact lenses. Last but not least, the LSI systems for CGM contact lens applications can benefit from advanced CMOS process nodes, to bring us a high-power density solar cell, high-density memory block, and so on.

CHAPTER II

A New Paradigm for CGM Contact Lens: A Solar Cell and Biofuel Cell Jointly-Powered Biosensing System

2.1 Introduction

As mentioned in Chapter I, biofuel cells (BFC) have been playing an important role in biosensing systems because they are an efficient means of monitoring physiological signals (e.g., glucose, or lactate concentration) for wearable healthcare Internet of Things (IoT) applications [14], [43]–[45]. Compared with other sensing front ends like potentiostat, BFC is like an independent component that can operate individually without cooperating with reference electrodes or analog circuits (dedicated amplifiers, et al.). These BFCs can generate electricity and use it by themselves, saving power and area for the entire system. Some systems are directly powered by the glucose-based BFCs, which harvest energy from the following electrochemical reactions in or near-human bodies.

Anode: $C_6H_{12}O_6 + 6H_2O \rightarrow 6CO_2 + 24H^+ + 24e^-$

Cathode: $6O_2 + 24H^+ + 24e^- \rightarrow 12H_2O$
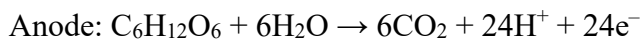
The output power is in accordance with the glucose concentration. The biological information can be noticed according to the output power, which can be read out by RF, [14], [43]–[45], or light signal [20]. Therefore, this work will employ a glucose-based BFC in continuous glucose monitoring (CGM) contact lens applications [12], [14], [46] by harvesting energy from tear glucose in human eyes that correlates with human blood glucose [19].

19

Introduced in Chapter I, a timer is a building block for the CGM system for clock generation. However, its high power consumption has not been tackled yet. A relaxation oscillator as the timer could consume an instantaneous power of 42 µW to generate a frequency of 445 kHz [16]. It is a process, voltage, and temperature (PVT)-robust due to a quadrature phase design. It also provides an operation clocking for an analog-to-digital converter (ADC), which is exploited to convert the glucose-based current into digital code for data readout. Another research employed an integrated ring oscillator to generate a clocking signal of 1.024 MHz, which is divided by 4 to create a 256 kHz signal for a $\Delta\Sigma ADC$ that consumes 180 nW [44]. From these observations, we can find that all these timers should be PVT-robust and cooperate with an ADC for signal conversion. However, the high power consumption is not affordable for a CGM contact lens. To achieve a battery-less BFC-compatible operation at low biomolecule concentration, our strategy is embedding a low-power relaxation oscillator in a supply voltage monitor (SVM) which operates like an ADC. The relaxation oscillator utilizes gate-leakage current to charge/discharge a MIM capacitor with low supply sensitivity, only consuming power at pW level. The SVM has another oscillator with high supply sensitivity. Then, the frequency of two oscillators is substrated as a voltage-to-frequency converter, acting like an ADC. Therefore, the low-power relaxation oscillator works as a timer and a signal converter at the same time. This method brings power consumption down significantly from hundreds of nW to pW.

Although with the ultra-low-power front-end techniques, a transmitter circuit (TX) for wireless communication is typically the most power-consuming component of these systems. In previous works, the power of TX was on the order of tens of µW [43], which is difficult to achieve even with the state-of-the-art BFC energy harvester [47], [48]. Moreover, most of the BFCs are with a bulky size of mm^2 level, which is infeasible to be accommodated in contact lenses. Although previous work has proposed a circuit architecture of a CGM system that utilizes a 2 cm × 2 cm BFC [48], the BFC area should be further reduced to 0.6 mm × 0.6 mm as shown in Figure 2.1 to make it compatible with CGM contact lenses [34]. Thus,

we should use a dedicated power source for TX to reduce the required BFC area.

To integrate a sub-mm^2 BFC into the area-constrained CGM contact lenses, this work proposes a solar-cell and BFC jointly powered wireless biosensing system as an innovative solution. To power a TX and facilitate BFC area reduction, an on-chip solar cell is introduced to the system as a dedicated power source for the TX. Furthermore, a self-controlled dual-oscillator-based SVM [49], powered by the BFC, is used to monitor the BFC output which is correlated with biological signals. This proposed architecture enables 89% BFC area reduction, [46], compared with the state-of-the-art BFC-based biosensing systems [14], [43], [44].

The proposed biosensing system is presented in Section 2.2, while Section 2.3 describes the measurement results. Finally, Section 2.4 concludes this work.
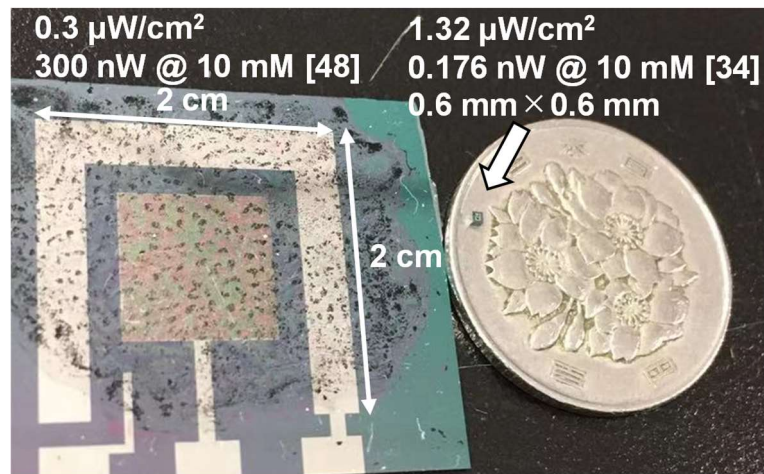
Figure 2.1: State-of-the-art BFCs power extraction capabilities.
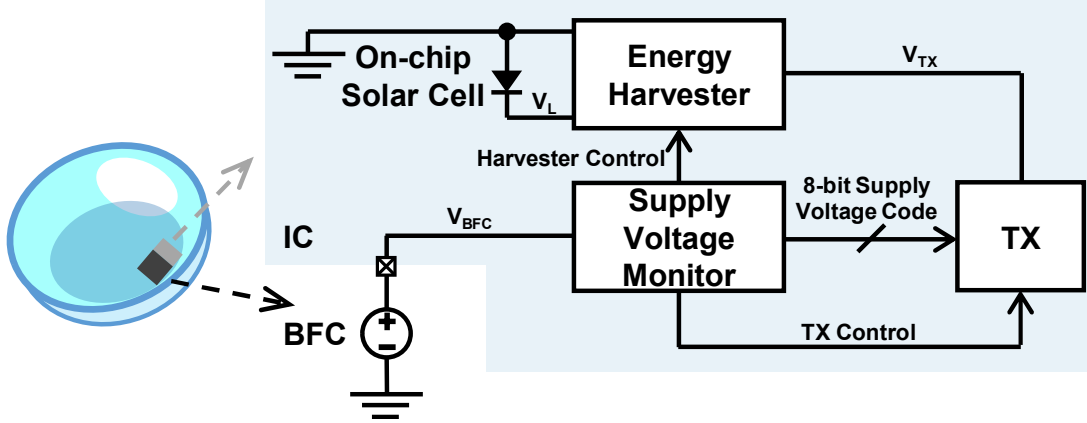
Figure 2.2: Block diagram of the proposed solar cell and BFC jointly powered wireless biosensing system for CGM contact lens.

2.2 System Architecture

2.2.1 Overall Architecture of the Biosensing System

A block diagram of the proposed solar cell and BFC jointly powered wireless biosensing systems and the conceptual image for area-constrained CGM contact lenses are shown in Figure 2.2. The on-chip solar cell is used to deliver power to the TX via a self-oscillating voltage doubler (SOVD)-based energy harvester, which boosts the output voltage of the on-chip solar cell. The SVM is directly powered by the BFC and converts V_{BFC} to an 8-bit supply voltage code for biosensing. The supply voltage monitor also controls the energy harvester and TX to ensure operation order. Directly connecting the circuits to the BFCs to acquire power and perform biosensing by reading the BFC outputs appears to be profitable [44], despite the fact that the power density of the BFC is limited to the pW/mm^2 region in tear glucose level [12].

On the other hand, solar cells can be integrated into CMOS technologies and are characterized by larger power density at tens of nW/mm^2 since PN junctions used as photodiodes inherently reside in a CMOS process [50]. This implies that solar cells are a suitable power source for the TX instead of using BFC output power. After separating the system power into two parts, i.e., wireless communication and signal conversion with timing management, the required BFC area can be determined by only considering the power of

SVM, whose power consumption can potentially reduce to become the pW region. Therefore, the tens-of-mm^2 BFC is no longer necessary, and the sub-mm^2 BFC [51] with the sub-mm^2 IC with on-chip solar cells can be integrated into CGM contact lenses.

Figure 2.3 shows the operation principle of the proposed system. The operation can be divided into three phases, i.e., energy harvesting, code generation, and data transmission. Signals from SVM control all three phases. First, during the energy harvesting phase, the harvester control signal enables the energy harvester to begin extracting energy from the solar cell to store power for the TX (Harvester Control = High). Consequently, SVM generates an 8-bit supply voltage code according to the V_{BFC} during the code generation phase (Rst and Count). After SVM ceases to generate the 8-bit supply voltage code (Hold), the 8-bit supply voltage code modulates the resonant frequency of the TX. Then, the TX transmits the data by enabling a TX control signal (TX Control = Low to High). It's worth mentioning that the three phases for one-time transmission take less than 1 s, and the entire operation can be duty-cycled below 1% to save power since the physiological signals vary slowly.
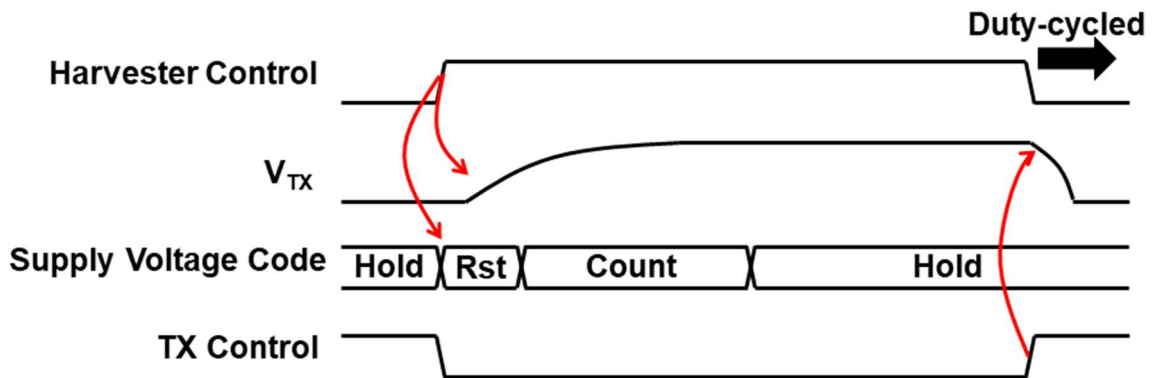
Figure 2.3: Timing diagram of the operational signal for each block.
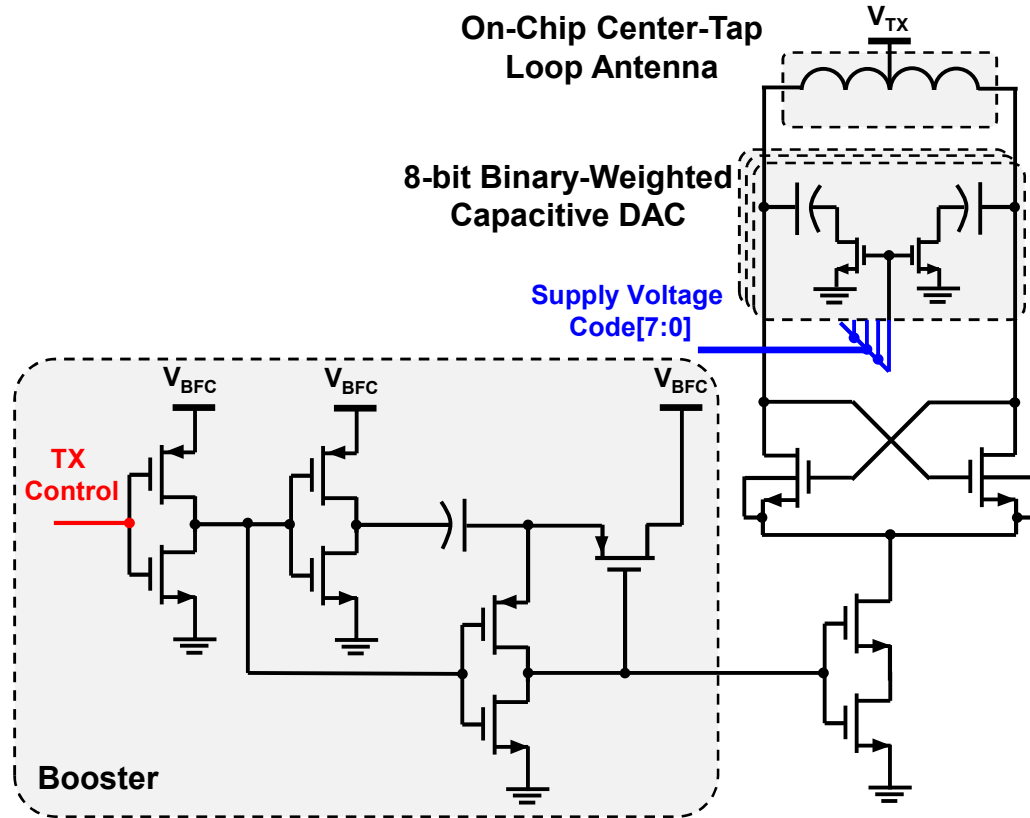
Figure 2.4: Schematic of the transmitter.

2.2.2 Direct-RF TX Circuits

Figure 2.4 shows the direct-RF power oscillator architecture of the TX. The direct-RF power oscillator architecture is selected for short active time operation [44], [51] with the on-chip center-tapped loop antenna. The 4-turn top-metal-based antenna, with a size of 385 μm × 385 μm, features an inductance of 4 nH at each half side confirmed by simulation, which is the same as the antenna in reference [14]. The antenna operates both as a resonant and radiative element, eliminating the necessity for a power amplifier and bulky matching networks.

An 8-bit binary-weighted capacitive digital-to-analog converter (DAC), totaling approximately 4.83 pF, is implemented for resonant frequency tunability. Each capacitive DAC consists of a metal-insulator-metal (MIM) capacitor and pull-down switch that uses a high V_{TH} transistor. A stacked power gating switch is used to reduce leakage to 29 pA during TX sleep time with a V_{TX} of 1 V, exhibiting 79% lower leakage in simulation compared with

an approach that uses a single transistor switch. To activate the TX using the V_{BFC}, the TX control signal is transmitted to the TX via the booster to double V_{BFC} to drive the gate of the stacked power gating switch.

2.2.3 Solar Cells-Powered SOVD-Based Energy Harvester

Figure 2.5 shows the details of the solar cell implementation. Three types of PN junctions, i.e., N+/P-well (PW), PW/deep-N-well (DNW), and DNW/ P substrate (PS), can be used as photodiodes in triple-well CMOS technology. There are two kinds of wire connection of photodiodes which are the solar cells using PS/DNW in this work and its counterpart without using PS/DNW. The difference is lying on the wire connection of PS. As all of the P-type semiconductors are interconnected in this work, once the light is imposed, all diodes can supply the current. However, the second connection which separates the P-type semiconductor inside the PW from PS excludes the PS/DNW diodes from the supply source. The PS/DNW diodes only bias the voltage. Only PW/DNW and PW/N+ supply the current, resulting in poor current density. As the priority of this work is harvesting energy in an area-constrained environment, this design implements the solar cell with PS/DNW to improve the maximum output current.
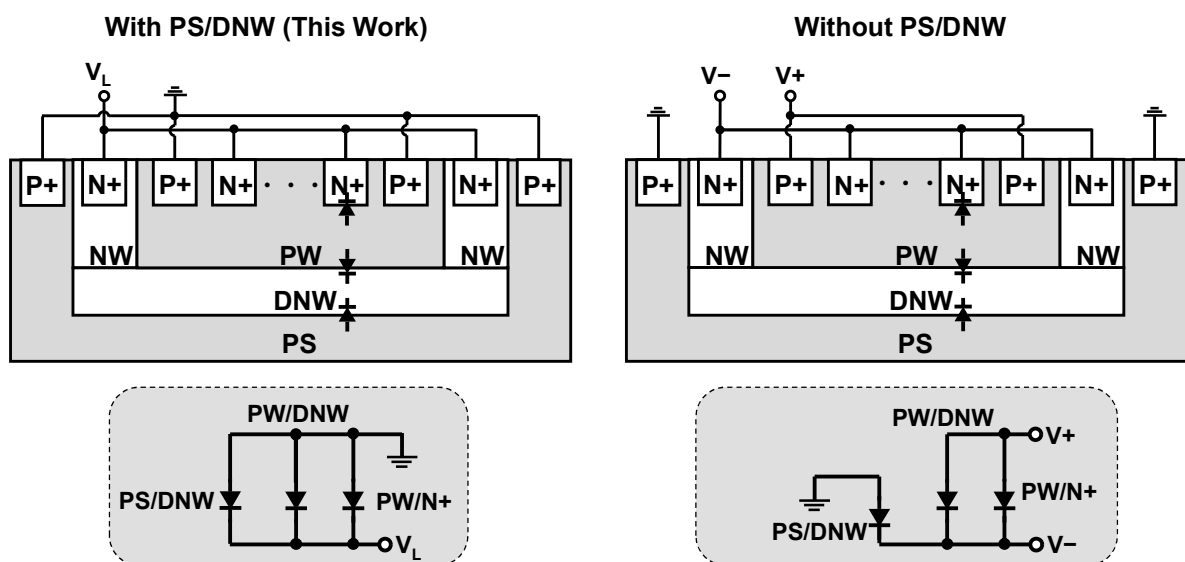
Figure 2.5: The cross-section conceptual diagram and schematic of two types of solar cells using a CMOS process with DNW.
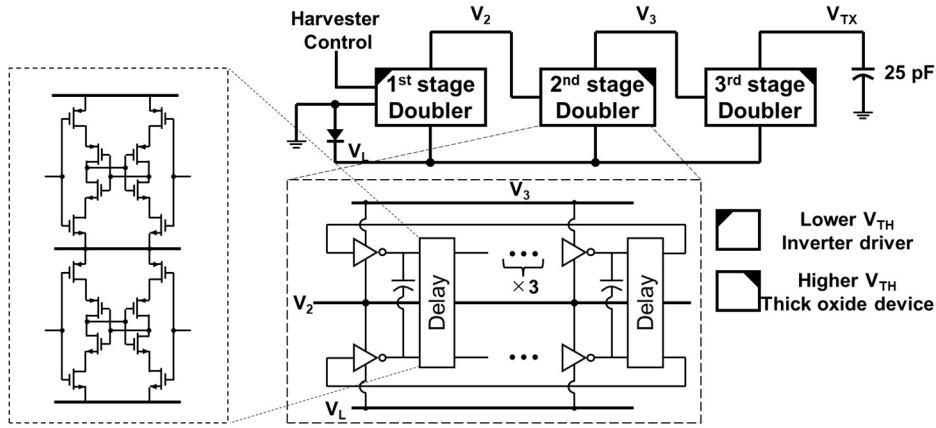
Figure 2.6: Schematic of the SOVD-based energy harvester.

Cascaded SOVDs [52] serve as the voltage converter in the proposed energy harvester, as shown in Figure 2.6. The up-conversion ratio is set to 7. To perform energy harvesting from a small solar cell output voltage, inverters consisting of low V_{TH} transistors are used in the 1st stage doubler. The controllability of the energy harvester is implemented by adding a switch to one of the inverters in the 1st stage doubler so that the energy harvester can be shut down during the holding time to save energy. The thick oxide devices with higher V_{TH} are used in 2nd stage and 3rd stage doublers to reduce the leakage and maintain a higher output voltage. The output MIM capacitor of 25 pF is adopted for TX operation which is the same as the reference [14].

2.2.4 Supply Voltage Monitor

The SVM is implemented using the self-controlled dual-oscillator architecture with different supply-sensitivity oscillators [49]. Figure 2.7 shows the details of the SVM architecture. Unlike typical biosensing systems that employ an analog front end using an ADC, the SVM converts the BFC output into an 8-bit supply voltage code via frequency subtraction using a supply sensitivity difference between the oscillators, i.e., OSC_H, and OSC_L. As shown in Figure 2.8 (a) and (b), the measured frequency of the two oscillators shows different supply sensitivities. The supply-insensitive oscillator, OSC_L, and supply-sensitive oscillator, OSC_H, can successfully generate an 8-bit supply voltage code as in reference [49].

26
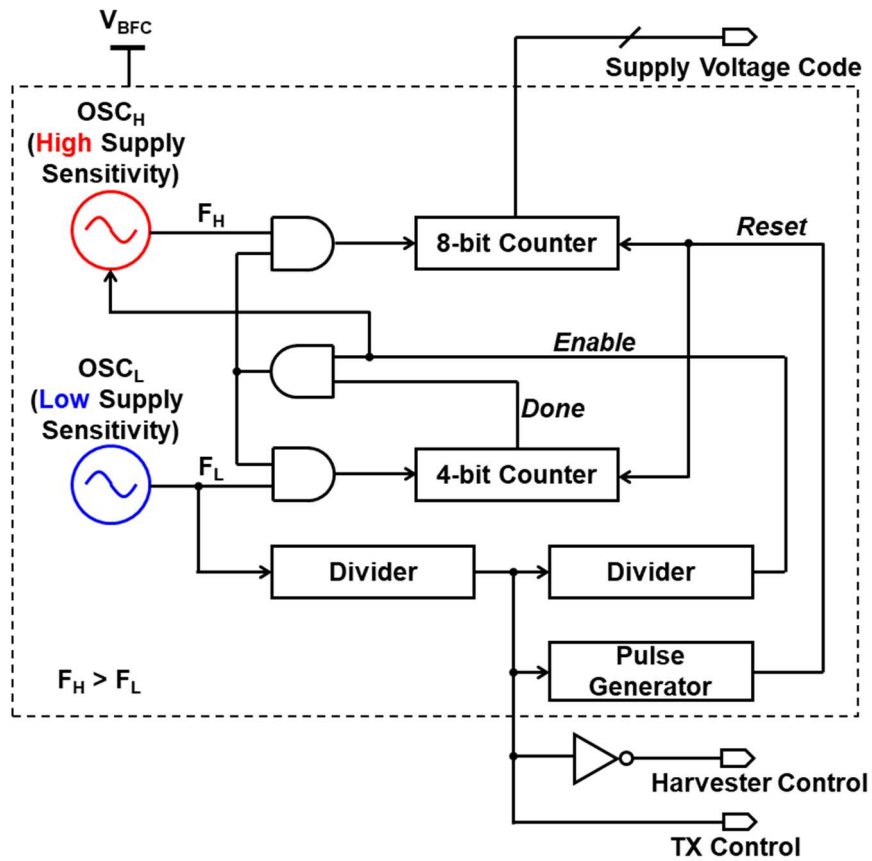
Figure 2.7: Block diagram of the supply voltage monitor.
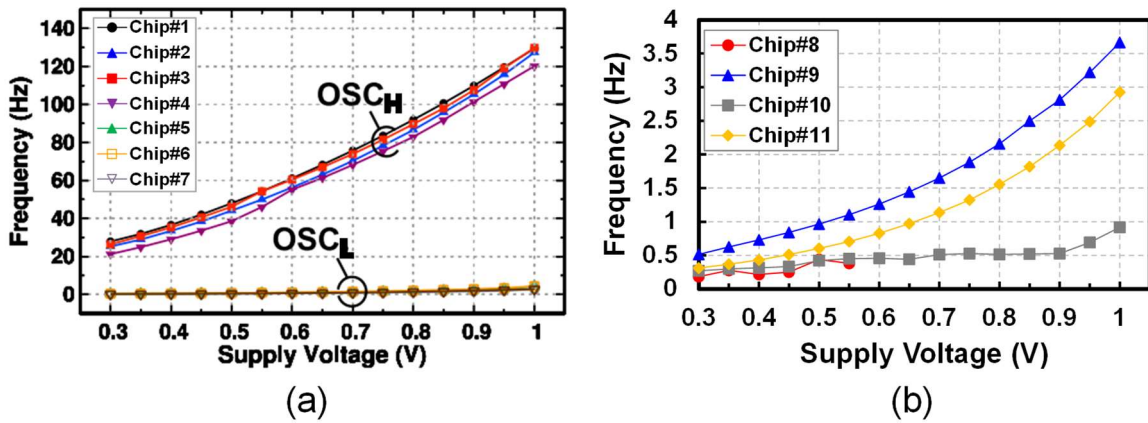
Figure 2.8: (a) Measured frequency of OSC_H and OSC_L vs. supply voltage, (b) measured frequency of OSC_L vs. supply voltage.

Note that the supply voltage range of 0.3–1.0 V in Figure 2.8 is provided by an independent voltage source to obtain accurate measurement results. However, in a voltage-oriented glucose-based BFC, the output voltage can only attain 370 mV with a 30 mM glucose solution [53]. The series-connection of solar cells for a high output voltage reminds us if we can stack multiple BFC for appropriate output voltages. The answer may be negative because the surrounding fluid with its impedance affects the output voltage of the stacked BFC. One of the solutions is to suppress supply voltage down to 0.3 V or lower. An example of this solution is given in Section 5.2. Another direction is not using BFC as a supply, but as a sensing voltage for biasing. This technique doesn't require a BFC voltage of 1.0 V because the BFC is used to tune the current of a voltage-controlled current source. The detailed design of this technique will be given in the next two chapters. Since the main purpose of this work is to prove a new paradigm for CGM contact lenses, simplified building blocks are adopted without deep optimization.

The control signals from the divider are for the energy harvester and TX control. It's worth mentioning that the leakage power consumption of the SVM is only 103 pW at 0.3-V V_{BFC} during the holding time confirmed by post-layout simulation, which makes the BFC-powered scheme feasible.

2.3 Measurement Results

The chip micrograph fabricated in 65-nm CMOS technology is shown in Figure 2.9. The total active circuit area of the proposed system is only 0.413 mm^2, which is feasible to be implemented on contact lenses. The measurement setup for the TX verification is shown in Figure 2.10, which adopts the same setup as the reference [14] because the same on-chip antenna and transmitter circuits are used in this work.

Since this design adopts an on-chip storage capacitor rather than an off-chip one, the capacitance values are <1 nF/mm^2. The available energy can only afford TX to operate for tens of ns. This requires the receiver (RX) to operate continuously and have the ability to

extract the signal from noises. On the other hand, the size of capacitors is the main reason that limits the communication distance because it determines the total current flowing through TX. To guarantee the receiver with a high signal-noise ratio, the gain horn antenna of RX is placed 10 cm away from the test chip, which is the same configuration as the reference [14]. Both of them have a storage capacitance of 30 pF. The high gain of the amplifier improves the sensitivity to signal detection. This kind of energy-budget-unbalanced TX/RX configuration is beneficial for energy-harvesting sensors because their transmission power budget is usually much lower than their RXs.
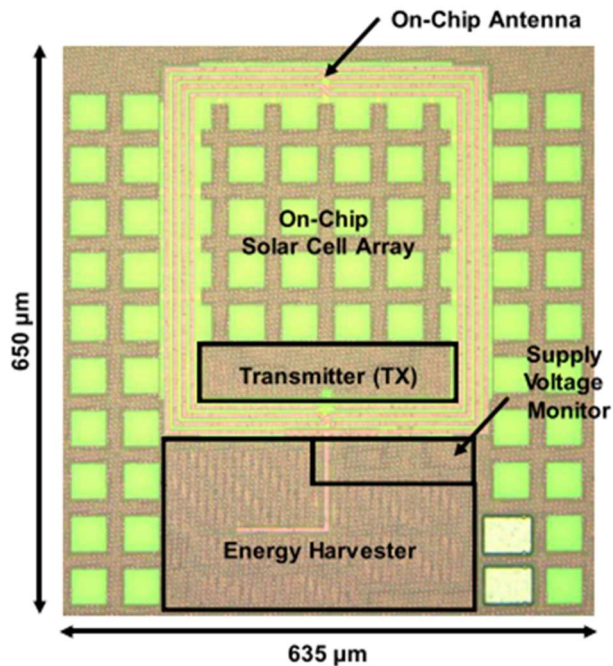
Figure 2.9: Chip micrograph of the biosensing IC.
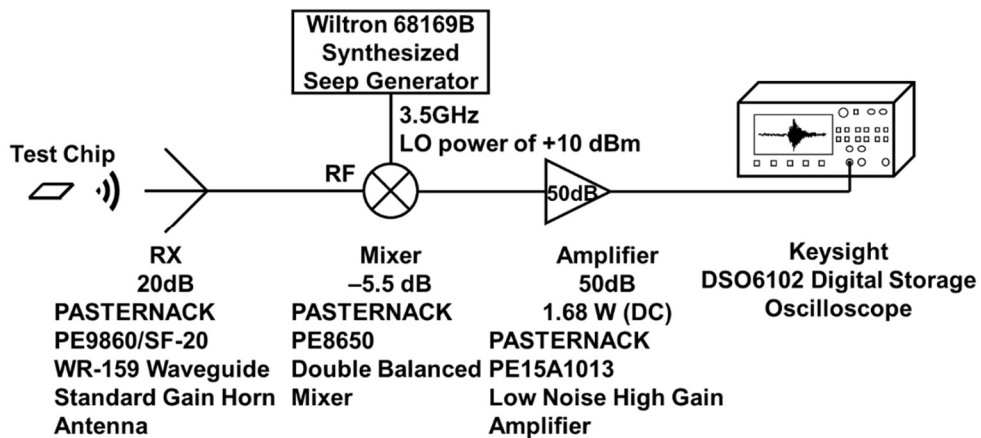
Figure 2.10: Measurement setup for the TX verification.
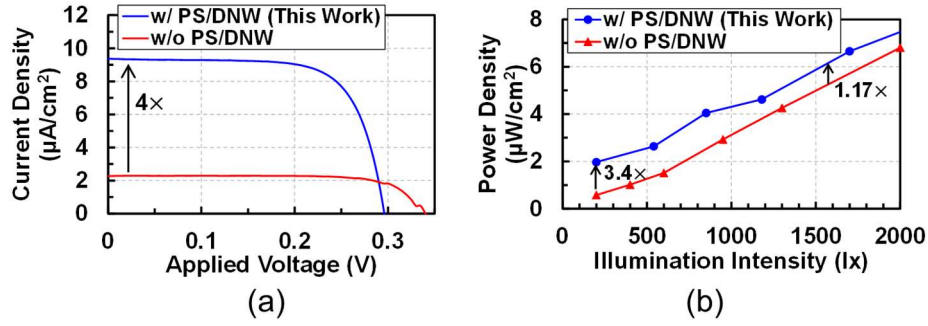
Figure 2.11: Measured performance of (a) current density of the solar cells at 200 lx, (b) power density of the solar cells.

Figure 2.11 (a), (b) plots the measured results of the on-chip solar cell implemented in 65-nm CMOS technology. As a comparison, two types of solar cells, i.e., with and without using the PN junction, PS/DNW, are implemented with the same area efficiency, which means the area size of NW and PW are the same. The measured I-V characteristic of the on-chip solar cell shows that the solar cell with PS/DNW used in this work improves 3× current density from the solar cell without using PS/DNW at 200-lx illumination intensity. Because the area size of PS/DNW is the largest among the three kinds of diodes, thus providing the largest current in a dim environment. The measured output power density of the solar cell with PS/DNW at 200 lx is 1.97 µW/cm^2, which is the 3.4× power density of the solar cell without PS/DNW. However, as the PS/DNW diodes lie beneath the other two, the light reaching the PS/DNW is constrained, limiting the output voltage and current. Even though the illumination intensity increases upon 1000 lx, the power density benefit from using PS/DNW is almost kept the same, as shown in Figure 2.11 (b).

As shown in Figure 2.12, although the open-circuit voltage of the solar cell used in this work is smaller due to the low output voltage of PS/DNW, it shows less sensitivity to the illumination intensity because the parallel connection of photodiodes can relieve output imbalance. The supply voltage for the TX is stabler so that the operating frequency of the TX has less deviation from the desired one.
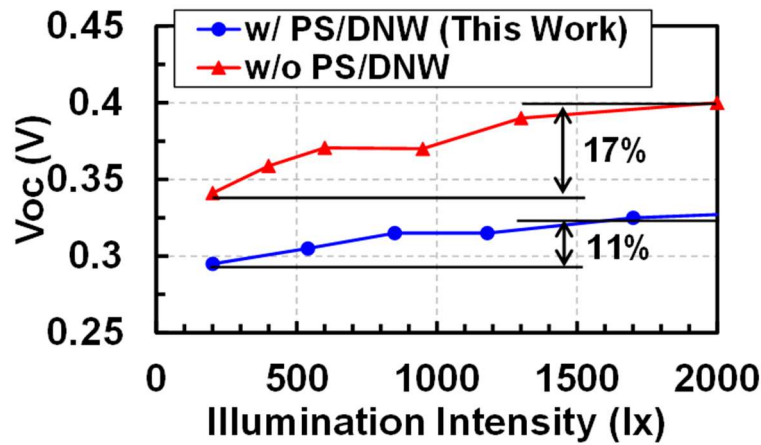
Figure 2.12: Measured open-circuit voltage of the solar cells.
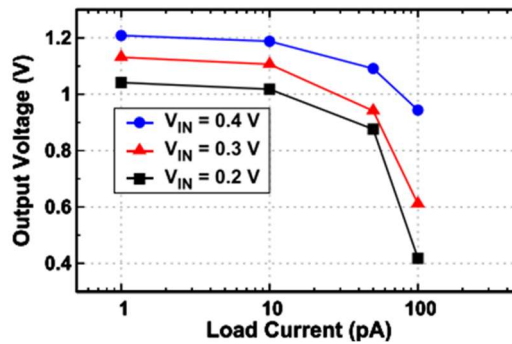
Figure 2.13: Measured output voltage of the energy harvester vs. load current.

Figure 2.13 plots the measured performance of the energy harvester. The energy harvester receives a minimum input of 200 mV and achieves an output larger than 1 V in a load current region below 10 pA while consuming 380 pW. Considering the simulated leakage current of the stacked power gating switch is 29 pA during TX sleep time with a V_{TX} of 1 V, the measured performance of the energy harvester can well satisfy the TX circuits when solar cells provide a 0.3-V supply voltage. However, the output voltage of the solar cell is always smaller than the open-circuit voltage due to its internal resistance. In addition, it can be observed from Figure 2.13 that output voltage V_{TX} changes as V_{IN} changes. This poses a challenge to a stable data readout because V_{TX} can also affect the transmission frequency. In order to achieve a stable performance of the TX, it's better to operate the biosensing system under an illuminated environment to obtain a stable and high solar cell output voltage.
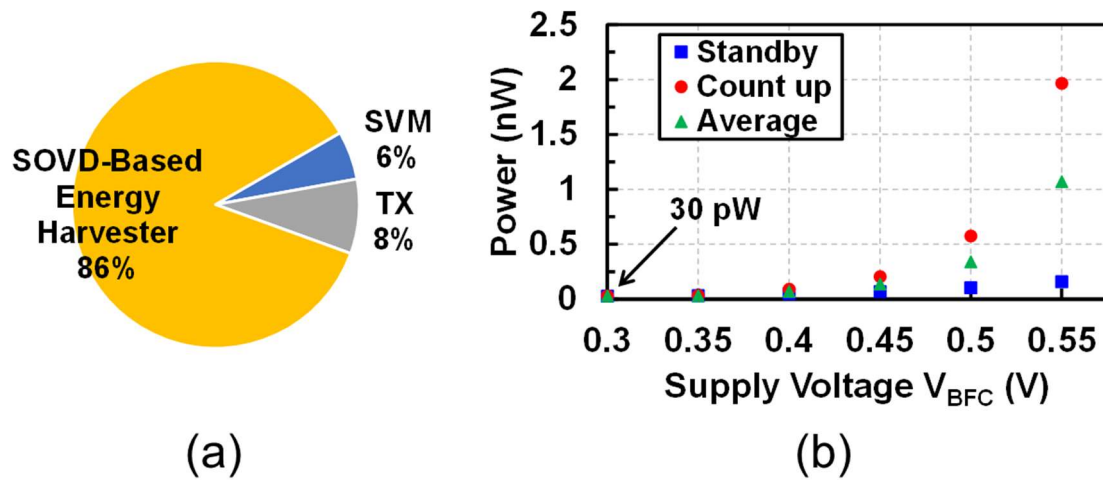
Figure 2.14: (a) Simulated power breakdown of the entire system, (b) measured power consumption of the SVM vs. supply voltage from BFC.

The simulated power breakdown is shown in Figure 2.14 (a). The SOVD-based energy harvester is the dominant part of power consumption because of the voltage up-conversion for TX. The power consumption of TX is only 8% due to the duty-on time in 10s of ns level, which is much shorter than one cycle time of 300 ms. Figure 2.14 (b) shows the measured power consumption of the SVM vs. supply voltage from BFC. The power consumption during standby and counting-up are different. The average power consumption during one cycle time is below 1 nW.

Table 2.1 shows the comparison to the previous works of BFC-powered systems which integrate TX for wireless communications[14], [43], [44]. The BFC in this work only supplies the power of the SVM and the booster, which is 30 pW in total at 0.3 V. When the same power density of BFC is applied to these systems, the proposed biosensing system only requires a BFC of 0.45 mm^2. The proposed fully on-chip system can achieve 89% BFC area reduction compared to the state-of-the-art. A sub-mm^2 glucose-based BFC [34] is suitable for this solar cell and BFC jointly powered CGM system.

Table 2.1: Comparison to the previous works of BFC-powered biosensing systems.

	TBioCAS'17 [43]	JSSC'18 [44]	BioCAS'18 [14]	This Work
Technology	65 nm	65 nm	65 nm	65 nm
Power Source	BFC	BFC	BFC	**BFC + SC**
Signal Conversion of BFC	Single-oscillator based (PIM)	$\Delta\Sigma$ADC (10-bit digital)	Single-oscillator based (PIM)	**Dual-oscillator based (8-bit digital)**
Transmitter	Inductive coupling	RF power oscillator	RF power oscillator	RF power oscillator
Off-Chip Component	Inductor (5 mm×5 mm)	1 cm loop antenna + 1μF capacitor	Fully on-chip	**Fully on-chip**
Transmission Distance	2 mm	10 cm	10 cm	10 cm
Chip Area [mm^2]	0.0032	0.999	0.15	0.413
Total Power Incl. TX	53 μW	1.15 μW	0.27 nW	1.55 nW (solar cell) 0.03 nW (BFC)[*]
Required BFC area[**] [mm^2]	803,030	17,424	4	**0.45**

[*] Since the biosensing system is integrated with on-chip solar cells, there is no measured power consumption of the entire system due to the existing current generated by photodiodes. Instead, the total power consumption is calculated by post-layout simulation.
[**] Power density: 66 pW/mm^2 (1.32 μW/cm^2×0.05 mM[***]/10 mM) [34] @ 0.3 V BFC output
[***] Tear glucose level [12]

2.4 Conclusions

To tackle the issue of power source in next-generation CGM contact lenses, this work presented a solar cell and BFC jointly powered biosensing LSI system for CGM contact lenses. A solar cell-based energy harvester is introduced as a dedicated power source for the power-hungry TX. A dual-oscillator-based SVM which is powered by BFC is employed as an analog front end to transduce the voltage of BFC to digital codes, and a timer to control the operating timing of the system. The SOVD up-converts the solar cell's voltage above 1 V which satisfies the minimum operating voltage of a direct-RF TX. From the measurements results of the test chip fabricated in 65-nm CMOS technology, the main conclusions of this work can be drawn as follows:

- A solar cell and BFC jointly powered biosensing system was introduced to CGM contact lenses for the first time, which achieved 89% BFC area reduction compared to previous BFC-powered work [14] by allocating a 0.3-mm^2 solar cell as a dedicated energy source of power-hungry wireless TX.

- Compared with previous CGM contact lenses, this work achieved a fully-on-chip design that occupies an area of only 0.413 mm^2. If combined with a 0.45-mm^2 BFC, the total area of the CGM system is 0.863 mm^2. To the best of the author's knowledge, this is the smallest area for a CGM contact lens LSI system.

- This work demonstrated a new paradigm for CGM contact lenses, paving the way to a stand-alone solar cell-powered BFC-input biosensing system targeting practical application scenarios.

CHAPTER III

A Solar Cell-Powered Biofuel Cell-Input Biosensing System with an Off-Chip Antenna for Long-Distance Wireless Communication

3.1 Introduction

As Chapter II proposed a new paradigm, the next generation of CGM contact lenses can be solar cell and BFC jointly powered system, without an external reader module as a dedicated power transfer device. Since most of the glucose detections should be done unconsciously to prevent sudden hypoglycemia/hyperglycemia conditions, stand-alone continuous operation of CGM contact lenses is preferred. The solar cells make it a battery-less continuous-on biosensing system with wireless transmission as an efficient means of data communication. Note that this kind of distributed wireless sensor has been introduced to our IoT society with large-scale numbers (e.g. ExG applications, glucose/lactate concentrations, temperature) for wearable healthcare applications [43], [44], [54], [55]. However, some performance needs further improvement in the applications of CGM contact lenses [11], [13]–[15], [17], [19], [46], [56], [57].

First, the communication distance of current CGM systems is too short to maintain data correct rates. Wireless communication needs a receiver (RX) to receive RF signals. The path between a transmitter (TX) and an RX at a specific frequency is called a channel. In information theory, Shannon's law tells that the theoretical maximum rate at which error-free digits can be transmitted over a bandwidth-limited channel in the presence of noise is given by Equation (3.1)
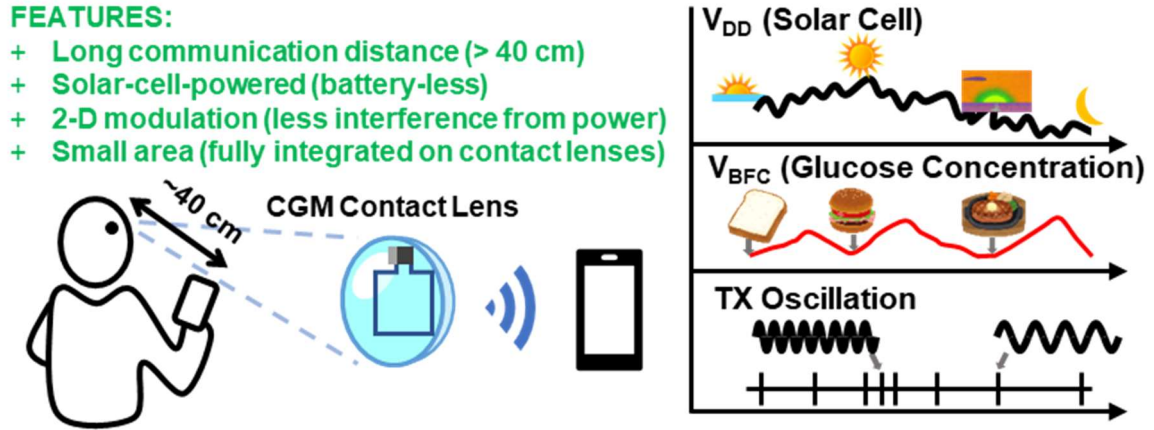
Figure 3.1: Concept and features of the proposed CGM contact lenses.

$$C = W \times \log_2(1 + S/N) \tag{3.1}$$

where C is the channel capacity in bits per second, W is the bandwidth in hertz, and S/N is the signal-to-noise ratio. If the signal strength is weak at a distance, the data can't be recognized correctly with the effect of noise. Then, effective communication can't be achieved at such a distance. The problem of communication occurs in Chapter II when the communication distance is longer than 10 cm. The possible devices which can be employed as an RX are our handsets or smart watches. In normal cases, the average distance between eyes and handsets is approximately 40 cm [58]. That means, the current designs of CGM systems could lose the correct data, and they can not satisfy the viewing distance with handsets as shown in Figure 3.1. To improve communication ability, a key factor is to improve the signal-to-noise ratio. The power of signal transmission should be much higher than the power of noise. Speculating from the design in Chapter II, the small on-chip storage capacitor can't satisfy the power strength of the signal transmission. Therefore, a high-energy-density charge-storage tank is necessary for powerful signal transmission.

Second, solar cell-powered biosensing systems suffer from varying light intensity and conventional modulation methods incur sensing error and bit errors which may confuse the users with incorrect information. The previous work in Chapter II adopted frequency-shift-keying (FSK) modulation to send an RF signal. However, the frequency of TX could be affected not only by the bit of capacitance but also by the powering voltage of TX which is

driven by solar cells. Some other works used pulse interval modulation (PIM) [43] with double pulses to reflect varying supply voltage information with targeted temperature information, which provides us with an example to solve the issue of varying light intensity. Multiple pulse intervals add one more dimension of information to a single pulse interval. This work proposes to combine FSK and PIM to modulate RF signals. Compared with the previous works using PIM, the FSK-PIM-combined TX adds another dimension to the single modulation, to send out supply voltage information together with sensed bio-information. By two-dimension (2-D) information, the users can distinguish the glucose changing trend with less interference from the varying supply voltage.

Third, powering a supply voltage monitor (SVM) directly by a BFC requires too much power from it. Although the previous work in Chapter II has made a sub-mm^2 BFC feasible, the power consumption at several nW when the supply voltage of SVM exceeds 0.3 V is still too much for a BFC. To further reduce the load of BFCs, this work employs a BFC as a dedicated sensing component, with no need to power an SVM. The BFC inputs its voltage to a voltage-to-frequency converter which is powered by solar cells. The low-power relaxation oscillator with low supply sensitivity continues to be used in this work, working as a timing clock for the entire system and a reference frequency for the voltage-to-frequency converter. The dual function of the relaxation oscillator saves power budget. This BFC-input configuration of sensing front ends separates powering components and sensing components thoroughly, only requiring pA current from BFCs.

Fourth, the solar cell-powered SOVD-based energy harvester can't up-convert the voltage enough for long-distance transmission. The powering voltage of TX is only 1.0 V in Chapter II, which drives a center-tapped on-chip antenna. However, to store more charge in a capacitor, a higher voltage is required. Therefore, this work designs a voltage-oriented energy harvesting that doubles the output voltage. The solar cells in Chapter II focus on output current density because the fully-on-chip system should make full use of the area. However, the solar cell's output voltage is degraded to some certain level. This work

improves the open-circuit voltage to enhance the output voltage of energy harvesters by re-connecting the wire connection of the solar cells. By excluding the photodiode PS/DNW, the new solar cell achieves at least a 16% output voltage increase, which is suitable for voltage-oriented energy harvesters. Dickson charge pump is adopted for a high voltage up-conversion instead of a three-stage SOVD. The TX circuit is re-designed to specialize in the features of high output voltage and high radiation power.

As described in Chapter I, wireless communication can be applied to normal cases of CGM which is suitable for most people with diabetes. To facilitate the application of CGM contact lenses in normal cases, this work makes efforts to extend wireless communication distance for data connectivity. This work presents a battery-less system for CGM contact lenses featuring a 2.4 GHz TX that combines FSK and PIM to overcome the impact of unstable solar power as shown in Figure 3.1. The measured maximum power consumption of 126 nW at 0.37-V supply voltage was obtained from a test chip fabricated with a 65 nm CMOS process. A transmitted signal was received at a 40-cm distance, which makes it feasible for contact lenses to communicate with handsets in normal scenarios.

Section 3.2 describes the system and circuit design of the proposed solar cell-powered BFC-input biosensing system. Section 3.3 shows the measurement results of the test chip and the implemented prototype. The conclusions are given in Section 3.4.

3.2 Design Details of Battery-Less CGM Contact Lenses

3.2.1 Architecture of Proposed Battery-less CGM Contact Lenses

Figure 3.2 shows the detailed block diagram of the proposed system consisting of a TX circuit, a charge pump-based energy harvester to up-convert the supply voltage (VDD) to V_{TX}, and a voltage monitor (VM) [49] as an analog-to-digital converter. The BFC [34], as the sensing interface, applies its voltage V_{BFC} to the header PMOS to control the frequency (CLK_H) of a high supply-sensitivity oscillator (OSC_H). The VM converts V_{BFC} to an 8-bit BFC voltage code and controls the operation timing of TX by a low supply-sensitivity

oscillator (OSC_L). Compared with the previous SVM [49] whose average power consumption of 30 nW is totally supplied by BFC, the VM in this work is supplied by on-lens solar cells, and BFC only biases the gate of the PMOS to modulate CLK_H. Therefore, the area of the BFC can be further reduced, because it only consumes a current at pA level.
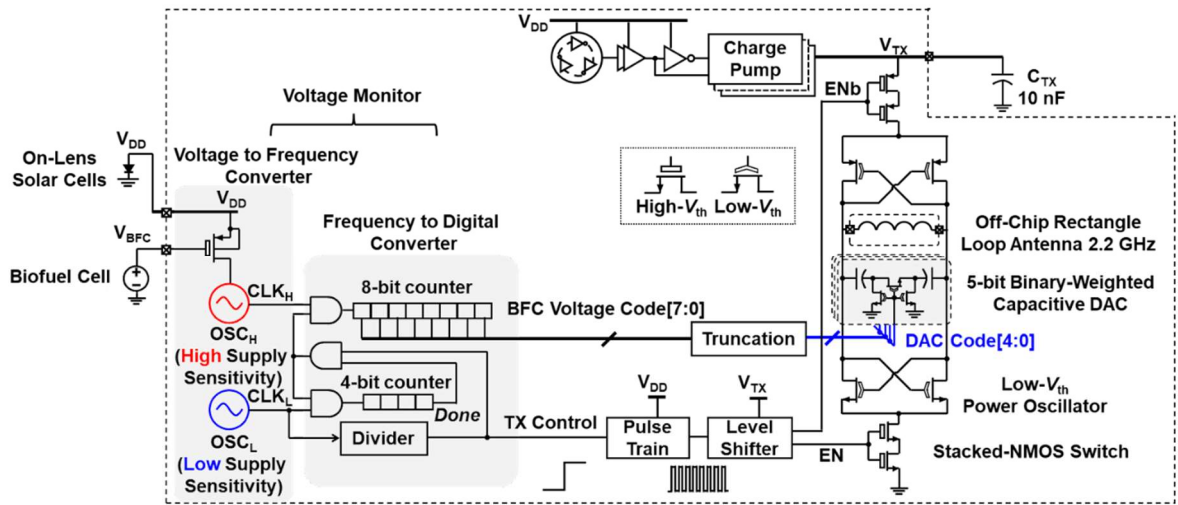
Figure 3.2: Block diagram of the proposed biosensing system with the TX circuit at the transistor level.
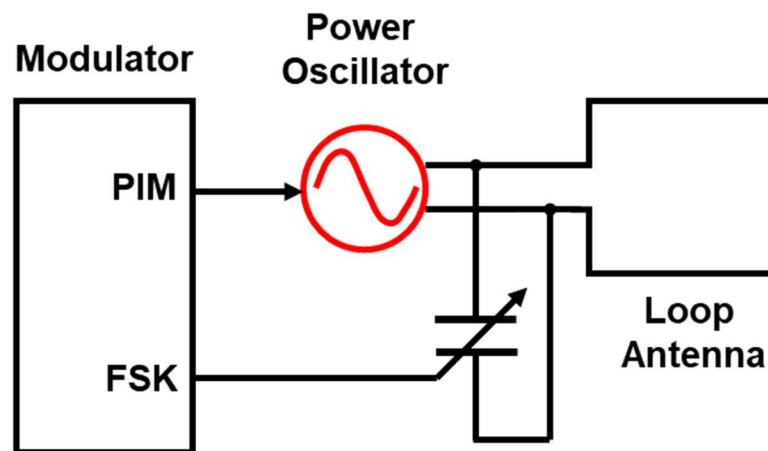
Figure 3.3: The proposed FSK-PIM-combined modulator for direct-RF wireless TX.

3.2.2 An FSK-PIM-Combined Transmitter with a High Radiation Efficiency Antenna

The conventional modulation methods used in previous works, such as OOK and PIM, have disadvantages in battery-less CGM contact lenses, as RF signals are prone to be lost due to weak transmission power. This becomes a fatal issue for data error rates. To guarantee the accuracy of signal transmission without relying on error-correcting coding, this work proposes an FSK-PIM-combined 2-D modulation for a TX with an off-chip antenna in Figure 3.3, enlightened by wide tuning-range voltage-controlled oscillators [59], [60].

In FSK-PIM-combined modulation, as shown in Figure 3.4 (a), the TX frequency is a function of V_{TX} and V_{BFC} corresponding to different codes, and the period of signals is controlled by OSC_L as a function of VDD. The 8-bit supply voltage code is passed to the 5-bit binary-weighted MIM capacitive digital-to-analog-converter (DAC) after truncating the least significant bit (LSB), most significant bit (MSB), and the bit next to MSB, to modulate the TX oscillation frequency. For the consideration of the trade-off between area and accuracy, a 5-bit capacitive DAC with a total size of 0.13 mm × 0.045 mm and 931 fF is employed. Rather than asymmetric placement in reference [46], the capacitors are placed in a common-centroid pattern shown in Figure 3.5 to minimize the mismatch among each bit. With these techniques, coarse frequency tuning is controlled by V_{TX}, and fine frequency tuning is controlled by V_{BFC}. The TX achieves a tuning range from 2.1–2.3 GHz as shown in Figure 3.4 (b), simulated in Spectre RF with extracted parasitic components from the layout. The TX control signal triggers an 8-pulse train to switch on the TX, whose pulse width is inversely proportional to VDD by a stacked-inverter chain. As V_{TX} increases with VDD without a voltage regulator, if the received signal frequency is confirmed, the transmitted bit code can be inferred.
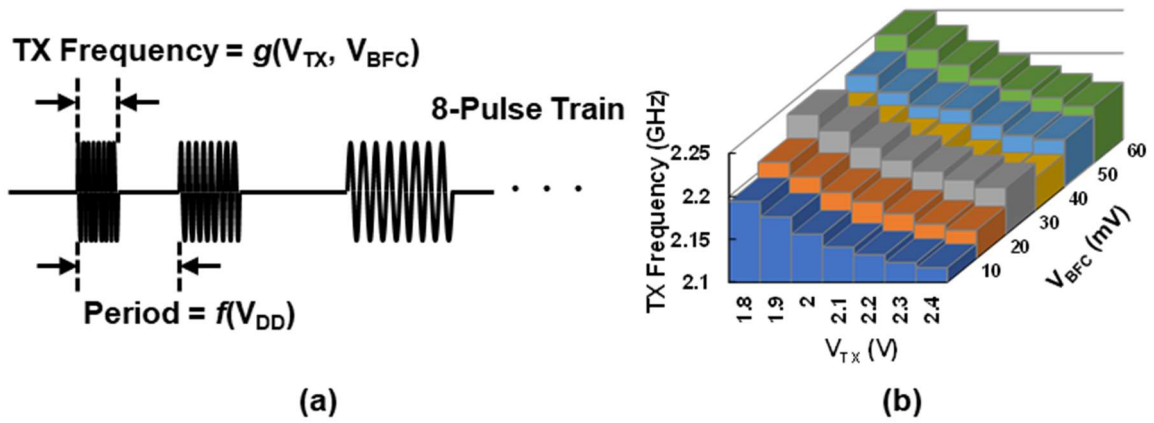
Figure 3.4: (a) Concept of the proposed FSK-PIM-combined modulation, (b) simulated TX oscillation frequency as a function of V_{TX} and V_{BFC}.
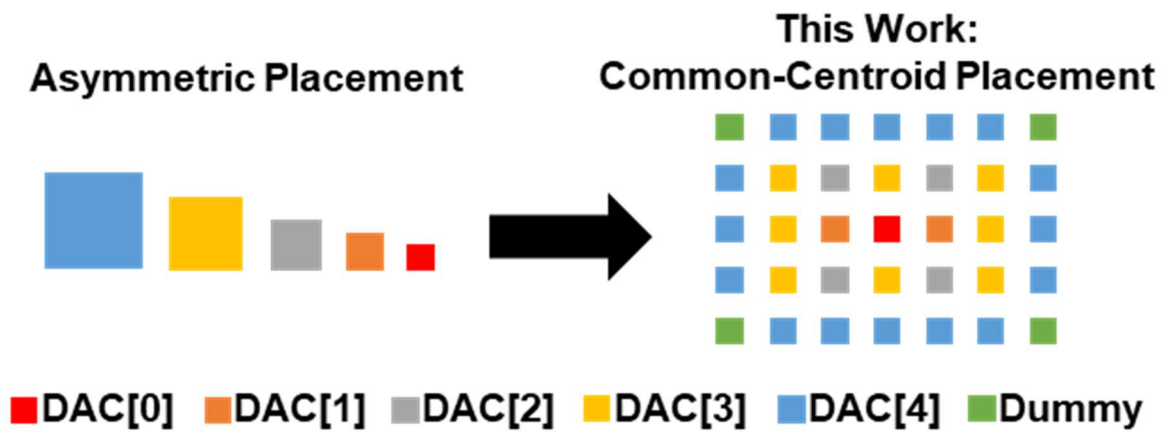
Figure 3.5: Illustration of the common-centroid placement of the MIM capacitors for the 5-bit DAC.
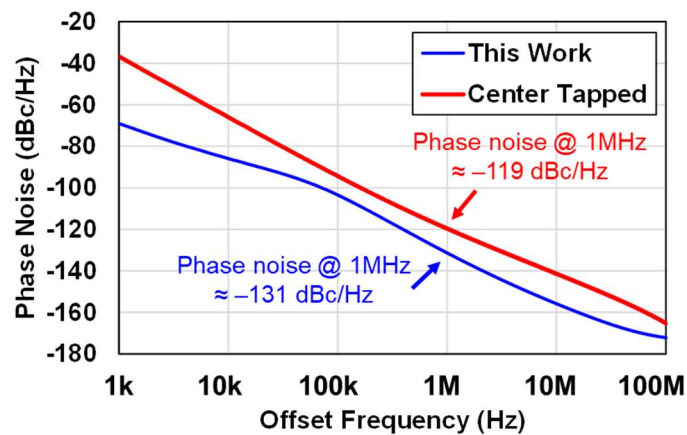
Figure 3.6: Simulated phase noise of LC oscillator in this work, and a 2.4 GHz center-tapped LC oscillator with single cross-coupled pair.

41

The TX circuit utilizes the direct-RF power oscillator architecture [51], [56] for short active time operation with a 3 mm × 4 mm off-chip loop antenna whose inductance is 15 nH. The antenna operates both as a resonant and radiative element, eliminating the necessity for a power amplifier and bulky matching networks. Although the 3 mm × 4 mm antenna has a higher Q-factor while operating at 900 MHz, 2.1–2.3 GHz is chosen because the antenna has a higher radiation efficiency near 2.4 GHz [51]. It should be noted that the target frequency is 2.4 GHz, but this design adopted a near-2.4 GHz band to avoid interference from existing RF in the measuring environment without a shielding box. The two cross-coupled pairs as power oscillators are designed with low-V_{th} devices for a fast start of oscillation. Compared to the design with single cross-coupled pair [51], this free-running LC oscillator achieves a simulated phase noise of –131 dBc/Hz at 1 MHz offset as shown in Figure 3.6, which is lower than –119 dBc/Hz of a 2.4 GHz center-tapped LC oscillator with single cross-coupled pair, when both of them are oscillating with the same amplitude.

3.2.3 Charge Pump-Based Energy Harvester

To drive the TX circuit, this system integrates an on-chip Dickson charge pump (DCP) which was employed in reference [57], to up-convert VDD to V_{TX} above 1.8 V. In the previous work with fully-on-chip design [14], the oscillation attenuates quickly because the on-chip capacitor can not sustain mW-level power oscillation. The issue becomes severe in the FSK case. However, a too-large capacitor leads to power and area overhead. As a result of the above considerations, a 10-nF off-chip capacitor, C_{TX}, is employed to store the charge. The stacked NMOS/PMOS switches using high-V_{th} devices minimize the leakage current during standby mode. Meanwhile, an "interleaved" layout technique [61] is applied to the stacked NMOS/PMOS switches to increase the output power and efficiency. To start the oscillation, the pulse train is level-shifted to full swing at V_{TX} by a level shifter [62] to enable the stacked switches, maximizing the I_{on}/I_{off}. This configuration extends the transmission distance and mitigates the V_{TX} drop to below 30 mV even with mA-level operating current through the TX.
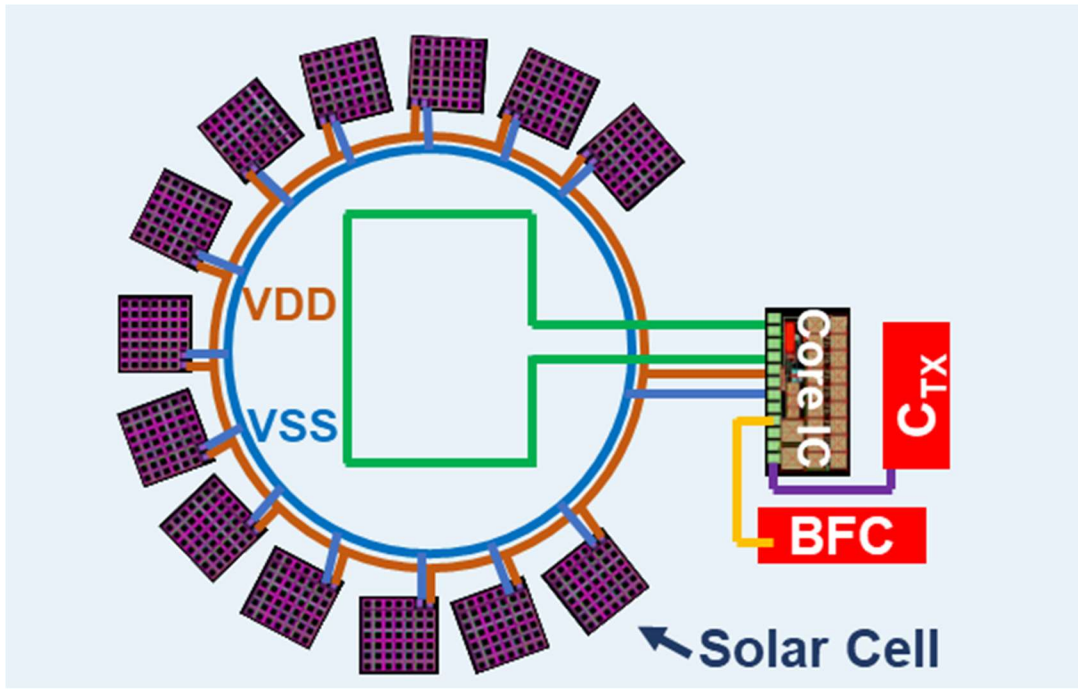
Figure 3.7: Illustration of proposed biosensing system for CGM contact lens.
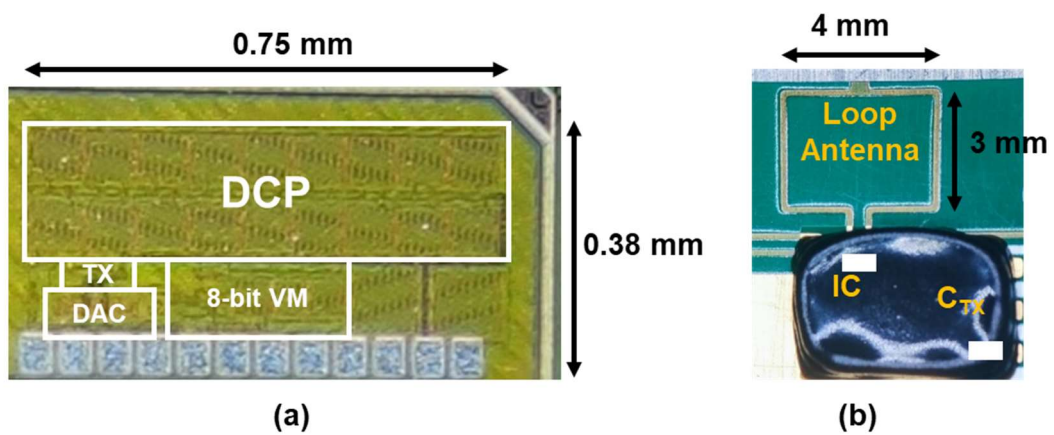
Figure 3.8: Photograph of the chip fabricated in a 65nm CMOS LP process, and

implemented prototype with an off-chip loop antenna.
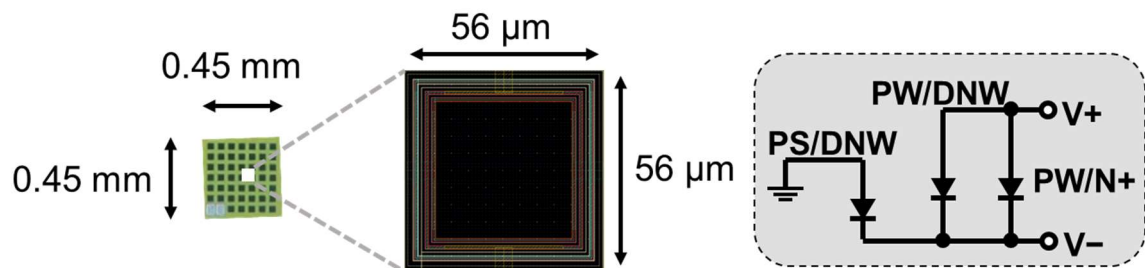
Figure 3.9: The implemented solar cell, the layout of a unit cell, and its schematic of

photodiode connection.

43

3.3 Measurement Results

The assembling of the proposed CGM contact lens is illustrated in Figure 3.7. It consists of solar cells, an off-chip antenna, core IC, BFC, connecting wires, and C_{TX}. The practical prototype with all these components is not implemented yet due to the availability of solar cells and BFC. Therefore, this work only verified the function of distributed components. There are 13 solar cells arranged around the visual axis, whose number is tentatively determined according to the simulated maximum power consumption. The solar cell chips are separated from the core IC because the total area will attain nearly 3 mm^2 which is not convenient to assemble on a curved surface of a contact lens. The separated components with small pieces bring flexibility to the assembling. Another merit is that the number of solar cell chips can be chosen freely even if the core IC design is changed.

The proposed core circuit was fabricated in a 65 nm CMOS LP process, occupying an area of 0.75 mm × 0.38 mm. The chip photograph is shown in Figure 3.8 (a). The 3 mm × 4 mm copper antenna with a thickness of 18 μm is printed on FR-4 material, which is directly bonded to the chip, which is shown in Figure 3.8 (b). The chip and C_{TX} are encapsulated by epoxy resin in the prototype. The solar cell chips are not included in this prototype. The system-level prototype including all components will be implemented in future work.

The solar cells were implemented by the same CMOS process, and their photograph and layout are shown in Figure 3.9. It should be noted that the photodiode connection is different from the solar cells in Chapter II. The PS/DNW photodiode is not adopted and does not provide a current in this work.
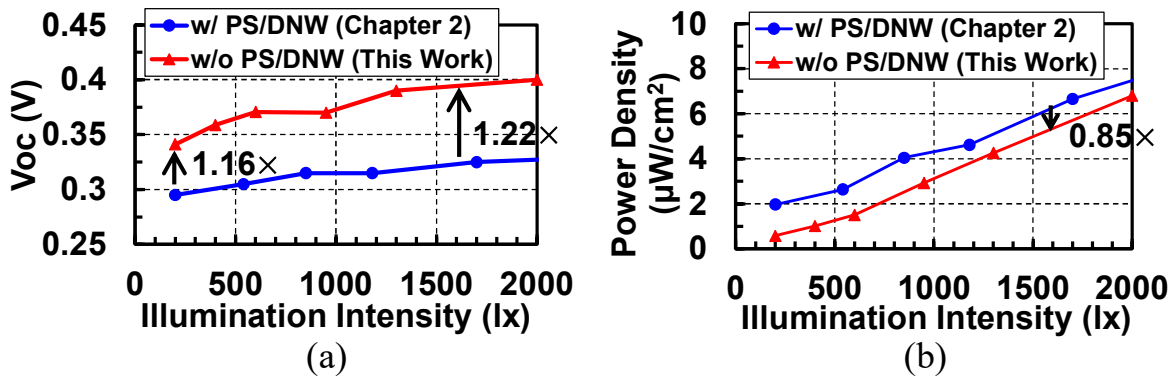
Figure 3.10: Measured open circuit voltage and power density of implemented solar cells vs. illumination intensity.
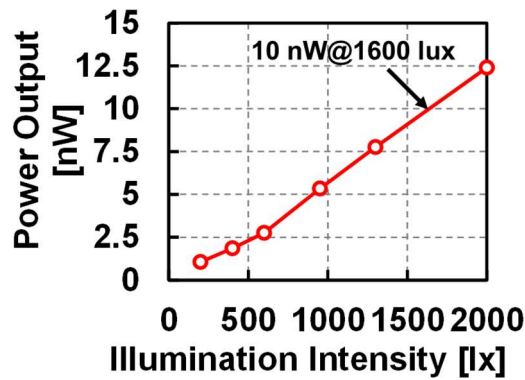
Figure 3.11: Measured output performance of single solar cell unit (0.45 mm × 0.45 mm) vs. illumination intensity.

Figure 3.10 (a) and (b) show the measured performance comparison of solar cells in this work and in Chapter II, which are implemented in the same area efficiency. The open-circuit voltage of the solar cell of this work is within 0.34–0.4 V, improved at least 16% from that of the conventional type at the cost of power density. However, the power density of the solar cell of this work can be still maintained at 85% of the conventional type in 1600-lx light. The implemented 0.45 mm × 0.45 mm solar cell unit can provide 1–10 nW in office-room ambient light (200–1600 lx) as shown in Figure 3.11. This implies that the maximum suppliable power by the 13 on-chip solar cells is 130 nW at sub-0.4 V in 1600-lx light, which is sufficient for the operation of the proposed CGM system. Due to the low power consumption, solar cells usually do not need to operate at the maximum power point. Therefore, VDD can still be kept within 0.3–0.4 V.
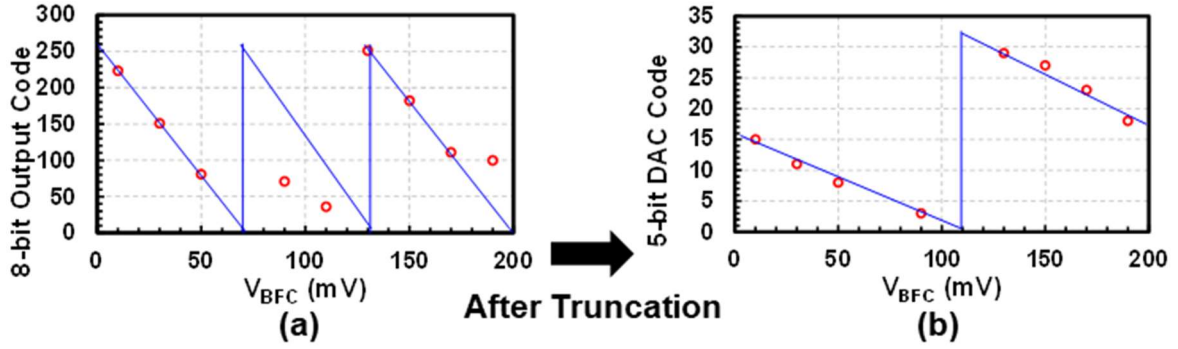
Figure 3.12: Measured results of (a) BFC voltage codes @VDD = 0.6 V, (b) DAC modulation codes after truncation @VDD = 0.6 V.
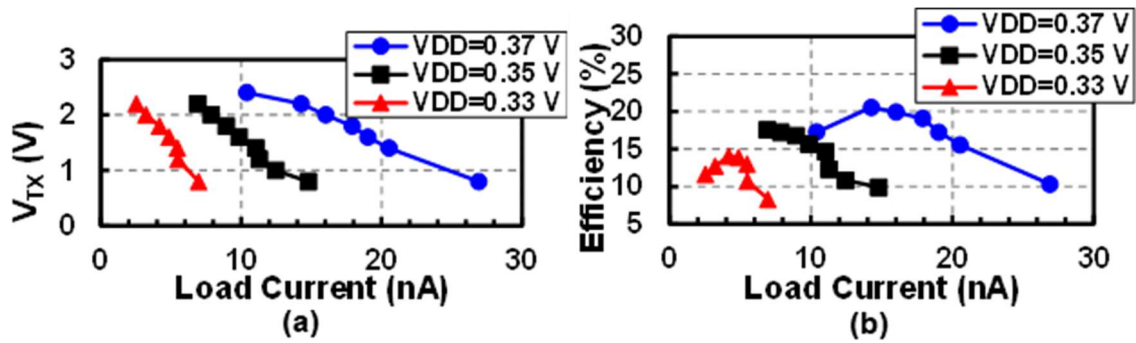
Figure 3.13: Measured results of (a) output voltage, and (b) efficiency of the DCP without C_{TX}.

Figure 3.12 (a) and (b) show the measured 8-bit BFC voltage codes and corresponding 5-bit DAC codes after truncating 3 bits at 0.6-V VDD. As obtained from the results, good linearity between V_{BFC} and codes can be kept after truncation. Another merit of truncation is that the repeat of bits is reduced within the V_{BFC} range of 0–200 mV, as there are two overflows of bits before truncation, but only once after truncation. It should be noted that the operational VDD is higher than the assumed one, which can be tackled by stacking solar cells in a dedicated source. The peak power consumption of the VM at 0.6-V VDD is 8 nW, which can be easily covered by solar cells.

Figure 3.13 (a) and Figure 3.13 (b) show the measured performance of the DCP. Because the stacked NMOS/PMOS switches limit the leakage current at tens of pA, the V_{TX} can be above 1.8 V for a high energy density in the off-chip capacitor. The peak efficiency of the DCP increases with VDD, attaining 20% when VDD is 0.37 V.
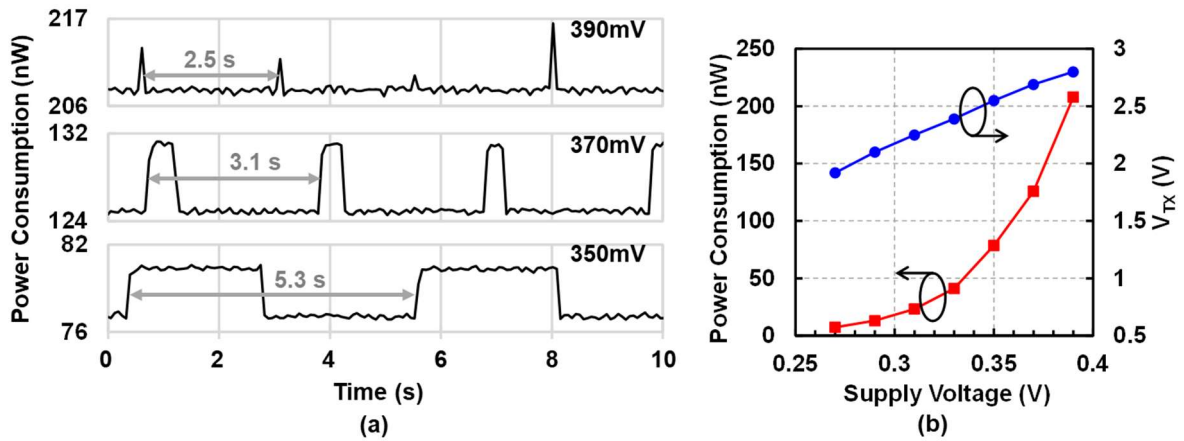
Figure 3.14: Measured results of (a) transient power consumption, (b) V_{TX}, and average power consumption of the chip without passive components.

Figure 3.14 (a) shows the measured transient power consumption of the chip, which indicates the pulse timing of transmission. The period of the pulse is 5.3 s, 3.1 s, and 2.5 s, when VDD is 350 mV, 370 mV, and 390 mV, respectively. Therefore, the solar cell's voltage can be distinguished through the period of received signals. The pulse width is also reduced as VDD increases since the delay time in the pulse train is shortened. It's worth mentioning that some transmission signals could be lost in the RX due to the weak pulse, e.g. the third pulse in Figure 3.14 (a) at 390-mV VDD. However, it doesn't affect information communication. Because the bit code can be inferred from the TX frequency and pulse width, as long as the RX received a signal for a single time. This is the advantage of FSK-PIM-combined modulation.

The measured average power consumption of the chip without passive components is 126 nW at 0.37 V, as shown in Figure 3.14 (b). If the CMOS solar cells operate at 1600 lx which is typically an indoor ambient-light environment, 2.6 mm^2 of them are necessary [57], which are accommodatable in contact lenses.
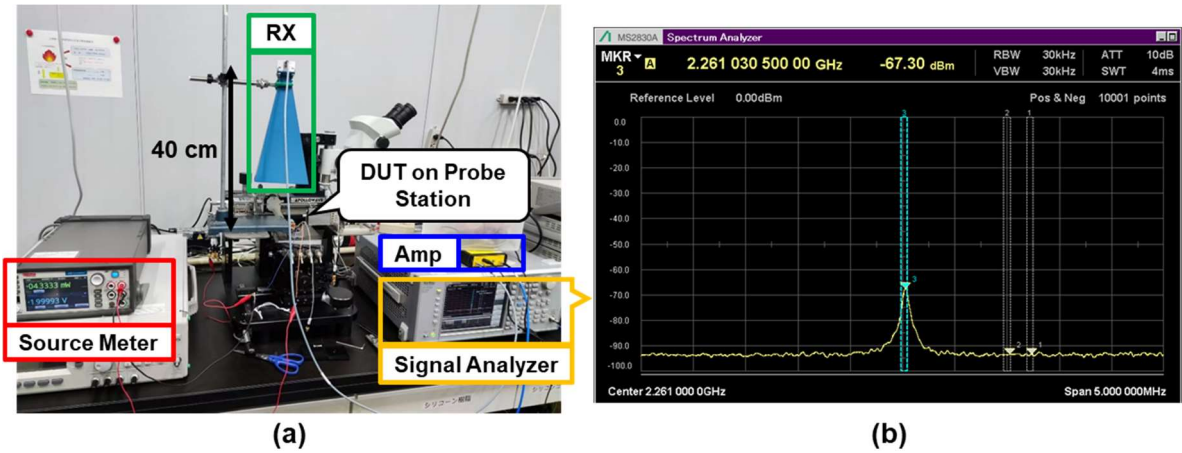
Figure 3.15: (a) Picture of RF measurement setup, (b) power spectrum of a received signal.
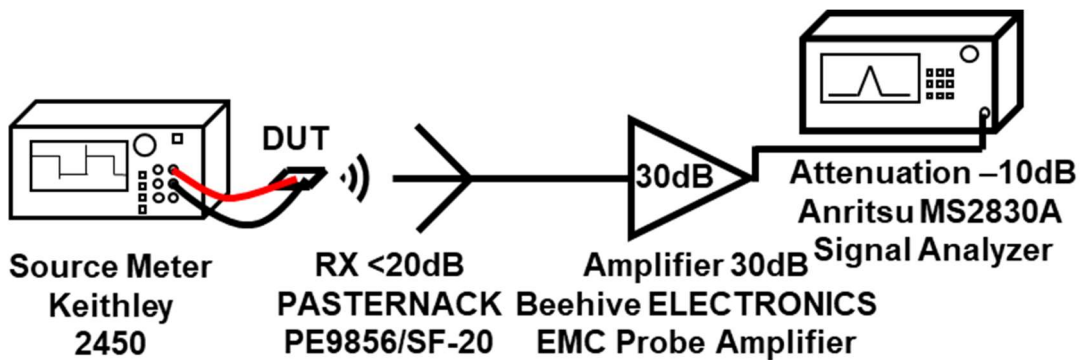
Figure 3.16: link budget of the RF signal.

Figure 3.15 (a) shows the picture of the experiment setup of TX and RX. A source meter (Keithley, 2450) is used to supply the power through a probe. A wireless signal with a 2.26-GHz center frequency was received by the gain horn receiver antenna (PASTERNACK, PE9856/SF-20), which was verified by the signal analyzer (Anritsu, MS2830A) as shown in Figure 3.15 (b). The distance from TX to RX is 40 cm. A received signal peak power of –67 dBm at V_{TX} of 2.1 V after 30-dB amplification by the amplifier (Beehive, 150A) and 10-dB attenuation by the signal analyzer was confirmed.

Considering that the gain horn antenna is originally designed for 8.2–12.4 GHz, the actual total gain is less than 40 dB as shown in the link budget in Figure 3.16. The maximum received power at a 40-cm distance is approximately –100 dBm, which is above the dead zone (–110 dBm) of handsets. The power spectrum bandwidth of the signal is less than 1 MHz, making it possible to distinguish each signal's frequency.
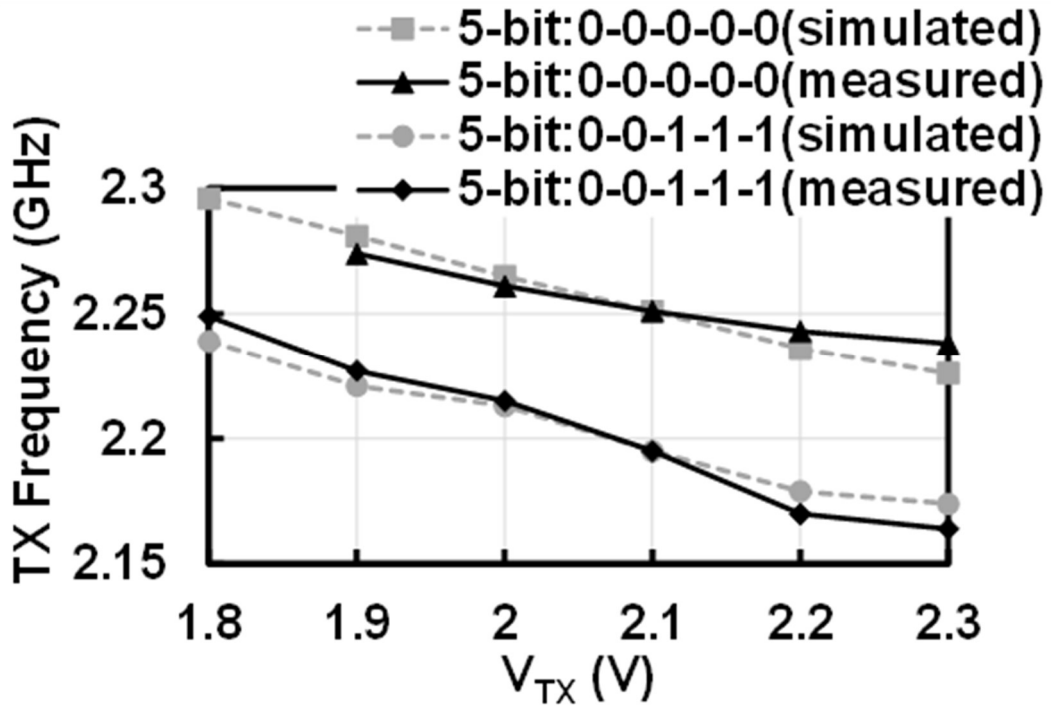
Figure 3.17: Measured and simulated TX frequency vs. V_{TX} without calibration.

The TX frequency is plotted in Figure 3.17 at different V_{TX} and two batches of DAC codes, which agrees with the simulated results without any calibration. It is not a heavy task to tune the center frequency to 2.4 GHz by reducing the capacitance of the DAC, which requires no area overhead. Meanwhile, V_{TX} ranging from 1.9–2.8 V has good linearity with VDD, as shown in Figure 3.14 (b), which helps to improve the resolution of the modulated TX frequency. It should be noted that although the linear relationship between V_{TX} and VDD exists among different chip samples, V_{TX} can change according to the change of VDD in real time. That means V_{TX} could be up and down when users move outdoors and indoors. This poses a challenge to practical applications because we can't limit users' movements during using CGM contact lenses. Fortunately, this work doesn't require VDD to be stable for a long time, because the VDD voltage can be known from the pulse width as Figure 3.14 (a). The users only need to keep VDD relatively stable during one detection which takes no longer than 10 s. This may be easy for users indoors under a stable environment, but may not be easy for users outdoors who are in a complicated environment. Therefore, this point should be improved in the future to make it suitable for a more complicated scenario.

Table 3.1 summarizes the performance of the proposed CGM system and compares it to the prior state-of-the-art CGM contact lenses[11], [14], [56], [57]. This system does not require any external reader module, improving comfort and flexibility compared to reference [11]. The large antenna size can achieve a transmission distance of 40 cm, which is 4× the length of that in reference [14]. By removing batteries, this design achieves 7.7× area reduction compared to the reference [56]. To the best of the authors' knowledge, it's the first time to implement FSK-PIM-combined TX on a system for CGM contact lenses, which adds one more dimension of information compared to the reference [57].

Table 3.1: Comparison of Prior State-of-the-art CGM Contact Lenses.

	ISSCC'11 [11]	BioCAS'18 [14]	VLSI'19 [56]	ESSCIRC'21 [57]	This Work
Methodology	RFID	Wireless TX	RFID + Wireless TX	μLED	Wireless TX
Process	0.13 μm	65 nm	0.18 μm	65 nm	65 nm
Supply Voltage [V]	1.2 (regulated)	0.165−0.39	2.0−3.8	0.31−0.4	0.27−0.37
Energy Source	Wirelessly (RF-2.4 GHz)	BFC	Wirelessly (RF-433 MHz) + Battery	Solar cell	**Solar cell**
Sensing Interface	Potentiostat	BFC	Potentiostat	BFC	BFC
Modulation Scheme	FM-LSK	OOK	LSK + OOK	PIM/PDM	**FSK + PIM**
TX Frequency	N/A	4.1 GHz	433 MHz	N/A	2.1−2.3 GHz
Off-Chip Component	Antenna	Fully on-chip	Antenna + Battery	SC + LED + Cap	Antenna + Cap
Transmission Distance	15 cm	10 cm	1 cm (LSK) 1 m (TX)	Display on lens	**> 40 cm**
Total Area [mm^2]	0.5 (chip)	0.15 (chip) 4 (BFC)	2.25 (chip) 20 (battery)	0.5 (chip) 3 (solar cells)	0.29 (chip) 3 (solar cells)
Power (Chip Only)	3 μW	0.27−11.8 nW	143−490 nW	28−144 nW	7.3−126 nW

3.4 Conclusions

In this work, a battery-less biosensing system for solar-cell-powered CGM contact lenses featuring a 2.4-GHz transmitter was presented. The proposed FSK-PIM-combined modulation with 2-D information including TX frequency and pulse width mitigates the impact of unstable solar power and bit error by weak signals. The high radiation efficiency antenna and the high energy density off-chip capacitor help to achieve a transmission distance longer than 40 cm, which allows communication between contact lenses and handsets. The fabricated chip in a 65 nm CMOS process consumes 126 nW at 0.37-V supply, which is manageable by 2.6-mm^2 solar cells in an indoor ambient-light environment. The battery-less design with a small area facilitates full integration on contact lenses. This work demonstrated the concept of the world-first self-powered handset-familiar CGM contact lenses.

CHAPTER IV

A Solar Cell-Powered Biofuel Cell-Input Biosensing System with an LED for Direct Hyperglycemia/Hypoglycemia Warning

4.1 Introduction

As of now, we have explored the possibility of wireless communication for CGM contact lenses in the last two chapters. The wireless communication distance has been extended from 10 cm to 40 cm, which makes communication between contact lenses and handsets feasible. However, there are some issues not been tackled yet. People will not always hold their phones in hand. In most situations, our phones are in our pockets or bags, which are longer than 40 cm away from our eyes. That means the data connectivity is still unavailable for some time. That may cause fatal issues for people with type 1 diabetes because their blood glucose may drop suddenly. Therefore, another method should be auxiliary to a stand-alone TX to warn people of an emergent condition of sudden glucose change.

Some RFID-based prior studies [11], [56], employed wireless RF power transfer to operate the systems on a contact lens. The backscattering communication is more secure than stand-alone TX because the reader module operates by a battery and doesn't worry about the shutdown of electricity. However, an external device, as shown in Figure 4.1, such as a neck-type charger or smart glasses transmitting power at a distance of 15 cm [11] or 1 cm [56], is required, which degrades comfort and eye health. In addition, wireless power transfer is lossy, incurring low energy efficiency.
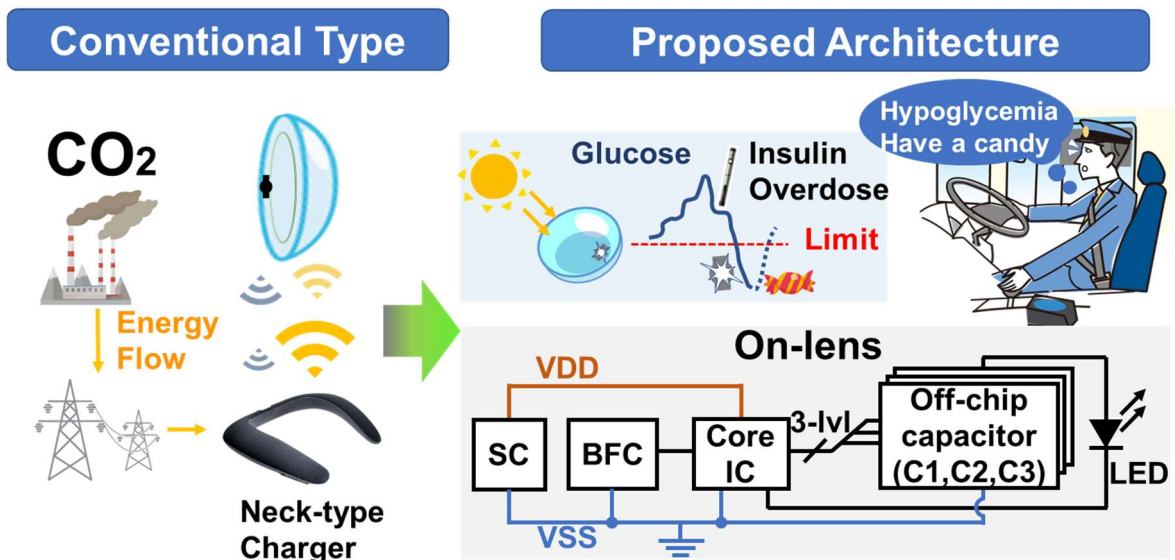
Figure 4.1: Application scenario of proposed CGM contact lens with on-lens displays to prevent hypoglycemia.

Localized information display is an effective approach for eliminating the necessity of external devices, which contributes to a stand-alone RF-less operation. As shown in Figure 4.1, by introducing LED displays on lenses, the glucose information can be displayed directly to the users unconsciously. Besides, by combining with machine learning (ML), hypoglycemia prediction becomes feasible [63]. Therefore, the users can react to the dramatic glucose level change even during driving a car. However, even duty-cycled energy-efficient LEDs require more power than wireless transmitters. The architecture in Chapter III should be further improved and specialized to drive an LED.

The solar cell-powered BFC-input methodology can be used in this work because it's featured for a stand-alone system with a sub-mm^2 BFC. Consequently, BFC is only utilized as a sensing element due to its available sub-nW power [34]. Solar cell (SC) is a promising power source as a localized energy harvester for LED driving on contact lenses which can provide 100s times larger power than BFCs in a unit area [46]. The SC design in Chapter III can be adopted in this work, but is there any way to improve its power density to another level? Considering that the output voltage of SCs in the previous chapters is always lower than open-circuit voltage due to its internal resistance, one possible method to improve the

output power of SC is to reduce its internal resistance. This work breaks down the unit SC into small pieces and parallelly connects them. This method not only improves the area usage efficiency but also decreases the internal resistance of SCs. A 3× power density is achieved compared to the SC in the last two chapters.

To further increase the output voltage of energy harvesters, the three-stage Dickson charge pumps with a pre-booster are designed to drive an LED. The single-stage Dickson charge pump in Chapter III should supply the voltage of TX and other circuit blocks, such as level shifters and buffer drivers. This causes heavy loads for the charge pump and results in output voltage degradation. This work makes the main charge pump a dedicated power source for an LED, without the need to power any other circuit blocks. The relieved load of the main charge pump can up-convert the voltage to 4 V, which can store more charge in capacitors and attain the minimum voltage for lighting an LED.

The BFC-input methodology continues to be used in this work. Note that the supply voltage of the voltage monitor in Chapter III is 0.6 V, which requires a stacking of solar cells. To decrease the supply voltage to 0.4 V which is possible for a single SC unit without stacking, this work designs a ring oscillator as the low-power relaxation oscillator. The ring oscillator is current-starved by a PMOS switch, consuming sub-nW power. The low-power ring oscillator works as a timer clock whose frequency implies the voltage of BFC. This configuration doesn't need a frequency-to-digital converter for a digital readout, reducing power consumption further.

Confronting the varying light density is still an obstacle to using solar power. Since the BFC-input method applies the voltage of BFC to a voltage-to-frequency converter, the continuous change of solar power will affect the output frequency, thus giving incorrect information to users. To mitigate the influence of varying light, this work shortens the required time for one readout and proposes a pulse density modulation (PDM). The PDM burst a series of LED lighting pulses to inform users by the density of pulses. Only 5 s is needed for keeping light condition stable, which gives users more convenience and flexibility.
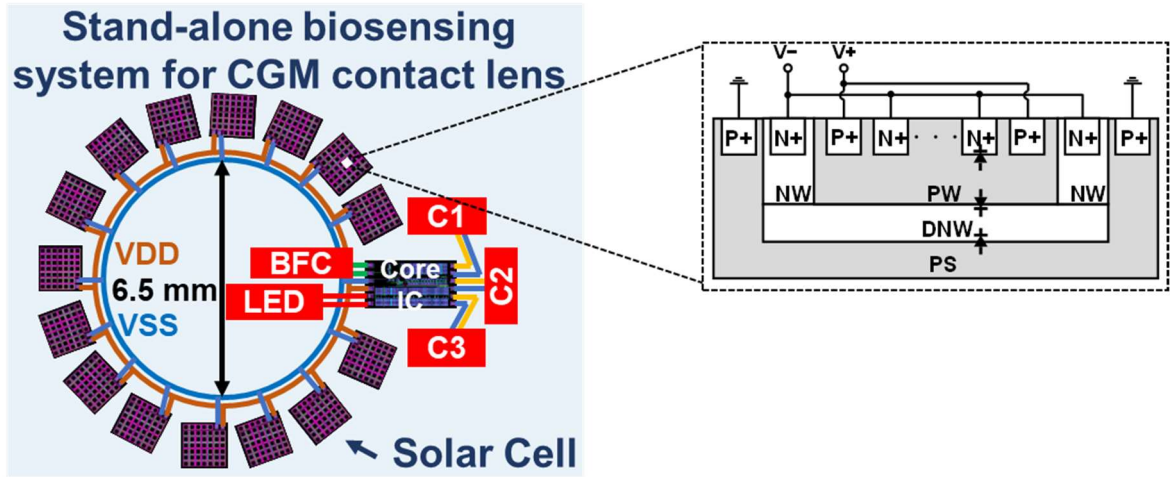
Figure 4.2: Conceptual image of solar cell-powered BFC-input CGM contact lens with LED driving capability.

In this paper, we extend our paradigm of SC-powered BFC-input CGM LSI system to another application scenario, which is specifically designed for emergency cases targeting type 1 diabetes. We present the first CGM contact lens with both localized energy generation and information display. Pulse interval modulation (PIM) and pulse density modulation (PDM) is employed in a hybrid manner with an identical mask layout to manage the tradeoff among power consumption, information visibility, and developing cost. The prototype successfully demonstrates the feasibility of a stand-alone RF-less CGM system. The design details of the proposed CGM LSI system are explained in Section 4.2. Measurement results are described in Section 4.3. The conclusions are given in Section 4.4.

4.2 RF-Less SC-Powered BFC-Input CGM LSI System

To make a fully-stand alone RF-less system, the conceptual image of the CGM contact lens is illustrated in Figure 4.2, which includes the SC, BFC, LED, core IC, connecting wires, and storage capacitors. To avoid a block of eye vision, each component except the LED is arranged away from the eye's visual axis. Same to the principle of a Cassegrain telescope, the near-center LED will not affect users' vision. The solar cell group in Chapter III is employed in this conceptual image due to the power budget. According to our simulation, the

power consumption of the total system is around 100 nW. To prepare a margin for fluctuating power, 15 solar cells can satisfy our scenario while operating the CGM contact lens. The solar cell group can provide 150 nW at sub-0.4 V in 1600-lx light, which is a typical value for an office-room light environment.

Figure 4.3 shows the block diagram of the proposed system, including signal modulation, LED driving, and LED switching. For guaranteeing functional verification, matured circuit techniques have been employed. The circuit schematic of on-lens CMOS SC is shown at the right of Figure 4.2, which is the same as the SCs in Chapter III. Three types of PN junctions, i.e., P-well(PW)/N+, PW/deep-N-well (DNW), and P substrate (PS)/DNW, are available as photodiodes in the standard triple-well CMOS process. In this design, two types of PN junctions, i.e., PW/DNW and N+/PW, are paralleled to achieve high efficiency. The difference between V+ and V– is the supply voltage (V_{SC}). The core IC is powered by the SCs.
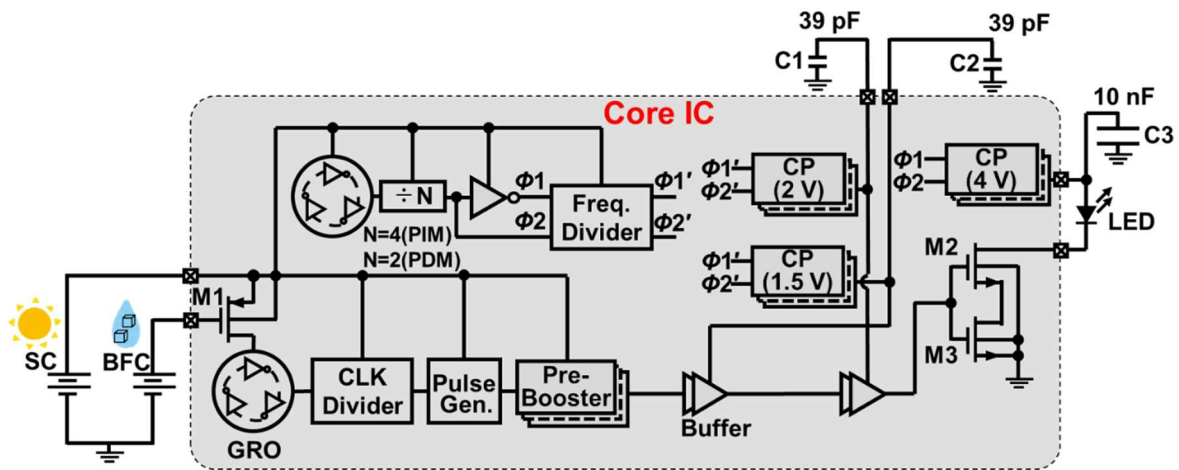
Figure 4.3: Block diagram of the proposed SC-powered BFC-input CGM system.
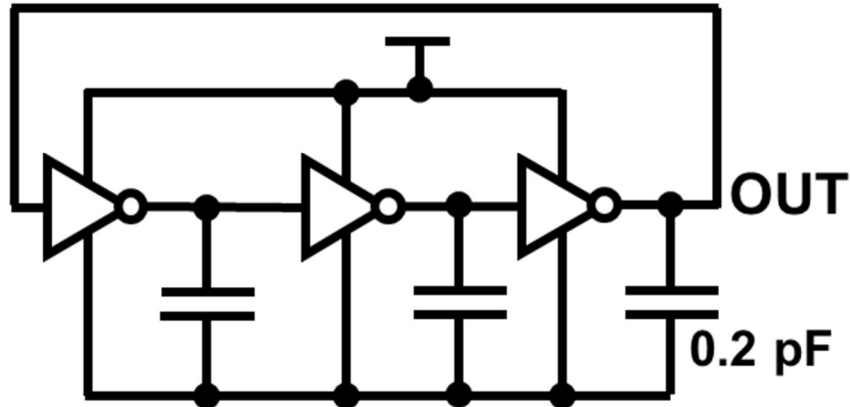
Figure 4.4: Gate-level schematic of the GRO for CLK divider.

4.2.1 Signal Modulation

The non-potentiostat analog-less BFC-input approach contributes to implementation in digital-friendly advanced technology which is beneficial for combining ML. This design separates the sensing component from powering circuits, which reduces the power budget of SCs. Customized 0.6 mm × 0.6 mm BFC which exhibits an open-circuit voltage of 228 mV is developed with a CMOS-compatible process [34]. This kind of BFC has a varying open-circuit voltage (V_{OC}) which is proportional to the glucose concentrations. The single PMOS transistor, M1, works as a sensing transducer to convert the BFC output voltage into the operating frequency of the gated ring oscillator (GRO) whose schematic is in Figure 4.4. The three-stage ring oscillator operates as a timer to output a frequency that correlates to the BFC voltage. Once the supply voltage from SC is applied and M1 is switched on by the BFC voltage, the ring oscillator starts to oscillate without an input signal. The output of the last inverter stage is feedback to the input of the first inverter stage, so the ring oscillator is inherently an unstable system that can oscillate by itself. The output of the GRO is used to control the timing of LED lighting.

As shown in the conceptual operational waveform in Figure 4.5, as BFC output voltage decreases when the glucose level drops, the drain current of M1 increases as well as the operating frequency of the GRO which is 100s of Hz. The GRO output is duty-cycled by a

clock (CLK) divider whose circuit schematic is shown by respective two modes in Figure 4.6. The multiple delay flip-flops (DFF) are cascaded to output pulses within several seconds at an average interval of several minutes, which is sufficient as CGM. A pulse generator (PG), whose schematic is in Figure 4.7 shortens the width of each pulse to 4 μs for LED blinking light emission with a larger margin compared to reference [20], which is distinguishable by the naked human eye.

However, the frequency of the GRO can be easily affected by unstable solar power when the users are moving outdoors and indoors. In the PIM mode, the users need to wait for two lighting pulses for one readout. The time between two pulses may exceed 100 s which is hard to recognize without an accurate timer. Any fluctuation in solar power will increase or decrease the time between two pulses. If the pulse width is shortened to a sub-second level and burst consecutive pulses in a short time, the users don't need to wait a long time and just stay in a stable light environment for a while. Not only by two pulses, but multiple pulses can also attract attention quickly from the users' eyes and don't affect results too much even if one light pulse is missed. Therefore, we proposed a PDM mode as shown in Figure 4.5 to generate 7 more pulses in a row as opposed to a single pulse with PIM at the cost of a higher power, so that the users can distinguish the glucose level by the density of the LED lighting pulses within several seconds. The modification is applied to the CLK divider by adding three more DFFs after the first DFF and reducing three DFFs in the follow-up DFFs. The follow-up DFFs modulate the interval to satisfy the typical CGM specification of every-minute displaying. Since the total DFF counts are kept the same in both modes, PDM mode includes a similar pulse interval mechanism as PIM mode in a hybrid manner.
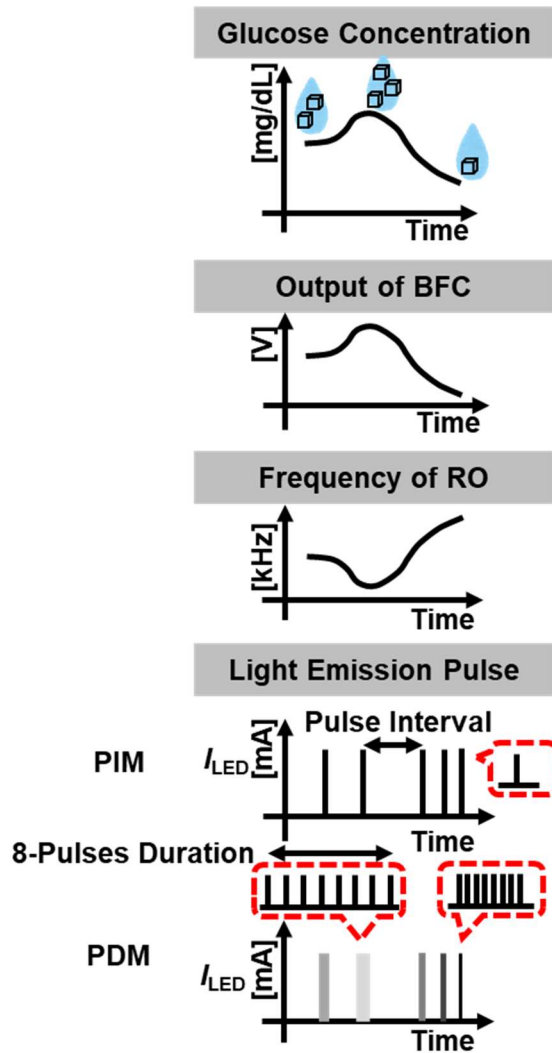
Figure 4.5: Conceptual diagram of LED light emission pulse in PIM/PDM mode.
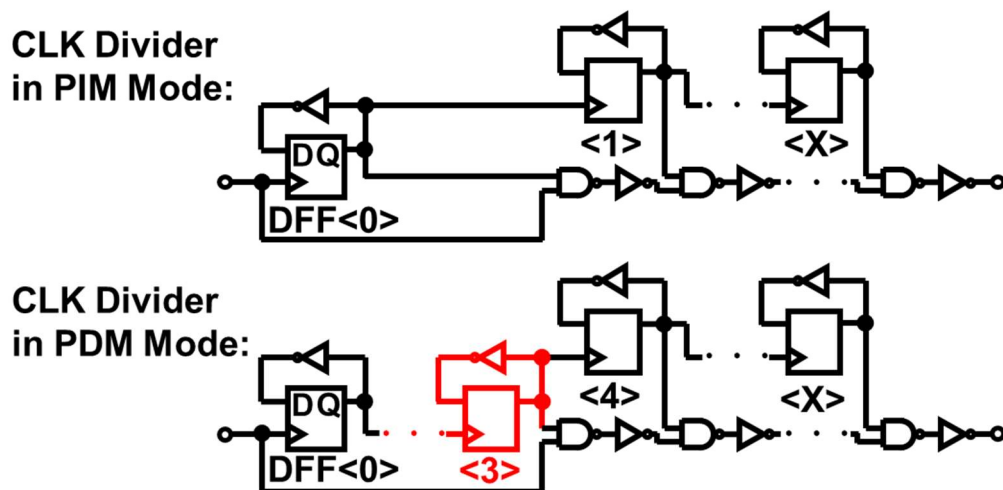
Figure 4.6: Gate-level schematic of the CLK dividers in PIM and PDM mode, respectively.

Pulse Generator :
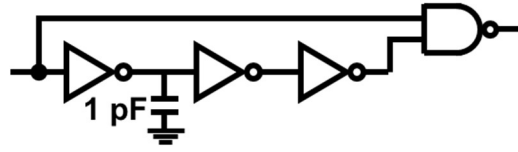
Figure 4.7: Gate-level schematic of the pulse generator.
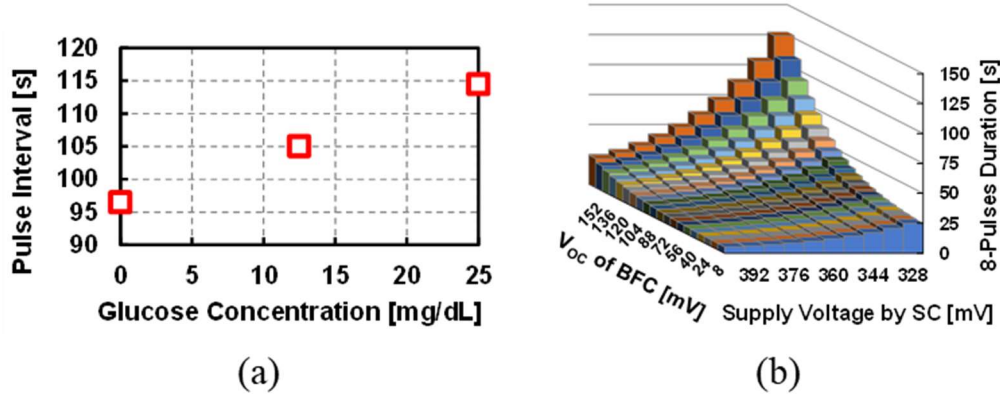
Figure 4.8: (a) Simulated light emission pulse interval vs. glucose concentration, (b) simulated light emission 8-pulses duration vs. V_{OC} of BFC and supply voltage by SC.

As illustrated in Figure 4.5, an interval-modulated single pulse at PIM mode to light the LED is generated with a frequency corresponding to the glucose level. According to the 10-concatenated-BFC output [34] with a 165-mV offset, the interval of the pulse in PIM mode correlates with the glucose concentration, whose simulation results are in Figure 4.8 (a), which is confirmed by the SPICE simulation using Spectre RF.

Figure 4.8 (b) shows the 8-pulses duration corresponding to the V_{OC} of BFC and supply voltage by SC, which is confirmed by the post-layout simulation. When BFC output is low, which means low glucose level, the duration is short and pulse density is high, the frequent LED lighting gives an alert of hypoglycemia. It's worth mentioning that both SC and BFC can affect the current through the GRO. There are some possible methods to reduce supply sensitivity, like adding a native NMOS header between VDD and the GRO [64]. However, it will occupy a voltage headroom, which is not suitable for near-threshold operation by solar cells. Therefore, the system requires a stable light environment such as a bright office room to offer a relatively stable solar cell output.
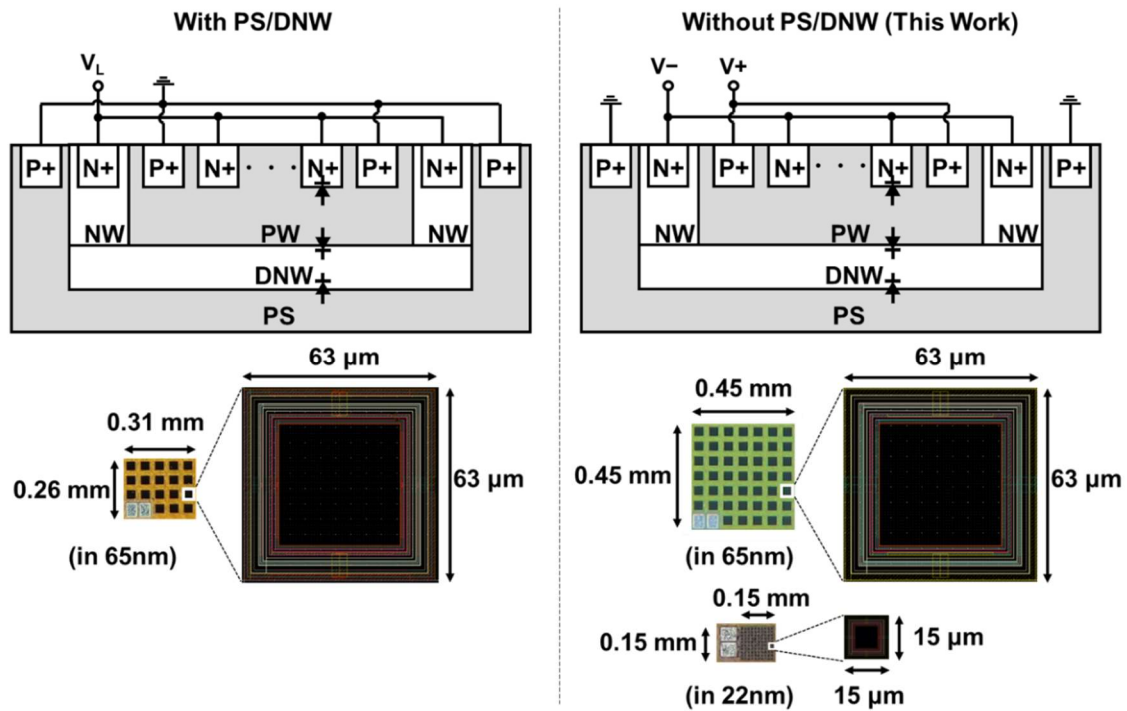
Figure 4.9: The cross-section conceptual diagrams, chip micrographs, and layouts of solar cells using a CMOS process with DNW.

This feature is the same as the V_{TX} in Chapter III and the situation here may be worse because the GRO works in the near-threshold region. Therefore, the varying light could be a fatal issue for accurate glucose readout. Besides staying in a stable light environment, a more advanced and smart solution is expected in the future to keep the supply voltage of GRO stable. One possible way is to use maximum power point tracking, and a dedicated source for GRO with a voltage regulator to keep the power supply of GRO at a relatively stable level.

4.2.2 LED Driving

Figure 4.9 shows the details of the SC implementation. Three types of PN junctions, i.e., P-well(PW)/N+, PW/deep-N-well (DNW), and P substrate (PS)/DNW, can be used as photodiodes in the standard triple-well CMOS process. As a counterpart of solar cells with PS/DNW photodiodes, this work adopts the wire connection in Chapter III to attain a higher open-circuit voltage because high voltage output is of high priority in this work. In order to improve power density from the constrained area, this work implemented two patterns of solar cells with different processes and pitches.

61
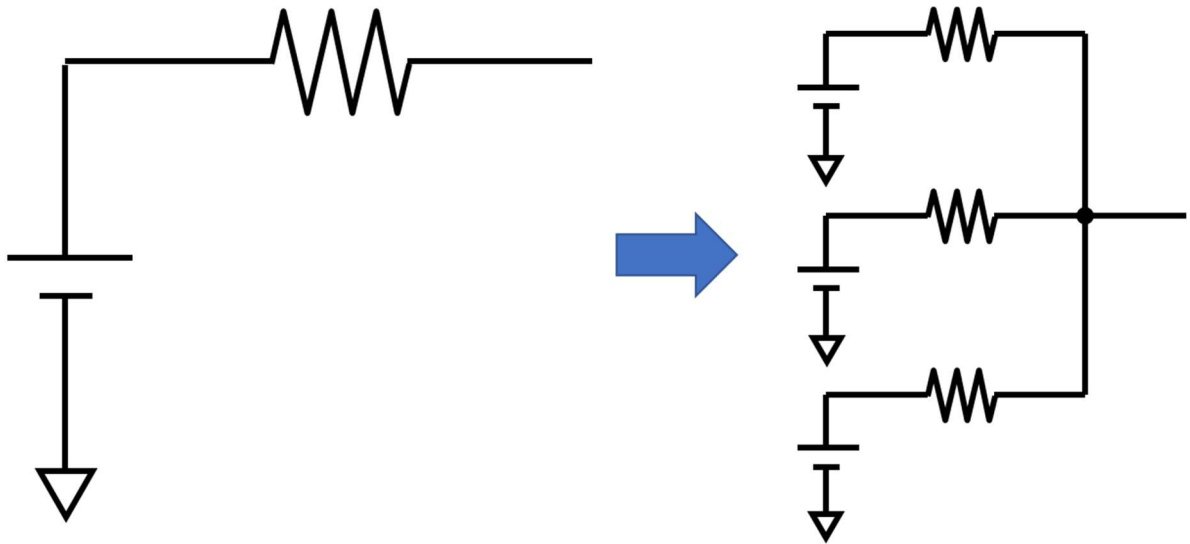
Figure 4.10: Parallel connection of broken down SC pieces to reduce the internal resistance.

Every SC unit can be simplified as a voltage source with an internal resistance as in Figure 4.10. If SC is implemented with smaller pitches, it can be regarded as small SC pieces are broken down from a big SC. If all small SC pieces are connected in parallel, the equivalent internal resistance of the SCs will be small. In addition, the SC with a smaller pitch can improve the fill factor, thus offering a higher power density. Note that the SC with a smaller pitch is implemented in a 22 nm CMOS process.

To drive an LED, charge pumps, 39 pF off-chip energy storage capacitors (GRM0335C1H390JA01D: C1, C2), and a 10 nF off-chip energy storage capacitor (CC201KRX5R7BB103: C3) are employed. Although the off-chip capacitor may make users' eyes uncomfortable, it is required for energy storage for consecutive LED blinking. The capacitance is determined by considering the light-emitting capability, charge pump drive capability, and limited form factor. Even though off-chip components are implemented, the form factor is acceptable due to its thickness of as thin as 0.3 mm for medical-purpose lenses as well as the existing lenses for intraocular pressure monitoring (Triggerfish) [26]. Compared with state-of-the-art smart contact lens designs with an LED display [27], the components in our design are less and smaller, thus resulting in less impact of stress from the contact lens on the active circuitry.
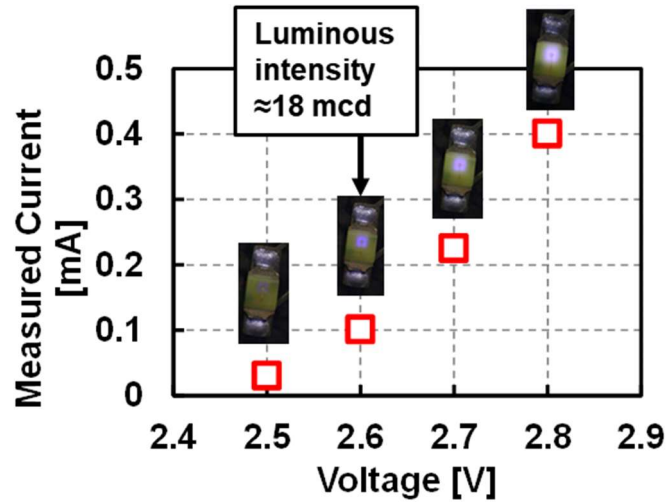
Figure 4.11: The light emission performance of an off-the-shelf LED.
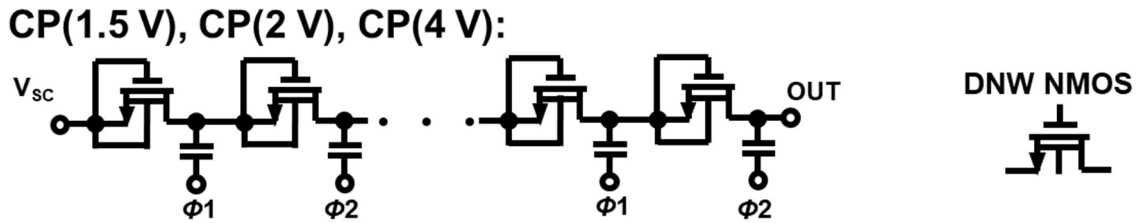
Figure 4.12: Transistor-level schematic of the charge pumps.

To maintain cost-effectiveness, a commonly-available off-the-shelf yet relatively large white LED (SCMP13WBC8W1) is employed, whose power consumption is the lowest in its series. The consumed current is shown in Figure 4.11. It can be observed that the minimum operable voltage of the LED is 2.6 V to emit visible light, which is approximately 18 mcd.

A two-phase clock-driven Dickson charge pump using deep N-well NMOS transistors in all 18 stages, denoted by CP(4V), up-converts the output voltage above 4 V, whose circuit schematic is shown in Figure 4.12. The up-converted voltage guarantees that the stored energy in the 10-nF capacitor is sufficient for consequent LED blinking light emission. The clock of the charge pumps is generated by another GRO which has a much higher operating frequency, which is 60 kHz, than the GRO current-starved by M1, ensuring a fine-grained voltage output of the charge pumps with less ripple. Compared with the prior art of DC-DC converter using an off-chip capacitor [65], the proposed CP(4V) can achieve a higher Figure of Merit (FoM) as shown in Figure 4.13 but sacrificing peak efficiency.

$$FoM = (\Delta V_{OUT,MAX} * F_{CLK} * Area * C_{OUT} / I_{LOAD,MAX})^{-1}$$
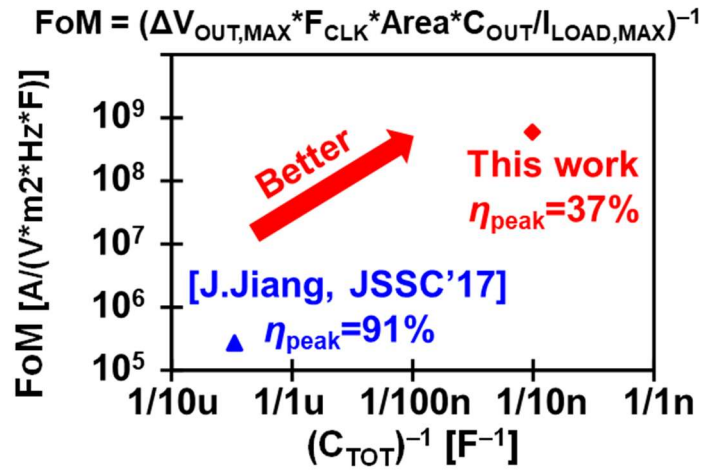
Figure 4.13: FoM of the DC-DC converter.

The Dickson-topology-based CMOS-switched charge pumps are considered because they can offer a high conversion ratio with moderate efficiency. Besides, it has advantages, such as area efficiency and low complexity, compared with inductor-based charge pumps and bootstrap charge pumps. However, it consumes a large amount of power during the start-up process. Therefore, the system is forced to adopt an always-on energy harvester to avoid frequent start and shut-down of the charge pump. This feature is different from the energy harvesters in the last two chapters since they triggered the harvesting by the on-chip timer. The reason is that the start-up process in wireless biosensors is not as time-consuming as LED driving. The output voltage of the energy harvesters is only half of that in this chapter so they can afford a frequent start and stop.

The conceptual operating waveform is illustrated in Figure 4.14. After one LED lighting pulse, the charge in capacitors is dissipated, then recharged. According to the post-layout simulation, although there is a voltage drop of 86 mV on CP(4V) output, the minimum operating current of the LED can be kept above 1.4 mA, higher than the visibility limit which corresponds to 2.6 V as shown in the simulated results with LED SPICE model in Figure 4.15. It's a challenge for consequent 8 lighting pulses if the charge dissipates too fast. Therefore, in PDM mode, the clock frequency of the main charge pump is doubled. So that the voltage can recover faster, and gets ready for the next lighting. However, higher clock frequency leads to higher power consumption. It is a trade-off between PIM and PDM mode.

64
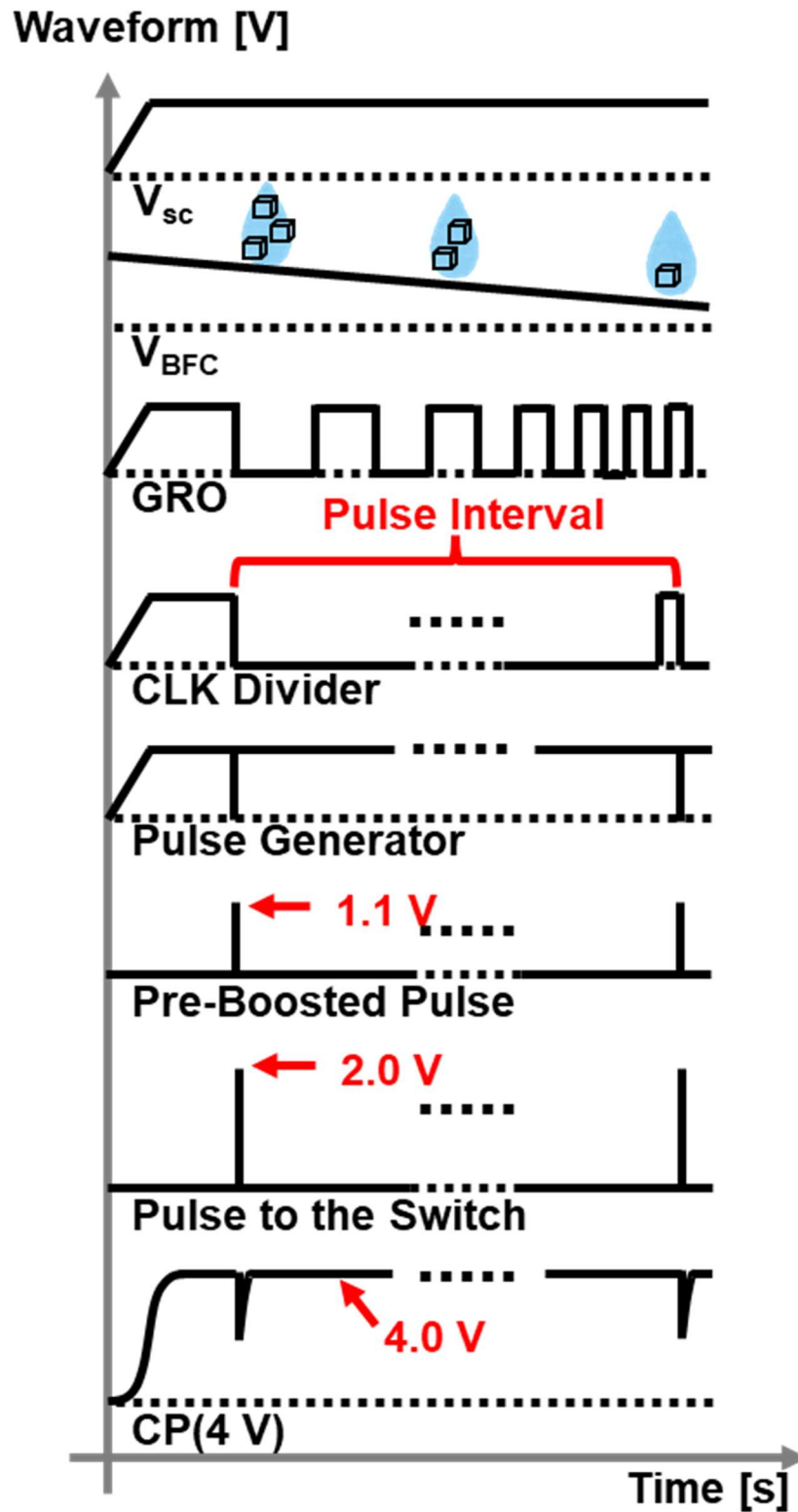
Figure 4.14: Conceptual diagram of transient operational waveforms.

However, it consumes a large amount of power during the start-up process. Therefore, the system is forced to adopt an always-on energy harvester to avoid frequent start and shut-down of the charge pump. The conceptual operating waveform is illustrated in Figure 4.13. After one LED lighting pulse, the charge in capacitors is dissipated, then recharged. According to the post-layout simulation, although there is a voltage drop of 86 mV on CP(4V) output, the minimum operating current of the LED can be kept above 1.4 mA, higher than the visibility limit which corresponds to 2.6 V as shown in the simulated results with LED SPICE model in Figure 4.14. It's a challenge for consequent 8 lighting pulses if the charge dissipates too fast. Therefore, in PDM mode, the clock frequency of the main charge pump is doubled. So that the voltage can recover faster, and gets ready for the next lighting. However, higher clock frequency leads to higher power consumption. It is a trade-off between PIM and PDM mode.
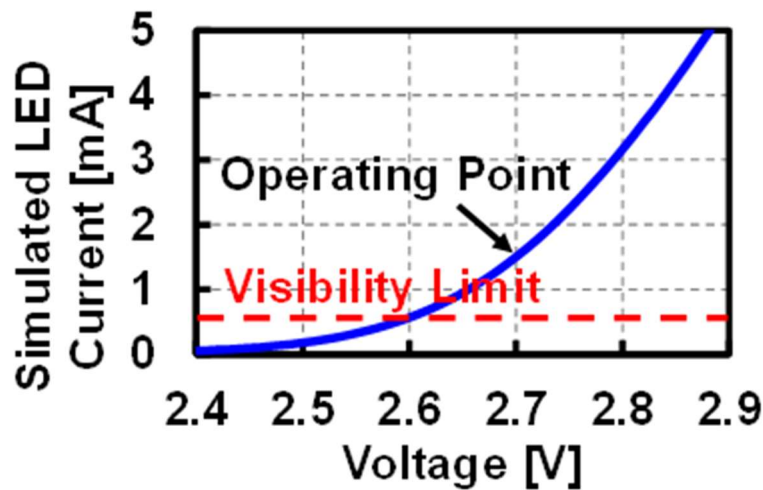
Figure 4.15: Simulated operating current of the LED vs. the voltage across the LED.

Frequency Divider:
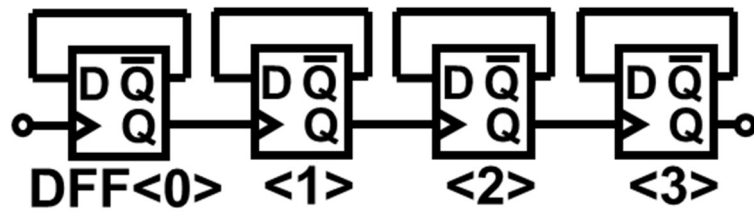
Figure 4.16: Gate-level schematic of the frequency divider for the charge pump clock.

Pre-booster:
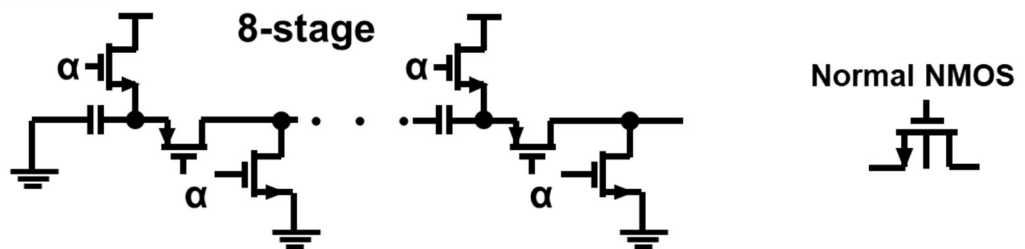
Figure 4.17: Transistor-level schematic of the pre-booster.

4.2.3 LED Switching

The Dickson charge pump schematic was applied to the CP(2V) and the CP(1.5V), which have 26 and 6 stages, respectively. The two charge pumps supply the respective voltage of the two-stage inverter-based buffers with 39 pF off-chip energy storage capacitors (C1, C2) which are used to drive the gate of stacked NMOS switches (M2, M3). These two capacitors can be replaced by MIM capacitors with an area overhead of 0.045 mm^2 or MOM capacitors adopting the upper layers at the top of logic circuits to avoid area overhead. In addition, the clock frequency for CP(2V) and CP(1.5V) is 4× down-converted through a frequency divider, as shown in Figure 4.16, to reduce the power consumption of the charge pumps.

The 8-stage pre-booster, using boosting multipliers in reference [66], connected to the pulse generator boosts the pulse voltage from 0.4 V to 1.1 V, whose schematic is shown in Figure 4.17. Finally, the pulse is up-converted to 2 V through the buffers to drive the NMOS switches. The gate driver ensures that the current through the LED is high enough to make

67

emitted light visible. Other designs use level shifters [14], [20], [44], or voltage regulators [11], [56] to down-convert voltage levels from the main voltage source. However, both methods will load the main charge pump, CP(4V), leading to a poor output voltage and insufficient charge storage in the capacitor. According to the simulation by loading CP(4V) with a level shift in reference [62], the output of CP(4V) degrades to 2 V, which is infeasible to drive the LED. As a key enabler of LED driving capability, CP(4V) only supplies the LED and the capacitor. Therefore, the task of driving the buffers is allocated to CP(1.5V) and CP(2V). A more complete system for future improvement should include Maximum Power Point Tracking to make the energy harvester operate at high efficiency.

4.3 Measurement Results

The core IC was implemented in standard 65-nm CMOS technology. Two patterns of solar cells were implemented in a 65 nm CMOS LP process and a 22 nm CMOS ULL process, respectively. The 65-nm CMOS solar cells were employed in the prototypes. The die micrograph and the CGM system are shown in Figure 4.18. BFC, core IC, and SC are implemented with independent chips because it's more convenient to assemble small pieces of components on a curved surface of a contact lens. Considering the typical radius of curvature of a contact lens is 8.4–8.6 mm and the center thickness is 0.2–0.4 mm, each component with the sub-mm^2 size is easy to accommodate. Another merit of separated small chips is easy maintenance when one component is broken or the chip design is changed. The situation is similar to that in Chapter III.

The proposed system takes 11.4 mm × 8.9 mm, which is comparable to the state-of-the-art smart contact lenses [16], [20], whose diameters of the coils are 10 mm and 11.5 mm, respectively. This system can be integrated into contact lenses with a typical diameter of 14–16 mm. Each component except the LED is arranged 3.25 mm away from the eye's central visual axis to avoid vision blocking since the pupil has a typical diameter of 6 mm. The two modulation modes are implemented in two prototypes respectively. Since the only difference

is the CLK divider, which occupies a small area ("Others" in Figure 4.18), the two prototypes have a similar appearance. Additionally, these two modes can be easily switched by a post-fabrication process such as FIB. In addition, the active circuitry is fully covered by epoxy resin for encapsulation, as same as reference [14] which has been confirmed for a 2-week usage duration in our previous work. Usually, a 2-week duration is enough for typical CGM contact lenses.

Figure 4.19 shows the performance of the SC units. According to the measured I–V characteristics in the illumination intensity range of 200–2000 lx, the SC of this work can supply a higher V_{OC} than the SC with PS/DNW photodiodes. Figure 4.19 (b) compares the performance with other on-chip solar cells [46], [67]–[69]. By the same principle of solar cells in reference [67] using a small pitch, the SC of this work in 22 nm achieves the highest power density around 900-lx light intensity and 3× peak power density at 2000-lx light intensity because of the high fill factor and low internal resistance. By assembling 15 SC chips in 65-nm CMOS on the lens, the total available power is sufficient for the operation of the proposed CGM system at 800–1600 lx which is the typical illumination intensity range in a bright office room.
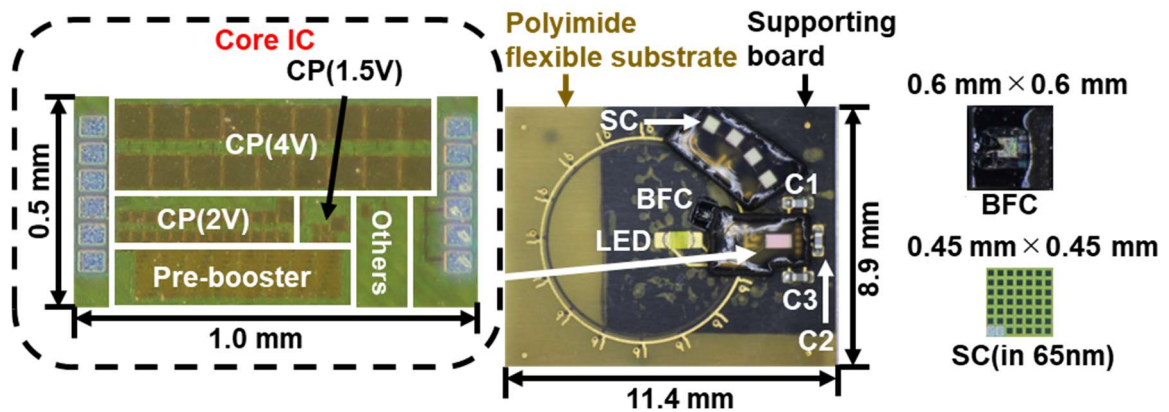
Figure 4.18: Micrograph of core IC, BFC, SC, and prototype of the proposed CGM system.
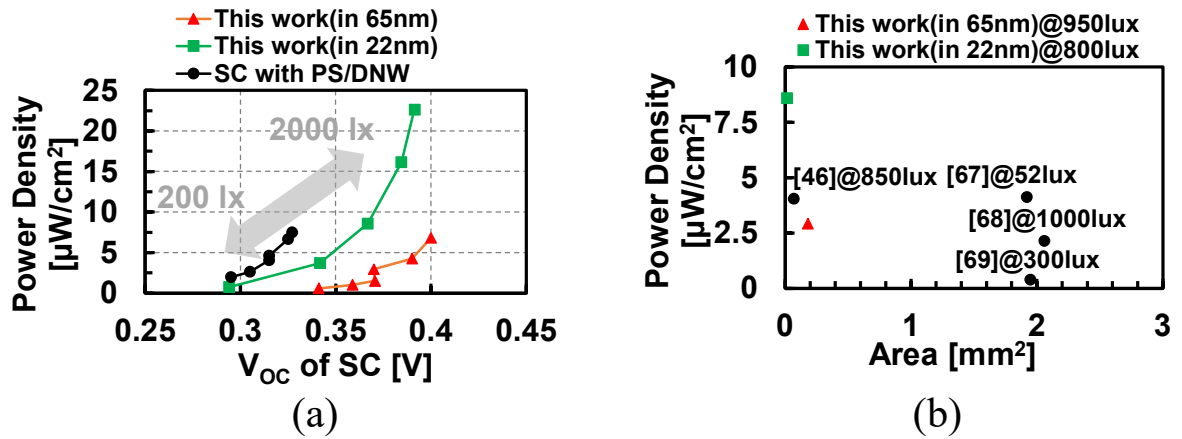
Figure 4.19: (a) Measured results of open-circuit voltage and power density of SC units vs. light intensity (200–2000 lx), (b) performance comparison with other on-chip solar cells.
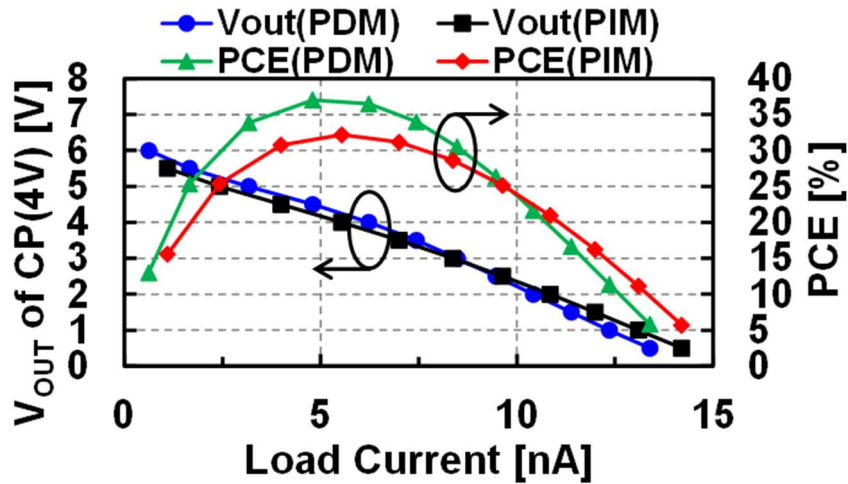
Figure 4.20: Measured performance of CP(4V) without off-chip C3(10 nF) at 0.39-V supply.

Figure 4.20 shows the performance of CP(4V) without off-chip C3(10 nF) at 0.39-V supply. The power conversion efficiency (PCE) and output voltage (V_{OUT}) are almost the same in PDM and PIM modes because of the same flying capacitor in the last stage. The higher switching frequency of PDM mode brings a slight improvement in PCE and V_{OUT} at 4 V, which is the operating point. Although the system is free-running without a voltage regulator, the energy harvester works near the maximum power point, because the load is almost capacitive only.
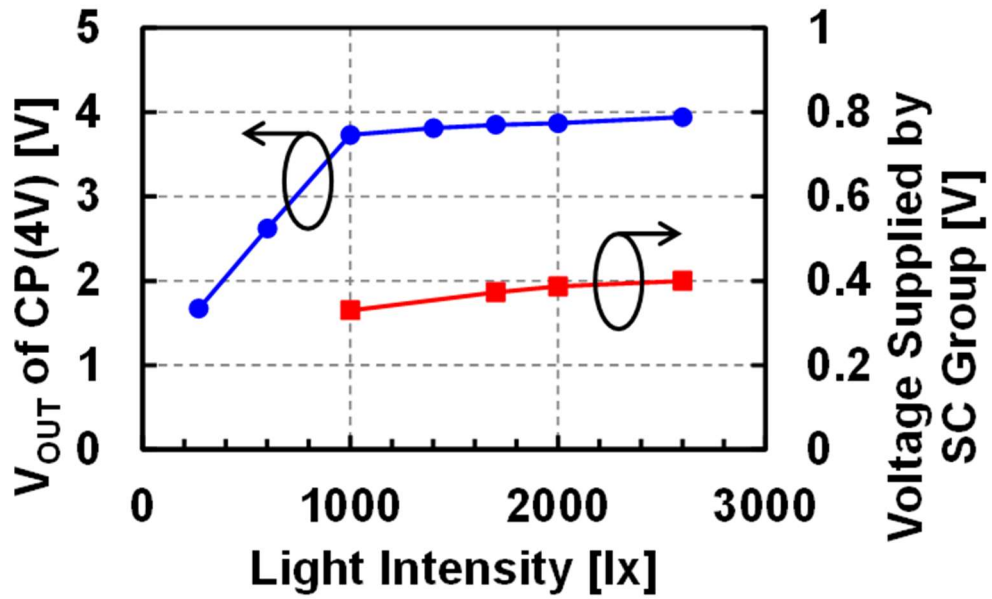
Figure 4.21: Measured performance of the prototype in different light conditions with 4 series-connected solar cells.

Figure 4.21 shows the performance of the prototype across varying light conditions. With only 4 series-connected solar cells, the system requires a certain light intensity above 1000 lx to maintain the voltage to drive the LED. It should be noted that due to the high cost of dicing solar cells, we only test with the prototype integrated with 4 series-connected solar cells to save samples. According to the measurement results, even with only 4 solar cells, the up-converted voltage for LED driving can attain the predetermined level across varying light conditions. If equipped with more solar cells, the performance of the energy harvester can be improved, so as to be able to operate in a dim environment whose light intensity is below 1000 lx.

Figure 4.22 shows the measured power consumption at a 0.39 V power supply under PDM mode. We can observe that there were three spikes, which suggests that the LED was lighting at the time. The time interval between the spikes is 95.3 s when the BFC output is 0 V, which complies with the simulated results in Figure 4.8 (a). The random power-down noise may occur resulting in a delayed time interval of 98.4 s. The light emission time with 8 lighting pulses lasted 5 s, which basically agrees with the simulated results in Figure 4.8 (b). 5-s duration is reasonable for the users to react during hypoglycemia conditions.
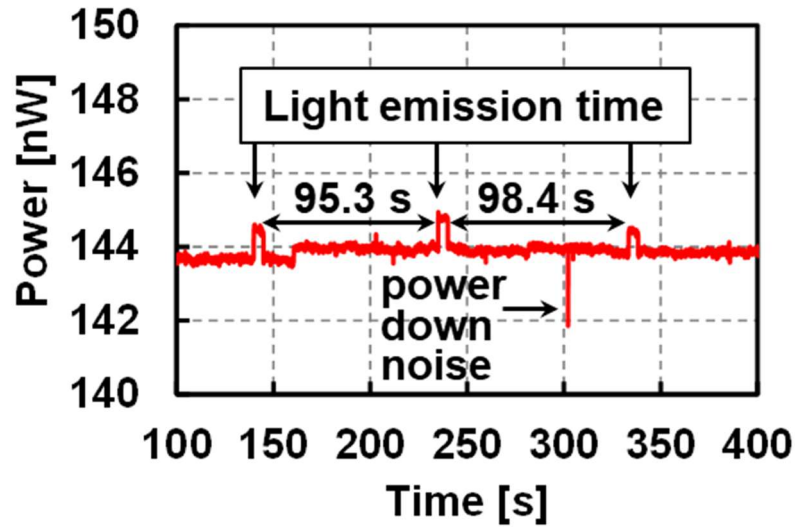
Figure 4.22: Measured power consumption at a 0.39 V power supply under PDM mode.
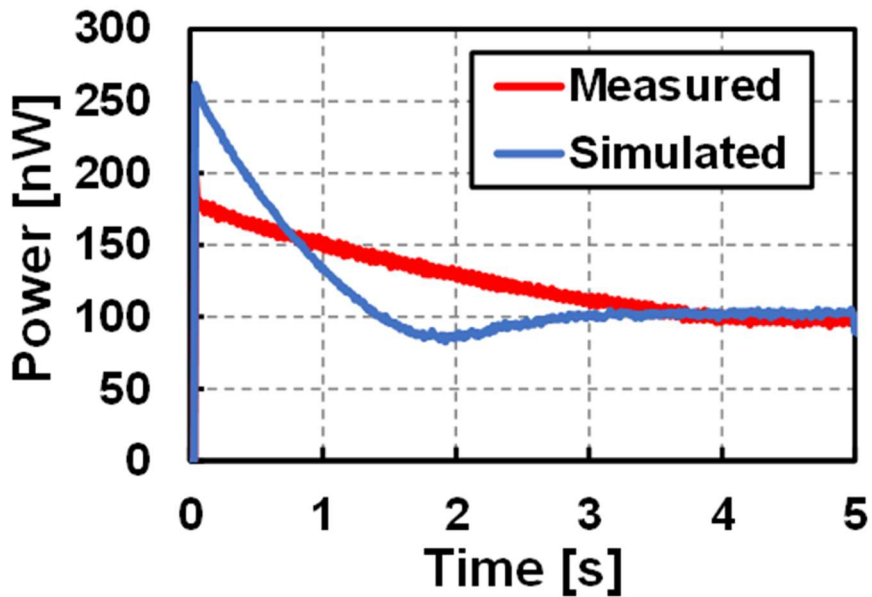
Figure 4.23: Cold start-up process at a 0.39 V power supply under PIM mode.

Figure 4.23 shows the cold start-up process at 0.39 V in PIM mode which takes approximately 4 s to charge a 10-nF energy storage capacitor to a standby state. Therefore, the power was sloping during the charging phase. The power consumption in the start-up process exceeds the power budget for a certain amount. To solve this issue, the start-up process can be completed under strong light before wearing the contact lens. After the start-up process, the power consumption most time is within the power budget since the biosensing system is at a stand-by state most of the time which doesn't require a re-start.
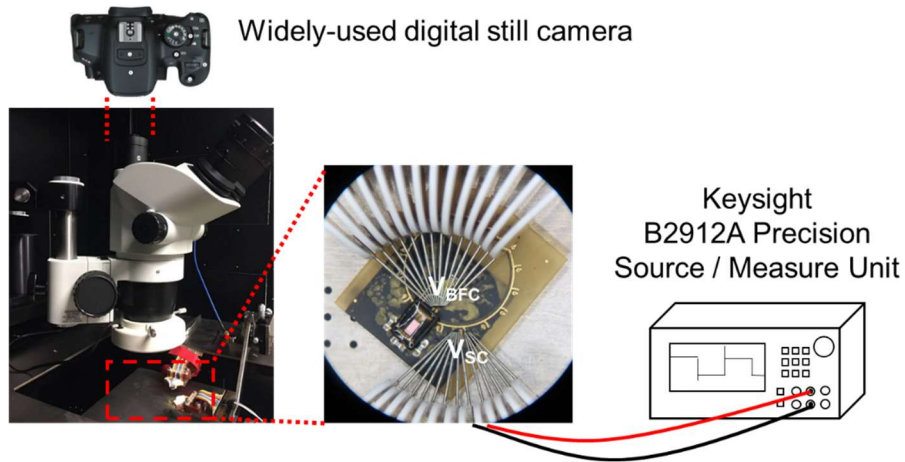
Figure 4.24: Measurement setup for observing the LED light.
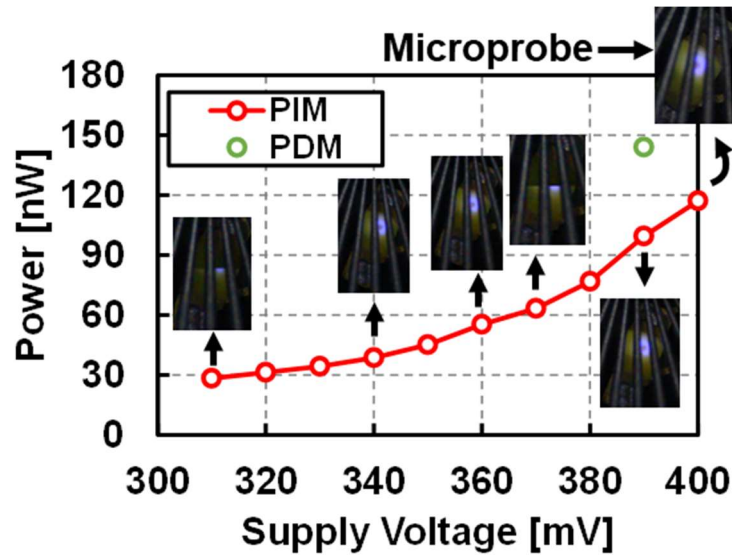
Figure 4.25: Measured standby power consumption and light emission vs. supply. voltage.

Figure 4.24 shows the measurement setup for observing the emitted light by the LED. Figure 4.25 shows the measured standby power consumption as a function of the supply voltage under two modes. Through observation by a digital camera (Kiss X6i), light emission from LEDs has been successfully confirmed in the range of 28–117 nW at 0.31–0.4 V in PIM mode. For different supply voltages, the stored energy in capacitors changes. Hence, the light intensity of the LED at power off decreases with the decrease in the supply voltage. Even the weakest light intensity is approximately higher than 14 milli-candela, which is enough for practical application [70].
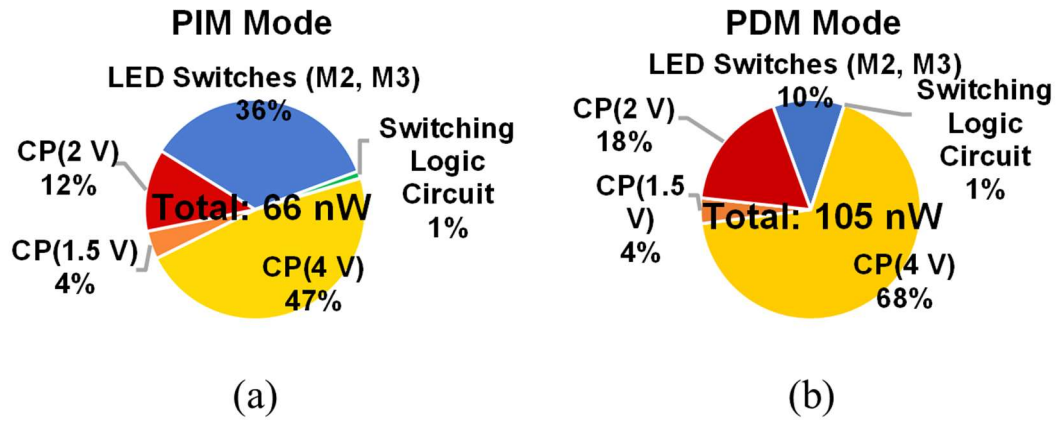
Figure 4.26: Simulated power breakdown in PIM and PDM modes, respectively.

It can be observed that the total power consumption can be dynamic in the range of 28–144 nW as supply voltage varies. To cover the maximum power, 15 on-lens SCs are necessary because we assume that each SC unit can provide 10 nW in a 1600-lx light environment.

Figure 4.26 shows the simulated power breakdown in PIM/PDM modes at 0.39-V supply. The charge pumps and the LED driving circuits dominate the power consumption, while the switching logic circuit consumes sub-nW. It should be noted that compared with a customized micro-LED in the state-of-the-art previous works [20], the power consumption of the LED in this work is higher. In future works, efforts can be put into customized LED design to reduce power consumption and required SC area further.

Table 4.1 depicts the performance compared to previous state-of-the-art CGM contact lenses[11], [14], [56]. Since our technique does not require external devices such as RFID reader/writer, and wireless receivers, it can reduce total power dramatically. This work demonstrates the possibility of the emergence of fully stand-alone RF-less CGM contact lenses which are environment-friendly because they do not use lossy wireless power transfer or battery.

Table 4.1: Comparison with Previous State-of-the-art CGM Contact Lenses.

	ISSCC'11 [11]	BioCAS'18 [14]	VLSI'19 [56]	This work
Communication	RFID	Wireless TX	RFID + Wireless TX	**LED display**
Supply Voltage [V]	1.2 (regulated)	0.165–0.39	2.0 (regulated)	0.31–0.4 (PIM) 0.39 (PDM)
Energy and Sensing Source	RF-powered + Potentiostat	BFC-powered + BFC-input	RF&battery-powered + Potentiostat	**Solar cell-powered + BFC-input**
Modulation Scheme	FM-LSK	Supply-modulated OOK	LSK + OOK	PIM/PDM
Power (Chip Only)	3 μW	0.27–11.8 nW	143–490 nW	28–117 nW (PIM) 144 nW (PDM)
Off-Chip Capacitor	N/A	N/A	1 (RF mode)	1×10 nF 2×39 pF
External Device	RFID Reader/Writer	Data Receiver	RFID Reader/Writer	**Fully stand-alone**
Readout Distance	15 cm	10 cm	1 cm (LSK), 1 m (TX)	**Display on lens**
Process	0.13 μm	65 nm	0.18 μm	65 nm
Chip Area [mm^2]	0.5	0.15	2.25	0.5
Glucose Level [mg/dL]	0–36	180–540	3–25	0–25

4.4 Conclusions

To make CGM contact lenses usable by people with type 1 diabetes who may suffer from serious symptoms of hypoglycemia, this work presents an SC-powered BFC-input biosensing system for next-generation CGM contact lenses. It demonstrates the possibility of the emergence of stand-alone RF-less CGM contact lenses which are environment-friendly and human-friendly because it does not use lossy wireless power transfer or battery. The RF-less battery-less biosensing system shows the feasibility of providing users with a non-invasive method to prevent hypoglycemia conditions with many conveniences by displaying glucose level information through the on-lens LED. By prototyping IC in 65-nm CMOS, the measured power of 28 nW/144 nW at PIM/PDM mode with a 0.31 V/0.39 V supply voltage and the LED light emission have been confirmed, enabling a fully stand-alone operation under office-room ambient light. The SC group with only a 3-mm^2 area makes the CGM contact lenses able to operate under indoor ambient-light environments without any external devices for power transfer or data receiving, achieving a self-powered smart contact lens with a long lifetime.

CHAPTER V

Conclusions and Future Directions

5.1 Summary of Conclusions and Contributions

This dissertation focuses on developing next-generation smart contact lenses for CGM applications. As CMOS techniques evolve generation by generation, LSI systems are becoming more versatile, miniaturized, energy-efficient, and across-multi-discipline, making our society smarter than ever before. Smart contact lenses may become the next blue-ocean market, and they are walking from imagination and science fiction to our reality. As a product of interdisciplinary science and engineering, the CGM contact lens has gone through 2 generations since its birth in the 2010s. Although the players come and go, many researchers around the world have been advancing state-of-the-art smart contact lenses and bringing their works closer to practical applications. This dissertation started with Generation 2 CGM contact lenses which can actively communicate with data receivers, and explored a new paradigm of stand-alone CGM contact lenses. It overviewed three solar cell-powered LSI systems toward next-generation CGM contact lenses which are able to actively transmit information and even alert the users of hypoglycemia directly. The target of this dissertation is to demonstrate the feasibility of solar cell-powered CGM contact lenses which can achieve stand-alone operation with fewer external devices. Based on the results of these works, the design trade-offs of CGM contact lenses will be clearer to researchers and engineers.

Chapter II presents a fully-integrated LSI system for CGM contact lenses. The implemented chip in a 65 nm CMOS process contains an energy harvester, supply voltage monitor (SVM), wireless transmitter, and on-chip antenna. Cooperating with BFC generating power from glucose, it's the first attempt at introducing solar energy harvesting to a BFC-combined biosensing system for joint power supply. The major contributions of this work

include 1) a fully-on-chip design of low implementation cost, with a total area of 0.413 mm^2; 2) a new paradigm demonstration that paves the way to a solar cell-powered BFC-input LSI system for stand-alone CGM contact lens; 3) 89% area reduction compared to BFC-powered biosensing system by utilizing solar cell, making the system compatible with a 0.45 mm^2 glucose BFC; 4) 3.4× increased power density of solar cell at the dim light environments (200 lx) by adopting a triple-well CMOS photodiode design which is normally available in CMOS process; 5) low power consumption of 1.58 nW which can be covered by a 0.3 mm^2 on-chip solar cell.

Chapter III proposes a solar cell-powered BFC-input biosensing system for CGM contact lenses with an off-chip antenna for long-distance wireless communication. Constrained by available power density and energy density without a battery, the previous CGM contact lens suffers from short communication distance. The new architecture solves this issue by solar cell-based energy harvesting, cooperating with a 10-nF capacitor and a 3 mm × 4 mm antenna which maximizes the radiation power to extend the communication distance. The major contributions of this work include 1) extension of wireless communication distance between CGM contact lenses and handsets up to 40 cm for the first time for a battery-less system; 2) a novel 2-D modulation combining FSK and PIM to send the voltage information of both solar cell and BFC, which can mitigate the interference from unstable solar power; 3) improvement of voltage monitor from SVM to make it able to operate at lower supply voltage and reduce power consumption.

Chapter IV prototypes a solar cell-powered BFC-input CGM contact lens with an LED for direct hyperglycemia/hypoglycemia warning. To remove RF communication, the adoption of an LED achieves localized information display. Cooperating with localized power generation by solar cells, the system becomes fully stand-alone without any external devices. The major contributions of this work include 1) the first demonstration of a fully stand-alone RF-less CGM contact lens with localized power generation and localized information display; 2) LED driving capability for emergency cases without wireless power

transfer, eliminating the necessity of glasses and data receivers, which is user-friendly for type 1 diabetes; 3) multi-stage buffer drivers to switch on the LED without level shifters or regulators, realizing 4-V voltage up-conversion for efficiency LED light emission; 4) improvement of BFC-input approach to reduce power consumption further; 5) energy harvesting at the light intensity of 800 lx which is a typical indoor ambient-light environment.

5.2 Other Works Related to This Research

Besides SVMs and current-to-frequency converters used in this dissertation, we also designed a slope ADC-like SVM (SASVM) for biofuel-cell-powered supply-sensing systems in 180-nm CMOS. Other than the above three LSI systems for CGM contact lenses, the design of each building block and composition also attract attention. The advancement of building blocks coordinates the overall performance improvement of CGM contact lenses.

In the past years, new designs of analog front end made biosensing systems with a smaller area, lower power consumption, and higher energy efficiency. The analog front end is an interface between the physical world and the digital world. It is always a classic subject in a biosensing system to transduce bio-information to a bit signal. Our proposed SASVM can transduce the supply voltage in the range of 0.18–0.35 V to a 9-bit code. It has better accuracy than the SVM in Chapter II and consumes less power.

The block diagram of the proposed SASVM is shown in Figure 5.1. The main idea is based on the single-oscillator-based temperature sensor technique described in the reference [71]. Compared with conventional single-slope ADC which separates input voltage (V_{IN}) and supply voltage (VDD), the proposed SASVM is designed to be powered by a BFC and sense its voltage. That means the external reference voltage can be eliminated as the SASVM is self-referenced. Another external key element of conventional slope ADC is the clock signal, which determines the conversion time. Usually, the conversion time of the slope ADC is long due to a large bit size to maintain a high resolution. Therefore, slope ADC is suitable for the measurement of signals which are varying slowly, or in cases where high accuracy is required.

Succeeding this feature from slope ADC, SASVM can realize a digitized VDD signal with a high resolution and accuracy.

The reference clock frequency, f_{REF}, of the proposed SVM is implemented using the DLS logic oscillator described in reference [72]. It is designed in DLS logic circuits [73] that can operate at extremely low power consumption at VDD less than 0.3 V. The leakage current can be in the order of 10 fA/gate in 180-nm CMOS [73]. In addition, the ON current of DLS logic gates is weakly dependent on VDD, resulting in a low supply sensitivity of the oscillation frequency.

However, the DLS logic oscillator is with a low frequency. If an accurate bit signal with high resolution is desired, we have to extend the conversion time. If a short conversion time is still needed, we have to sacrifice the bit size of the counter. To solve the conversion time-bit size trade-off, the burst pulse generator is utilized to generate a pulse train, V_{Burst}, from reference clock signal f_{REF} when Enable signal is high. A single input pulse burst to 16 pulses to increase the resolution even keeping the same conversion time.
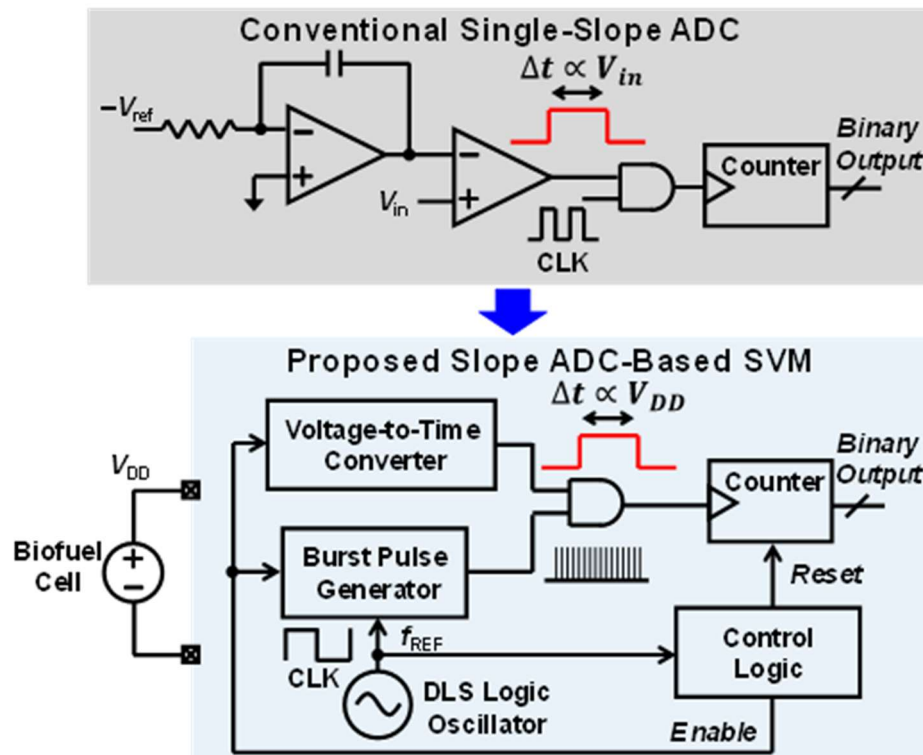
Figure 5.1: Block diagram of the proposed SASVM and its comparison with conventional single-slope ADC.

80
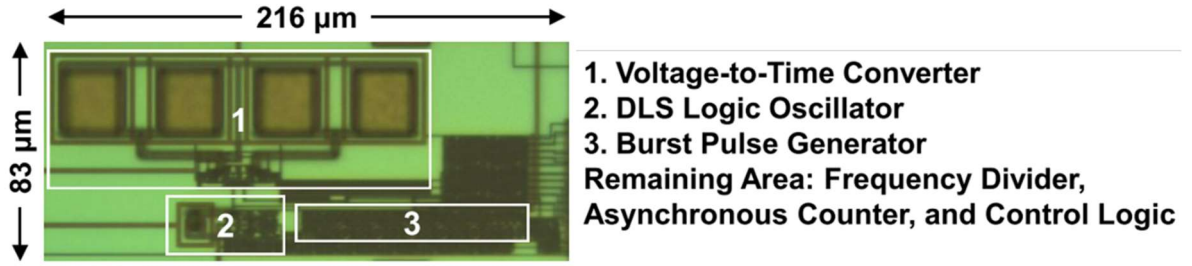
Figure 5.2: Chip micrograph of the proposed SASVM.
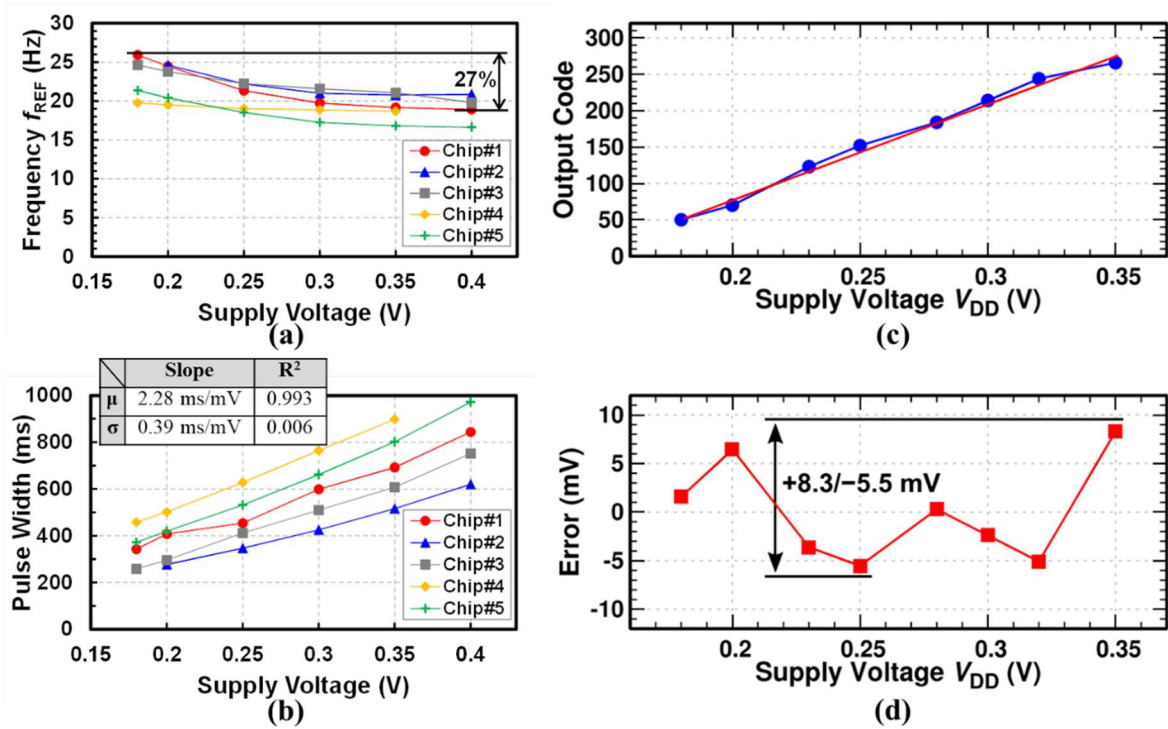
Figure 5.3: Measured results of (a) frequency of the DLS logic oscillator, (b) output pulse width of the proposed voltage-to-time converter, (c) output code, (d) nonlinearity error of the proposed SASVM.

A slope-based voltage-to-time converter (VTC) generates a pulse width proportional to the supply voltage by subtracting two slopes with different slew rates. The output pulse of VTC and burst pulses are logically ANDed. Finally, an asynchronous counter digitizes the counts of burst pulses to a binary output.

The test chip of the proposed SASVM was fabricated in 180-nm CMOS technology to validate its effectiveness. A chip micrograph is shown in Figure 5.2. The proposed SASVM occupies an active area of 0.018 mm^2. As shown in the measured results in Figure 5.3 (a).

The DLS logic oscillator achieves a maximum frequency variation of 27% in a VDD range of 0.18–0.4 V. The least frequency variation among the tested 5-chip samples is only 6%, showing a weak supply dependence. Figure 5.3 (b) shows the measured output pulse width of the proposed voltage-to-time converter with respect to VDD. The proposed converter successfully generates an output pulse width that is linearly proportional to VDD, resulting in a slope coefficient of an average of 2.28 ms/mV in a VDD range of 0.18–0.4 V.

Figure 5.3 (c) shows the measured output code of the proposed SVM. The output code ranges from 50 to 266 in a VDD range of 0.18–0.35 V, which means 9 bits of the counter are employed. By calculating the gap between the measured dots and their fitting straight line by linear regression using a least-squares method in Figure 5.3 (c), the measured nonlinearity error of the proposed SASVM is within −5.5/+8.3 mV, as shown in Figure 5.3 (d). The measured average power consumption of the proposed SASVM ranges from 0.21 nW to 3.9 nW in the VDD range of 0.18–0.35 V. This power level can be supplied by a single sub-mm^2 biofuel cell [34], making it compatible with wearable and implantable sensors. The proposed SASVM consumes 0.29 nJ/bit at a VDD of 0.35 V, which shows better energy per conversion and accuracy compared with previous SVMs [42]. This design provides a new option for analog front ends in CGM contact lenses. This work was initialized by my colleague Dr. Atsuki Kobayashi, and finalized by me. I served as an executor for the system re-design and testing. Data in Figure 5.3 (c) and (d) are measured with the help of Dr. Atsuki Kobayashi.

5.3 Future Directions

This dissertation opens up new paradigms for CGM systems and advances the performance of Generation 2 CGM contact lenses. All proposed three CGM contact lenses are summarized in Table 5.1. The fully on-chip biosensing system in Chapter II requests the least cost due to the small area but sacrifices the sensing and transmission performance. As a counterpart, the CGM contact lens with an LED in Chapter IV improves the sensing and display performance but consumes more power, area, and cost. The CGM contact lens with

an off-chip antenna in Chapter III is a moderate option, compromising between performance and cost. They have covered the design of next-generation CGM contact lenses from many perspectives. However, there are still big challenges and desired new functions in the way to a smart, compact, reliable, and comfortable product that is close to the practical applications.

Table 5.1: Comparison of Proposed CGM Contact Lenses in Three Chapters.

	Chapter II	Chapter III	Chapter IV
Methodology	Wireless TX	Wireless TX	LED display
Process	65 nm	65 nm	65 nm
Supply Voltage for Sensing Front End [V]	0.3−1.0	0.3−0.6	0.3−0.4
Role of BFC	Power source	Biasing	Biasing
Modulation	FSK	FSK+PIM	PIM/PDM
Off-Chip Component	Fully on-chip	Antenna + Cap	LED + Cap × 3
External Device	Receiver	Receiver	Fully stand-alone
Transmission Distance	10 cm	40 cm	Display on lens
Required Area [mm²]	0.413 (chip) 0.45 (BFC)	0.29 (chip) 2.6 (solar cells) 0.36 (BFC)	0.5 (chip) 3 (solar cells) 0.36 (BFC) 0.6 (LED)
Required Power [nW]	1.55	7.3−126	28−117 (PIM) 144 (PDM)
Cost per lens	Cheap	Moderate	Expensive
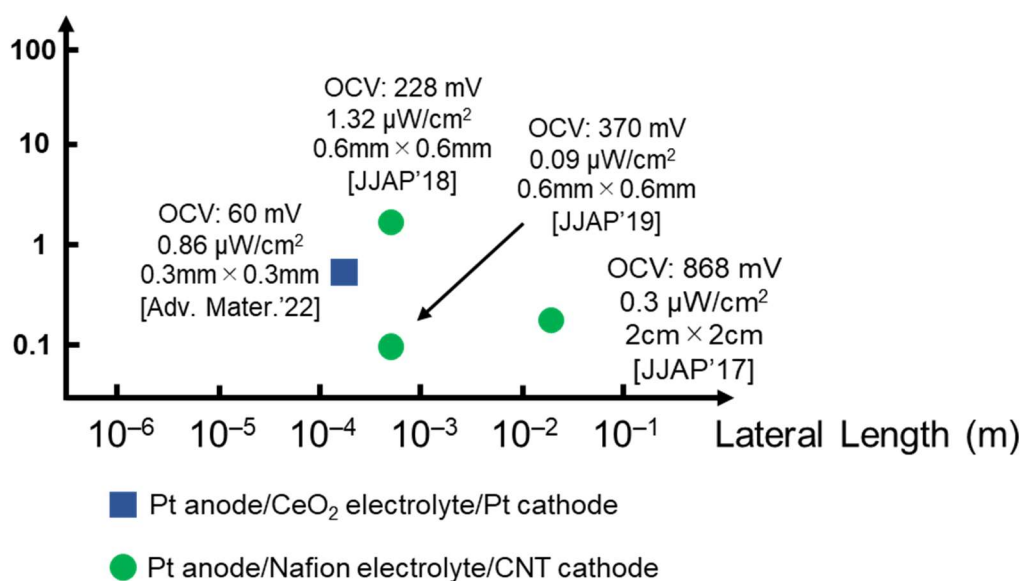
Figure 5.4: Power density at 10 mM/L glucose concentrations versus lateral length of the state-of-the-art glucose BFCs.

First, the roadmap should continue toward a long-lifetime high-yield less-variation miniaturized BFC. In the recent trend of BFCs' design, they have been scaled down to the sub-mm^2 level and achieved a high power density. Figure 5.4 shows a class of BFCs harvesting from glucose [33], [34], [48], [53]. To the best of the author's knowledge, the reported highest power density harvested from glucose attains 43 μW/cm^2 [33]. However, it requires a glucose concentration of 0.5 M/L, which is impossible in the human body. The power density is only 0.86 μW/cm^2 if scaled to 10 mM/L. By utilizing a ceramic-based electrolyte, this ceria BFC achieved a high yield, whose 84 out of 150 pieces can exhibit a nonzero open-circuit voltage (V_{OC}), in spite of that the highest V_{OC} is only 60 mV. Besides, it is durable for 140 h testing, which is the longest in the published BFCs. Some works improved power density to 1.32 μW/cm^2 [34] and V_{OC} to 228 mV which is possible to drive a CMOS chip. But the BFC performance degraded quickly after several hours, and only 6 out of 132 samples can push V_{OC} above 100 mV. Therefore, the next-generation CGM contact lenses need a high-performance BFC which can leverage the trade-offs between lifetime, yield, area, power density, V_{OC}, and so on.
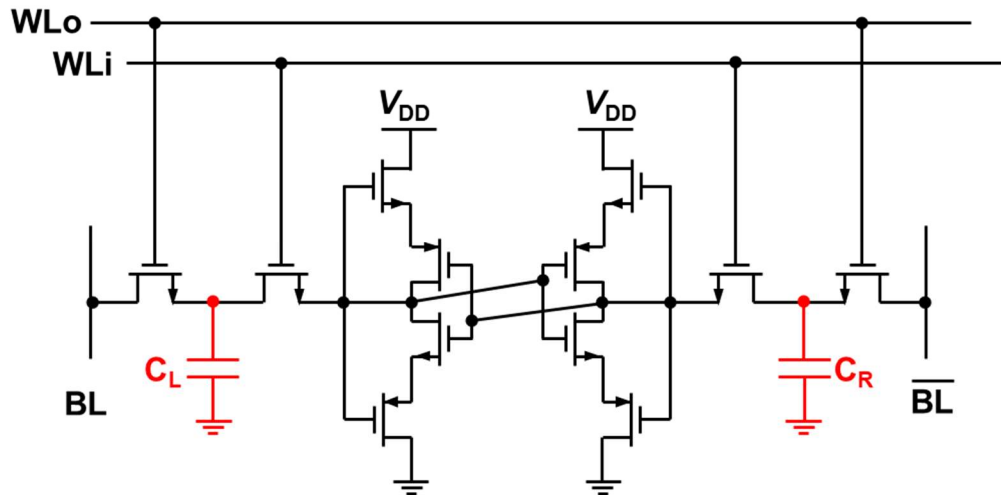
Figure 5.5: A novel circuit design for SRAM with data retention ability.

Second, a smart CGM contact lens is desired to be equipped with a memory function, which is essential to achieve learning-based intelligence. The memory circuit is also a key enabler for power-adaptive CGM systems. Both volatile and non-volatile memory circuits can play a critical role to push CGM contact lenses into real "smart" contact lenses. In the available memory option in the memory family, static random access memory (SRAM) is a good choice for CGM contact lenses due to its low reading/writing energy, data durability in the low voltage range, and high bit density. However, SRAM is a kind of volatile memory whose data can be gone if power is off. To tackle the above issue, some works proposed DLS-based SRAM dedicated to nW-level applications [74], [75]. The DLS logic can suppress the leakage current of SRAM to fW/bit, and the minimum voltage to retain the data is sub-200 mV. Some works employed the DLS-based SRAM in the microprocessor or microcontroller designs for IoT sensor nodes which are compatible with a wide power range in nW [76]–[78]. These features fit the CGM contact lens applications, but the volatile characteristics have not been solved yet. Even a blinking of eyes could erase all stored data due to the disappeared solar power. Some charge retention techniques reported in dynamic random access memory (DRAM) are promising to apply to the SRAMs [79]–[81]. As shown in Figure 5.5, by adding charge-storing capacitors, C_L, and C_R, the leakage of charge can be slowed down, and the data can be stored for a long time. Some work customized a fishbone-like charge-storing

capacitor right on the top of the SRAM circuits, without any area overhead [82]. By charging/discharging the capacitors, C_L and C_R, some work achieved compute-in-memory binary neural networks [83].

Considering that machine learning and artificial intelligence (AI) will be introduced to our edge devices, the high energy efficiency of compute-in-memory is a key enabler because the memory wall may incur large power waste due to data transfer between memory and processor unit. The versatile SRAM with various cell structures can achieve energy efficiency at tens of TOPS/W, making AI feasible on CGM contact lenses [84]. According to an example of smart contact lenses with augmented reality, the power and area overhead of introducing high-end technology is affordable on contact lenses by embedding customized batteries [27]. These techniques are promising to bring to smart contact lens applications, making real-time forecasting and warning available on smart contact lenses in Chapter IV.

Last but not least, as introduced in Chapter IV, an advanced CMOS process node can bring powerful performance elevation to energy harvester, communication units, and many other building blocks. Benefiting from the process node's evolution to 2 nm in 2024 [85], many circuit techniques in Chapter II–IV can obtain an improved figure of merit. The solar cell unit can be optimized to improve the area usage efficiency to obtain a high power density. The wireless TX/RX can shift its frequency to a higher frequency band to avoid interference, improving the signal-to-noise ratio. What's more, the circuit techniques for 5G communications can be applied to CGM contact lenses. For example, the phased array of antennas can improve the energy efficiency of communication because RF power is transmitted in a specific direction, reducing wasted power in unnecessary directions [86]. Besides the covered circuit techniques, the memory block, which will be introduced to the CGM system in the future, can have a high bit density to store data. It brings more possibilities to our circuit designers to make next-generation CGM contact lenses come true.

Acknowledgements

BIBLIOGRAPHY

BIBLIOGRAPHY

[1] "Diabetes," *World Health Organization*. https://www.who.int/news-room/fact-sheets/detail/diabetes

[2] T. Vos *et al.*, "Global burden of 369 diseases and injuries in 204 countries and territories, 1990–2019: a systematic analysis for the Global Burden of Disease Study 2019," *Lancet*, vol. 396, no. 10258, pp. 1204–1222, Oct. 2020.

[3] "Freestyle Libre CGM," *Abbott*. https://www.abbott.com/freestyle-libre-2-continuous-glucose-monitor-cgm.html

[4] "Dexcom G6 CGM," *Dexcom*. https://provider.dexcom.com/

[5] "Sibionics Dynamic CGM," *SIBIONICS*. https://www.sibionics.com/Consumer/index.html

[6] A. Hina, H. Nadeem, and W. Saadeh, "A Single LED Photoplethysmography-Based Noninvasive Glucose Monitoring Prototype System," *2019 IEEE International Symposium on Circuits and Systems (ISCAS)*. 2019. doi: 10.1109/iscas.2019.8702747.

[7] "Mobile Glucose Sensor," *Light Touch Technology*. http://www.light-tt.co.jp/product

[8] "GlucoTrack Gen 2," *GlucoTrack*. https://www.integrity-app.com/

[9] T. Tsujimura, S. Murakami, G. Chen, and K. Niitsu, "Design of 33 GHz 65-nm-CMOS small-formfactor direct-conversion receiver for non-invasive continuous glucose monitoring," in *2020 27th IEEE International Conference on Electronics, Circuits and Systems (ICECS)*, Nov. 2020, pp. 1–2.

[10] M. X. Chu *et al.*, "Soft contact lens biosensor for in situ monitoring of tear glucose as non-invasive blood sugar assessment," *Talanta*, vol. 83, no. 3, pp. 960–965, Jan. 2011.

[11] Y.-T. Liao, H. Yao, B. Parviz, and B. Otis, "A 3µW wirelessly powered CMOS glucose sensor for an active contact lens," in *2011 IEEE International Solid-State Circuits Conference*, Feb. 2011, pp. 38–40.

[12] Y.-T. Liao, H. Yao, A. Lingley, B. Parviz, and B. P. Otis, "A 3-µW CMOS glucose sensor for wireless contact-lens tear glucose monitoring," *IEEE J. Solid-State Circuits*, vol. 47, no. 1, pp. 335–344, Jan. 2012.

[13] K. Hayashi, S. Arata, S. Murakami, Y. Nishio, A. Kobayashi, and K. Niitsu, "A 6.1-nA fully integrated CMOS supply modulated OOK transmitter in 55-nm DDC CMOS for glasses-free, self-powered, and fuel-cell-embedded continuous glucose monitoring contact lens," *IEEE Trans. Circuits Syst.*

Express Briefs, vol. 65, no. 10, pp. 1360–1364, Oct. 2018.

[14] K. Hayashi *et al.*, "A 385μm × 385μm 0.165 V 0.27 nW fully-integrated supply-modulated OOK CMOS TX in 65nm CMOS for glasses-free, self-powered, and fuel-cell-embedded continuous glucose monitoring contact lens," in *2018 IEEE Biomedical Circuits and Systems Conference (BioCAS)*, Oct. 2018, pp. 379–382.

[15] J. Park *et al.*, "Soft, smart contact lenses with integrations of wireless circuits, glucose sensors, and displays," *Science Advances*, vol. 4, no. 1, p. eaap9841, 2018.

[16] C. Jeon *et al.*, "A smart contact lens controller IC supporting dual-mode telemetry with wireless-powered backscattering LSK and EM-radiated RF transmission using a single-loop antenna," *IEEE J. Solid-State Circuits*, vol. 55, no. 4, pp. 856–867, Apr. 2020.

[17] Do Hee Keum, Su-Kyoung Kim, Jahyun Koo, Geon-Hui Lee, Cheonhoo Jeon, Jee Won Mok, Beom Ho Mun, Keon Jae Lee, Ehsan Kamrani, Choun-Ki Joo, Sangbaie Shin, Jae-Yoon Sim, David Myung, Seok Hyun Yun, Zhenan Bao, Sei Kwang Hahn, "Wireless smart contact lens for diabetic diagnosis and therapy," *SCIENCE ADVANCES*, vol. 6, no. 17, pp. 1–12, Apr. 2020.

[18] E. R. Berman, *Biochemistry of the Eye*. Springer US, 1991.

[19] M. Aihara *et al.*, "Association between tear and blood glucose concentrations: Random intercept model adjusted with confounders in tear samples negative for occult blood," *J. Diabetes Investig.*, vol. 12, no. 2, pp. 266–276, Feb. 2021.

[20] J. Pandey, Yu-Te Liao, A. Lingley, R. Mirjalili, B. Parviz, and B. Otis, "A fully integrated RF-powered contact lens with a single element display," *IEEE Trans. Biomed. Circuits Syst.*, vol. 4, no. 6, pp. 454–461, Dec. 2010.

[21] Q. Li *et al.*, "From 'MISSION: IMPOSSIBLE' to mission possible: Fully flexible intelligent contact lens for image classification with analog-to-information processing," in *2017 IEEE International Symposium on Circuits and Systems (ISCAS)*, May 2017, pp. 1–4.

[22] R. Yin *et al.*, "Soft transparent graphene contact lens electrodes for conformal full-cornea recording of electroretinogram," *Nat. Commun.*, vol. 9, no. 1, pp. 1–11, Jun. 2018.

[23] B. C. Raducanu *et al.*, "An Artificial Iris ASIC with High Voltage Liquid Crystal Driver, 10 nA Light Range Detector and 40 nA Blink Detector for LCD Flicker Removal," *2020 IEEE Symposium on VLSI Circuits*. 2020. doi: 10.1109/vlsicircuits18222.2020.9163057.

[24] A. Vásquez Quintero, P. Pérez-Merino, and H. De Smet, "Artificial iris performance for smart contact lens vision correction applications," *Sci. Rep.*, vol. 10, no. 1, p. 14641, Sep. 2020.

[25] J. Kim *et al.*, "A soft and transparent contact lens for the wireless quantitative monitoring of intraocular pressure," *Nat Biomed Eng*, May 2021, doi: 10.1038/s41551-021-00719-8.

[26] "The first Smart Contact Lens that delivers a complete 24-hour picture of the eye," *SENSIMED Triggerfish*. https://www.sensimed.ch/

[27] R. Singh, S. Bailey, P. Chang, A. Olyaei, M. Hekmat, and R. Winoto, "34.2 A 21pJ/frame/pixel Imager and 34pJ/frame/pixel Image Processor for a Low-Vision Augmented-Reality Smart Contact Lens," in *2021 IEEE International Solid- State Circuits Conference (ISSCC)*, Feb. 2021, vol. 64, pp. 482–484.

[28] "ENERCHIP™ SMART SOLID STATE BATTERIES," *Cymbet*. https://www.cymbet.com/products/enerchip-solid-state-batteries/ (accessed Dec. 05, 2022).

[29] *Energy Harvesting Technologies*. Springer US.

[30] R. J. M. Vullers, R. van Schaijk, H. J. Visser, J. Penders, and C. Van Hoof, "Energy Harvesting for Autonomous Wireless Sensor Networks," *IEEE Solid-State Circuits Mag.*, vol. 2, no. 2, pp. 29–38, Spring 2010.

[31] J. Xie, C. Lee, and H. Feng, "Design, Fabrication, and Characterization of CMOS MEMS-Based Thermoelectric Power Generators," *J. Microelectromech. Syst.*, vol. 19, no. 2, pp. 317–324, Apr. 2010.

[32] V. Bhatnagar and P. Owende, "Energy harvesting for assistive and mobile applications," *Energy Sci. Eng.*, vol. 3, no. 3, pp. 153–173, May 2015.

[33] P. Simons, S. A. Schenk, M. A. Gysel, L. F. Olbrich, and J. L. M. Rupp, "A ceramic-electrolyte glucose fuel cell for implantable electronics," *Adv. Mater.*, vol. 34, no. 24, p. e2109075, Jun. 2022.

[34] S. Arata, K. Hayashi, Y. Nishio, A. Kobayashi, K. Nakazato, and K. Niitsu, "Wafer-scale development and experimental verification of 0.36mm2 228mV open-circuit-voltage solid-state CMOS-compatible glucose fuel cell," *Jpn. J. Appl. Phys.*, vol. 57, p. 04FM04, Mar. 2018.

[35] H. Kloub, D. Hoffmann, B. Folkmer, and Y. Manoli, "A micro capacitive vibration energy harvester for low power electronics," *Work*, 1740, [Online]. Available: https://www.researchgate.net/profile/Daniel-Hoffmann-11/publication/267998601_A_MICRO_CAPACITIVE_VIBRATION_ENER GY_HARVESTER_FOR_LOW_POWER_ELECTRONICS/links/54649e740

cf2837efdb45db0/A-MICRO-CAPACITIVE-VIBRATION-ENERGY-HARVESTER-FOR-LOW-POWER-ELECTRONICS.pdf

[36] L. Deng, Z. Wen, X. Zhao, C. Yuan, G. Luo, and J. Mo, "High Voltage Output MEMS Vibration Energy Harvester in d_31 Mode With PZT Thin Film," *J. Microelectromech. Syst.*, vol. 23, no. 4, pp. 855–861, Aug. 2014.

[37] S. Oh and D. D. Wentzloff, "A −32dBm sensitivity RF power harvester in 130nm CMOS," in *2012 IEEE Radio Frequency Integrated Circuits Symposium*, Jun. 2012, pp. 483–486.

[38] N. Efron, G. Young, and N. A. Brennan, "Ocular surface temperature," *Curr. Eye Res.*, vol. 8, no. 9, pp. 901–906, Sep. 1989.

[39] C. Purslow, J. S. Wolffsohn, and J. Santodomingo-Rubido, "The effect of contact lens wear on dynamic ocular surface temperature," *Cont. Lens Anterior Eye*, vol. 28, no. 1, pp. 29–36, Mar. 2005.

[40] M. Alioto, "From less batteries to battery-less alert systems with wide power adaptation down to nWs—toward a smarter, greener world," *IEEE Des. Test Comput.*, vol. 38, no. 5, pp. 90–133, Oct. 2021.

[41] K. Uchiyama, G. Chen, and K. Niitsu, "Design of Fully-Integrated Self-Powered FM Transmitter Using On-Chip Photodiodes in 65-nm CMOS," in *2020 27th IEEE International Conference on Electronics, Circuits and Systems (ICECS)*, Nov. 2020, pp. 1–2.

[42] A. Kobayashi, K. Hayashi, S. Arata, S. Murakami, G. Xu, and K. Niitsu, "Design of a self-controlled dual-oscillator-based supply voltage monitor for biofuel-cell-combined biosensing systems in 65-nm CMOS and 55-nm DDC CMOS," *IEEE Trans. Biomed. Circuits Syst.*, vol. 13, no. 6, pp. 1152–1162, Dec. 2019.

[43] A. Kobayashi *et al.*, "Design and experimental verification of a 0.19 V 53 μW 65 nm CMOS integrated supply-sensing sensor with a supply-insensitive temperature sensor and an inductive-coupling transmitter for a self-powered bio-sensing system using a biofuel cell," *IEEE Trans. Biomed. Circuits Syst.*, vol. 11, no. 6, pp. 1313–1323, Dec. 2017.

[44] A. F. Yeknami *et al.*, "A 0.3-V CMOS biofuel-cell-powered wireless glucose/lactate biosensing system," *IEEE J. Solid-State Circuits*, vol. 53, no. 11, pp. 3126–3139, Nov. 2018.

[45] K. Niitsu *et al.*, "A self-powered supply-sensing biosensor platform using bio fuel cell and low-voltage, low-cost CMOS supply-controlled ring oscillator with inductive-coupling transmitter for healthcare IoT," *IEEE Trans. Circuits Syst. I Regul. Pap.*, vol. 65, no. 9, pp. 2784–2796, Sep. 2018.

[46] A. Kobayashi *et al.*, "A solar-cell-assisted, 99.66% biofuel cell area reduced, biofuel-cell-powered wireless biosensing system in 65-nm CMOS for continuous glucose monitoring contact lenses," in *2019 26th IEEE International Conference on Electronics, Circuits and Systems (ICECS)*, Nov. 2019, pp. 61–64.

[47] A. H. Talkhooncheh *et al.*, "A fully-integrated biofuel-cell-based energy harvester with 86% peak efficiency and 0.25V minimum input voltage using source-adaptive MPPT," in *2020 IEEE Custom Integrated Circuits Conference (CICC)*, 2020. doi: 10.1109/cicc48029.2020.9075912.

[48] K. Niitsu, T. Ando, A. Kobayashi, and K. Nakazato, "Enhancement in open-circuit voltage of implantable CMOS-compatible glucose fuel cell by improving the anodic catalyst," *Jpn. J. Appl. Phys.*, vol. 56, no. 1S, p. 01AH04, Nov. 2016.

[49] A. Kobayashi, K. Hayashi, S. Arata, S. Murakami, G. Xu, and K. Niitsu, "A 65-nm CMOS 1.4-nW self-controlled dual-oscillator-based supply voltage monitor for biofuel-cell-combined biosensing systems," in *2019 IEEE International Symposium on Circuits and Systems (ISCAS)*, May 2019, pp. 1–5.

[50] Z. Chen, M.-K. Law, P.-I. Mak, and R. P. Martins, "A single-chip solar energy harvesting IC using integrated photodiodes for biomedical implant applications," *IEEE Trans. Biomed. Circuits Syst.*, vol. 11, no. 1, pp. 44–53, Feb. 2017.

[51] P. P. Mercier, S. Bandyopadhyay, A. C. Lysaght, K. M. Stankovic, and A. P. Chandrakasan, "A sub-nW 2.4 GHz transmitter for low data-rate sensing applications," *IEEE J. Solid-State Circuits*, vol. 49, no. 7, pp. 1463–1474, Jul. 2014.

[52] W. Jung *et al.*, "An ultra-low power fully integrated energy harvester based on self-oscillating switched-capacitor voltage doubler," *IEEE J. Solid-State Circuits*, vol. 49, no. 12, pp. 2800–2811, Dec. 2014.

[53] S. Arata *et al.*, "Yield and open-circuit-voltage enhancement of 0.36 mm2 solid-state CMOS-compatible glucose fuel cells by using repeated separator coating," *Jpn. J. Appl. Phys.*, vol. 58, no. SBBG11, pp. 1–5, 2019.

[54] Y. Zhang *et al.*, "A batteryless 19 μW MICS/ISM-band energy harvesting body sensor node SoC for ExG applications," *IEEE J. Solid-State Circuits*, vol. 48, no. 1, pp. 199–213, Jan. 2013.

[55] Z. Xiao *et al.*, "An implantable RFID sensor tag toward continuous glucose monitoring," *IEEE Journal of Biomedical and Health Informatics*, vol. 19, no.

3, pp. 910–919, May 2015.

[56] C. Jeon *et al.*, "A 143nW glucose-monitoring smart contact lens IC with a dual-mode transmitter for wireless-powered backscattering and RF-radiated transmission using a single loop antenna," in *2019 Symposium on VLSI Circuits*, Jun. 2019, pp. C294–C295.

[57] G. Chen *et al.*, "A 0.5 mm^2 0.31 V/0.39 V 28 nW/144 nW 65 nm CMOS solar cell-powered biofuel cell-input biosensing system with PIM/PDM LED driving for stand-alone RF-less continuous glucose monitoring contact lens," in *ESSCIRC 2021 - IEEE 47th European Solid State Circuits Conference (ESSCIRC)*, Sep. 2021, pp. 171–174.

[58] L. Boccardo, "Viewing distance of smartphones in presbyopic and non-presbyopic age," *J. Optom.*, vol. 14, no. 2, pp. 120–126, Apr. 2021.

[59] L.-H. Lu, H.-H. Hsieh, and Y.-T. Liao, "A wide tuning-range CMOS VCO with a differential tunable active inductor," *IEEE Trans. Microw. Theory Tech.*, vol. 54, no. 9, pp. 3462–3468, Sep. 2006.

[60] J. Xu, C. E. Saavedra, and G. Chen, "An active inductor-based VCO with wide tuning range and high DC-to-RF power efficiency," *IEEE Trans. Circuits Syst. Express Briefs*, vol. 58, no. 8, pp. 462–466, Aug. 2011.

[61] C. Liang and B. Razavi, "A layout technique for millimeter-wave PA transistors," in *2011 IEEE Radio Frequency Integrated Circuits Symposium*, Jun. 2011, pp. 1–4.

[62] M. Lanuzza, F. Crupi, S. Rao, R. De Rose, S. Strangio, and G. Iannaccone, "An ultralow-voltage energy-efficient level shifter," *IEEE Trans. Circuits Syst. Express Briefs*, vol. 64, no. 1, pp. 61–65, Jan. 2017.

[63] T. M. Quan *et al.*, "AI-based edge-intelligent hypoglycemia prediction system using alternate learning and inference method for blood glucose level data with low-periodicity," in *2019 IEEE International Conference on Artificial Intelligence Circuits and Systems (AICAS)*, Mar. 2019, pp. 201–206.

[64] A. Kobayashi, Y. Nishio, K. Hayashi, K. Nakazato, and K. Niitsu, "A 350-mV, under-200-ppm allan deviation floor gate-leakage-based timer using an amplifier-less replica-bias switching technique in 55-nm DDC CMOS," in *2018 IEEE Custom Integrated Circuits Conference (CICC)*, Apr. 2018, pp. 1–4.

[65] J. Jiang, W.-H. Ki, and Y. Lu, "Digital 2-/3-phase switched-capacitor converter with ripple reduction and efficiency improvement," *IEEE J. Solid-State Circuits*, vol. 52, no. 7, pp. 1836–1848, Jul. 2017.

[66] J. Choi, E. Aklimi, C. Shi, D. Tsai, H. Krishnaswamy, and K. L. Shepard, "Matching the power, voltage, and size of biological systems: a nW-scale, 0.023-mm^3 pulsed 33-GHz radio transmitter operating from a 5 kT/q-supply voltage," *IEEE Trans. Circuits Syst. I Regul. Pap.*, vol. 62, no. 8, pp. 1950–1958, Aug. 2015.

[67] N. Shah, P. Lajevardi, K. Wojciechowski, C. Lang, and B. Murmann, "An Energy Harvester Using Image Sensor Pixels With Cold Start and Over 96% MPPT Efficiency," *IEEE Solid-State Circuits Letters*, vol. 2, no. 9, pp. 207–210, Sep. 2019.

[68] F. Horiguchi, "Integration of series-connected on-chip solar battery in a triple-well CMOS LSI," *IEEE Trans. Electron Devices*, vol. 59, no. 6, pp. 1580–1584, Jun. 2012.

[69] M. Megahed, Y. Ramadass, and T. Anand, "A sub 1µW switched source + capacitor architecture free of top/bottom plate parasitic switching loss achieving peak efficiency of 80.66% at a regulated 1.8V output in 180nm," in *2019 IEEE Custom Integrated Circuits Conference (CICC)*, Apr. 2019, pp. 1–4.

[70] "SML-P12x/P13x Series PICOLED Data Sheet," *Rohm Semiconductor*. https://fscdn.rohm.com/jp/products/databook/datasheet/opto/led/chip_mono/sml-p1-j.pdf (accessed Dec. 14, 2022).

[71] X. Wang, P.-H. P. Wang, Y. Cao, and P. P. Mercier, "A 0.6V 75nW all-CMOS temperature sensor with 1.67m°C/mV supply sensitivity," *IEEE Trans. Circuits Syst. I Regul. Pap.*, vol. 64, no. 9, pp. 2274–2283, Sep. 2017.

[72] O. Aiello, P. Crovetti, and M. Alioto, "A sub-leakage pW-power Hz-range relaxation oscillator operating with 0.3V-1.8V unregulated supply," in *2018 IEEE Symposium on VLSI Circuits*, 2018. doi: 10.1109/vlsic.2018.8502413.

[73] W. Lim, I. Lee, D. Sylvester, and D. Blaauw, "8.2 Batteryless sub-nW Cortex-M0+ processor with dynamic leakage-suppression logic," in *2015 IEEE International Solid-State Circuits Conference - (ISSCC) Digest of Technical Papers*, Feb. 2015, pp. 1–3.

[74] S. Gupta, D. S. Truesdell, and B. H. Calhoun, "A 65nm 16kb SRAM with 131.5pW Leakage at 0.9V for Wireless IoT Sensor Nodes," in *2020 IEEE Symposium on VLSI Circuits*, Jun. 2020, pp. 1–2.

[75] Y. Wang, G. Chen, X. Yu, X. Chen, and K. Niitsu, "A 22nm CMOS 0.2V 13.3nW 16T SRAM Using Dynamic Leakage Suppression and Half-Selected Free Technique," in *2021 IEEE Asia Pacific Conference on Circuit and Systems (APCCAS)*, Nov. 2021, pp. 29–32.

[76] D. S. Truesdell, X. Liu, J. Breiholz, S. Gupta, S. Li, and B. H. Calhoun, "NanoWattch: A Self-Powered 3-nW RISC-V SoC Operable from 160mV Photovoltaic Input with Integrated Temperature Sensing and Adaptive Performance Scaling," in *2022 IEEE Symposium on VLSI Technology and Circuits (VLSI Technology and Circuits)*, Jun. 2022, pp. 210–211.

[77] D. S. Truesdell, J. Breiholz, S. Kamineni, N. Liu, A. Magyar, and B. H. Calhoun, "A 6–140-nW 11 Hz–8.2-kHz DVFS RISC-V Microprocessor Using Scalable Dynamic Leakage-Suppression Logic," *IEEE Solid-State Circuits Letters*, vol. 2, no. 8, pp. 57–60, Aug. 2019.

[78] L. Lin, S. Jain, and M. Alioto, "Sub-nW Microcontroller With Dual-Mode Logic and Self-Startup for Battery-Indifferent Sensor Nodes," *IEEE J. Solid-State Circuits*, vol. 56, no. 5, pp. 1618–1629, May 2021.

[79] K. C. Chun, W. Zhang, P. Jain, and C. H. Kim, "A 2T1C Embedded DRAM Macro With No Boosted Supplies Featuring a 7T SRAM Based Repair and a Cell Storage Monitor," *IEEE J. Solid-State Circuits*, vol. 47, no. 10, pp. 2517–2526, Oct. 2012.

[80] W. Zhang, K. C. Chun, and C. H. Kim, "A write-back-free 2T1D embedded DRAM with local voltage sensing and a dual-row-access low power mode," in *Proceedings of the IEEE 2012 Custom Integrated Circuits Conference*, Sep. 2012, pp. 1–4.

[81] C. Yu, T. Yoo, H. Kim, T. T.-H. Kim, K. C. T. Chuan, and B. Kim, "A Logic-Compatible eDRAM Compute-In-Memory With Embedded ADCs for Processing Neural Networks," *IEEE Trans. Circuits Syst. I Regul. Pap.*, vol. 68, no. 2, pp. 667–679, Feb. 2021.

[82] T. Urabe, H. Ochi, and K. Kobayashi, "Nonvolatile SRAM Using Fishbone-in-Cage Capacitor in a 180 nm Standard CMOS Process for Zero-Standby and Instant-Powerup Embedded Memory on IoT," *2021 IEEE Symposium in Low-Power and High-Speed Chips (COOL CHIPS)*. 2021. doi: 10.1109/coolchips52128.2021.9410314.

[83] H. Oh *et al.*, "Energy-efficient charge sharing-based 8T2C SRAM in-memory accelerator for binary neural networks in 28nm CMOS," in *2021 IEEE Asian Solid-State Circuits Conference (A-SSCC)*, Nov. 2021, pp. 1–3.

[84] A. Biswas and A. P. Chandrakasan, "CONV-SRAM: An Energy-Efficient SRAM With In-Memory Dot-Product Computation for Low-Power Convolutional Neural Networks," *IEEE J. Solid-State Circuits*, vol. 54, no. 1, pp. 217–230, Jan. 2019.

[85] P. Singer, "20-year semiconductor roadmap: tearing down the walls," *imec*,

Aug. 02, 2022. https://www.imec-int.com/en/articles/20-year-roadmap-tearing-down-walls (accessed Jan. 14, 2023).

[86] M. Ide, A. Shirane, K. Yanagisawa, D. You, J. Pang, and K. Okada, "A 28-GHz Phased-Array Relay Transceiver for 5G Network Using Vector-Summing Backscatter with 24-GHz Wireless Power and LO Transfer" *IEEE J. Solid-State Circuits*, vol. 57, no. 4, pp. 1211–1223, Apr. 2022.

Publications Related to This Dissertation

Journals

1. **Guowei Chen**, Yue Wang, Tran Minh Quan, Naofumi Matsuyama, Takuya Tsujimura and Kiichi Niitsu, "A 0.5 mm^2 Solar Cell-Powered Biofuel Cell-Input Biosensing System with LED Driving for Stand-Alone RF-Less Continuous Glucose Monitoring Contact Lens", *IEEE Solid-State Circuits Letters*, vol. 5, pp. 41–44, Feb. 2022.

2. **Guowei Chen**, Kiichi Niitsu, "A Solar-Cell-Assisted, 99% Biofuel Cell Area Reduced, Biofuel-Cell-Powered Wireless Biosensing System in 65nm CMOS for Continuous Glucose Monitoring Contact Lenses", *IEICE Transactions on Electronics*, vol. E105.C, Issue 7, pp. 343–348, Jul. 2022.

3. **Guowei Chen**, Xujiaming Chen, Kiichi Niitsu, "Design and Experimental Verification of a 2.1nW 0.018mm^2 Slope ADC-Based Supply Voltage Monitor for Biofuel-Cell-Powered Supply-Sensing Systems in 180-nm CMOS", *IEICE Transactions on Electronics*, vol. E105.C, Issue 10, pp. 565–570, Oct. 2022.

International Conference

1. Guowei Chen, Xinyang Yu, Yue Wang, Tran Minh Quan, Naofumi Matsuyama, Takuya Tsujimura, Md. Zahidul Islam and Kiichi Niitsu, "A 0.5 mm^2 0.31 V/0.39 V 28 nW/144 nW 65 nm CMOS solar cell-powered biofuel cell-input biosensing system with PIM/PDM LED driving for stand-alone RF-less continuous glucose monitoring contact lens," i*n ESSCIRC 2021 - IEEE 47th European Solid State Circuits Conference (ESSCIRC)*, Sep. 2021, pp. 171–174.

2. Guowei Chen, Xinyang Yu, Yue Wang, Tran Minh Quan, Naofumi Matsuyama, Takuya Tsujimura and Kiichi Niitsu, " A 0.5 mm^2 Ambient Light-Driven Solar Cell-Powered Biofuel Cell-Input Biosensing System with LED Driving for Stand-Alone RF-Less Continuous Glucose Monitoring Contact Lens", *Asia and South Pacific Design Automation Conference – University Design Contest (ASP-DAC UDC 2022)*, Jan. 2022, pp. 1–2.

Domestic Conference

1. Guowei Chen, Xinyang Yu, Yue Wang, Tran Minh Quan, 松山直史, 辻村拓也, Xujiaming Chen, 加藤 空, 林 右馬, 田中彬義, Huy Nghiep DUONG, Md. Zahidul Islam, 新津葵一,中村 迅, "無線レス単独自立動作可能な持続血糖モニタリングコンタクトレンズに向けたパルス密度変調LED駆

動機能付き環境光駆動バイオ発電素子入力 65nm CMOS バイオセンサ集積システム,” 電子情報通信学会 LSI とシステムのワークショップ 2021, 2021 年 5 月, ポスターセッション学生部門.

Awards

1. Guowei Chen, Xinyang Yu, Yue Wang, Tran Minh Quan, 松山直史, 辻村拓也, Xujiaming Chen, 加藤 空, 林 右馬, 田中彬義, Huy Nghiep DUONG, Md. Zahidul Islam, 新津葵一, 中村 迅, LSI とシステムのワークショップ 2021, IEEE SSCS Japan Chapter Academic Research Award, May 11, 2021.

2. Guowei Chen, Xinyang Yu, Yue Wang, Tran Minh Quan, Naofumi Matsuyama, Takuya Tsujimura, Kiichi Niitsu, ASP-DAC 2022 Best Design Award, Jan. 20, 2022.